CERN-THESIS-2014-340

ALMA MATER STUDIORUM · UNIVERSITÀ DI BOLOGNA

DIPARTIMENTO DI FISICA ED ASTRONOMIA
DOTTORATO DI RICERCA IN FISICA, XXVI CICLO
Settore Concorsuale di afferenza: 02/A1
Settore Scientifico disciplinare: FIS/04 - Fisica Nucleare e Subnucleare

VECTOR MESON PHOTOPRODUCTION IN ULTRA-PERIPHERAL HEAVY ION COLLISIONS WITH ALICE AT THE LHC

DR. ANDREA AGOSTINELLI

Coordinatore Dottorato:
Prof.
Fabio Ortolani

Relatore:
Chiar.ma Prof.ssa
Luisa Cifarelli

Esame finale anno 2014

Contents

Introduction

The research activities presented in this thesis have been carried out within the ALICE (A Large Ion Collider Experiment) Collaboration at the CERN LHC (Large Hadron Collider), Geneva. The main goal of the experiment is the study of a particular state of the matter that can be created at the extreme temperature conditions reached by colliding ultra-relativistic heavy ions. The aim is the investigation − with a better accuracy with respect to the past − of the theoretical predictions for the existence of a QCD (Quantum Chromo Dynamics) transition from an ordinary nuclear and hadronic matter to a state in which quark and gluons are deconfined in an expanding medium, historically called Quark Gluon Plasma (QGP). According to the hot Big Bang model of cosmology such a transition must have occurred also in the primordial expanding Universe, where after the electro-weak phase transition, the initial deconfined partons plasma would have reached the hadronic phase about 1 μs after the Big Bang. Afterwards more recent measurements performed at the RHIC (Relativistic Heavy Ion Collider) facility of Brookhaven National Laboratory, a new physical characterization of the medium turned out: the created fireball has rather the properties of a perfect fluid than those of a plasma. This fireball, initially in local thermal equilibrium, rapidly expands and cools down on the basis of relativistic thermodynamics. When the temperature goes below the critical temperature of the QCD phase transition, hadronisation takes place and the particle abundances are fixed, in the commonly called "chemical freeze-out". The expansion continues accompanied with elastic scattering of the regenerated hadrons up to the "kinematic freeze-out", a stage in which the distances between hadrons are larger than the range of the interaction. At this point also elastic collisions stop and the kinematic of the final state is fixed.

The evolution of the fireball is nowadays estimated by lattice QCD computations. The theory of strong interactions between coloured charges indeed, is very well known in its perturbative regime (pQCD), but still not fully understood in the non-perturbative domain, where the lattice QCD approximations are adopted for calculations. These theoretical uncertainties must be summed to those related to hadronization and the initial state effects, in which the parton content inside the nuclei plays a fundamental role in the description of the possible interactions. A better knowledge of the nuclear parton distribution functions (nPDFs) reduces therefore the uncertainties related to the initial state effects and the final hadronisation, disentangling these contributions from those characterizing the nature of the QGP itself. In particular, the gluon distribution in the nuclei, namely $g_A(x,Q^2)$, could be sensitive to nuclear shadowing effects both at low Bjorken$-x$ ($x \ll 10^{-2}$) and low transferred 4-momentum ($Q^2 \sim 1$ GeV^2). In this framework, a rapidity-wise analysis of the photoproduction of vector mesons like the J/ψ allows to better constrain the behaviour of $g_A(x,Q^2)$, probing possible gluon shadowing effects at different ranges of Bjorken$-x$. In ALICE the accessible range goes from $x \sim 10^{-2}$ to $x \sim 10^{-3}$, at the LHC energies of $\sqrt{s_{NN}} = 2.76$ TeV. The collected results at LHC will extend to lower values the knowledge on the phase space (x,Q^2) explored in deep inelastic scattering (DIS) at greater transferred 4-momenta ($Q^2 \sim 100$ GeV^2), a region where pQCD is again fully working.

A feasible approach to the study of photoproduction processes at the LHC is by means of

ultra-peripheral heavy-ion collisions (UPCs), in which two accelerated ions surrounded by a cloud of quasi-real photons, interact with an impact parameter of several tens of femtometres, namely larger than the sum of their radii, excluding in this way purely hadronic interactions. The rate of processes involving the interaction with these photons is maximized in heavy-ion collisions, where the photon flux is proportional to the square of the electric charge of the accelerated particle, gaining thus a factor Z^2 with respect collisions among protons. Moreover, the high intensity of the photon flux produces an abundance of di-lepton pairs, e^+e^- and $\mu^+\mu^-$, from two-photon interactions. A comparison between the data and the predictions on the $\gamma\gamma$ scattering cross-section represents a remarkable contribution to the studies on the QED perturbative approach with a bigger effective coupling $Z \times \sqrt{\alpha_{QED}(Q^2)}$.

In this work the results of the the first measurements on the J/ψ and e^+e^-photoproduction performed at the LHC are summarized. The analysis of the data collected at central rapidity by ALICE in the 2011 $Pb-Pb$ collisions is illustrated. All steps of the analysis are described, from data acquisition to the final results and comparisons of the extracted cross-section with the available models. The work illustrated in what follows contributed to the conclusions recently published in [1]. In Chapter 1 a survey on the physics of ultra-peripheral collisions and the implications to the low-x physics studies is discussed. The importance of this analysis within the ALICE heavy-ion research program is also pointed out. Chapter 2 describes the ALICE detector at the LHC, focusing on the systems involved in the experimental set-up and the offline framework developed by the collaboration to analyse the data. Chapter 3 is dedicated to the description of the Time-Of-Flight (TOF) system and its performance during different periods of data taking. The TOF is a key detector for the analysis presented here, owing to its capability to deliver a fast topological trigger signal as required for the selection of UPCs. Finally, Chapter 4 presents the details of the analysis and the results on the measurement of the photoproduction cross-section of J/ψ and e^+e^-pairs at mid-rapidity.

Chapter 1

Physics of ultra-peripheral nuclear collisions

In this chapter a general review on the theoretical constrains to photoproduction processes in $A-A$ and $p-A$ collisions is reported. The approach followed in this discussion can be more extensively found in [2, 3, 4]. Moving highly-charged ions carry strong electromagnetic fields that act as a beam of photons. In collisions at large impact parameters, hadronic interactions are strongly suppressed, and the ions may interact through photon-ion and photon-photon collisions known as ultra-peripheral collisions (UPCs). Hadron colliders like the Large Hadron Collider (LHC) produce photonuclear and two-photon interactions at luminosities and energies beyond that accessible elsewhere; the LHC reaches a γp energy ten times that of the Hadron-Electron Ring Accelerator (HERA). Because of these interesting features, photon-ion interactions represent a remarkable tool to constrain the effects of the nuclear gluon shadowing on the nuclear parton density functions (nPDFs). In a similar way, photon-photon interactions offer the possibility to study quantum electrodynamics (QED) effects in new energy domains.

1.1 Introduction

In 1924, Enrico Fermi submitted the paper "On the Theory of Collisions Between Atoms and Elastically Charged Particles" to Zeitschrift für Physik [7]. In this publication, Fermi devised a method known as the equivalent (or virtual) photon method, where he treated the electromagnetic fields of a charged particle as a flux of virtual photons. Ten years later, Weiszsäcker and Williams extended this approach to include ultra-relativistic particles, and the method is known as the Weizsäcker-Williams method [8]. A fast-moving charged particle has electric field vectors pointing radially outward and magnetic fields circling it. The field at a point some distance away from the trajectory of the particle resembles that of a real photon. Thus, Fermi replaced the electromagnetic fields from a fast particle with an equivalent flux of photons. The flux of photons with energy k , $dN_\gamma(k)/dk$, is given by the Fourier transform of the time-dependent electromagnetic field. UPCs, are those reactions in which two ions interact via their cloud of virtual photons at an impact parameter of several tens of femtometers, larger than the sum of the two radii. The intensity of the electromagnetic field, and therefore the number of photons in the cloud surrounding the nucleus, is proportional to Z^2, where Z is the atomic number. Thus these types of interactions are highly favoured when heavy ions collide. The virtual photon approach used in QED to describe, e.g., atomic ionization or nuclear excitation by a charged particle, can be simply described using Fermis approach. When two nuclei collide, two types of electromagnetic processes can occur. A photon emitted by one ion can strike the other ion,

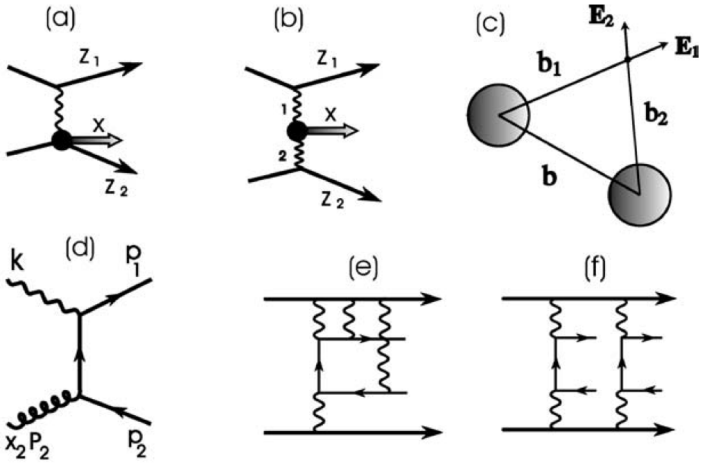

Figure 1.1 *(a)* One-photon and *(b)* two-photon processes in heavy ion collisions. *(c)* Geometrical representation of the photon fluxes at a point outside nuclei 1 and 2, in a collision with impact parameter b. The electric field of the photons at that point are also shown. *(d)* Feynman diagram for $q\bar{q}$ production through photon-gluon fusion to leading order. *(e, f)* Example of higher order corrections to pair production: *(e)* Coulomb distortion and *(f)* production of multiple pairs.

Fig. 1.1a, or, photons from each nucleus can collide, in a photon-photon collision, as in Fig. 1.1b. In these diagrams the nucleus that emits the photon remains intact after the collision. However, it is possible to have an ultra-peripheral interaction in which one or both nuclei break up. The breakup may occur through the exchange of an additional photon. In calculations of ultra-peripheral $A-B$ collisions, the impact parameter is usually required to be larger than the sum of the two nuclear radii, $b > R_A + R_B$. Strictly speaking, an ultra-peripheral electromagnetic interaction could occur simultaneously with a hadronic collision. However, since it is not possible to separate the hadronic and electromagnetic components in such collisions, the hadronic components are excluded by the impact parameter cut. Ultra-peripheral hadron-hadron collisions will provide unique opportunities for studying electromagnetic processes. At the LHC, photon-proton collisions occur at center of mass energies an order of magnitude higher than those available at previous accelerators, and photon-heavy ion collisions reach 30 times the energies available at fixed target accelerators. Ultra-relativistic heavy-ion interactions have been used to study nuclear photoexcitation (*e.g.*, to a Giant Dipole Resonance) and photoproduction of hadrons. Coulomb excitation is a traditional tool in low-energy nuclear physics. The strong electromagnetic fields from a heavy ion allow for the study of multi-photon excitation of nuclear targets. The high photon energies can also be used to study the gluon density in heavy nuclei at low Bjorken-x[1], as this thesis will explain: the exclusive photoproduction of vector mesons (in particular J/ψ) in UPCs is one of the ALICE goals to investigate the behaviour of the nuclear PDFs (nPDFs) at low x. The photoproduction of vector mesons can be classified in two categories, coherent or incoherent. In the coherent processes, the photon wavelengths has the same order of magnitude of the ions radius ($\lambda_\gamma \sim R_A$), that is, the photon couples coherently with the whole electromagnetic field of the target ion. In most cases no nuclear break-up happens and the photoproduced vector meson has a transverse momentum distribution peaked at very low values, $p_T \sim 1/R_A = 60$ MeV$/c$, that implies a well defined event topology in the transverse plane, as it will be described in the last chapter. For the incoherent processes, the impinging photon scatters off a single nucleon since its wavelengths has the same order of mag-

[1] The Bjorken-x is a kinematic parameter that represents the fraction of the momentum of the nucleon carried by the gluons. Along the texts, several mathematical expression of this quantity will be given.

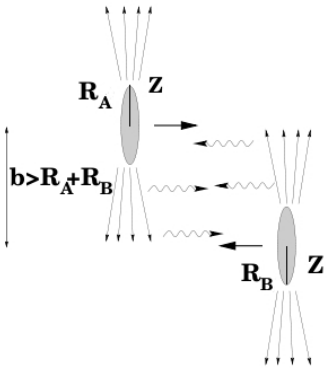

Figure 1.2 Highly energetic charges have a Lorentz contracted electric (and magnetic) field. The interaction between these fields can be replaced by the interaction of real (or quasi-real) photons. Strong hadronic interactions are suppressed whenever the impact parameter of the colliding nuclei is greater than the sum of their two radii.

nitude of the nucleon radius, $\lambda_\gamma \sim r_N$. In most cases the target nucleus breaks-up and the average vector meson momenta are around 500 MeV$/c$. In the most general case, the cross section for photoproduction of a state X is

$$\sigma_X = \int dk \frac{dN_\gamma(k)}{dk} \sigma_X^\gamma(k), \tag{1.1}$$

where $\sigma_X^\gamma(k)$ is the photonuclear cross section.

Photon-photon (or two-photon) processes have long been studied at e^+e^-colliders. They are an excellent tool for many aspects of meson spectroscopy and tests of QED. At hadron colliders, they are also used to study atomic physics processes, often involving electrodynamics in strong fields. One striking success was the production of antihydrogen atoms at CERN's LEAR1 [11] and at the Fermilab Tevatron [12]. At the highest energy colliders, reactions like $\gamma\gamma \to X$ may be used to probe the quark content and spin structure of meson resonances. Production of meson or baryon pairs can also probe the internal structure of hadrons. The study of ALICE collected data in photon-pohoton reactions, in particular the $\gamma\gamma \to e^+e^-$ channel, will be presented. The cross section for two-photon processes is

$$\sigma_X = \int dk_1 dk_2 \frac{dN_\gamma(k_1)}{dk_1} \frac{dN_\gamma(k_2)}{dk_2} \sigma_X^{\gamma\gamma}(k_1,k_2), \tag{1.2}$$

where $\sigma_X^{\gamma\gamma}(k_1,k_2)$ is the two-photon cross section.

It is necessary now to better investigate what are the photon flux and the photoproduction cross sections that the two formulas take into account.

1.2 Photon flux

In this section the formalism of the photon flux adopted in the treatise of photonuclear processes is introduced. The considerations developed here can be extended to the two-photon interaction process.

AB	L_{AB} ($\mathrm{mb}^{-1}\mathrm{s}^{-1}$)	$\sqrt{s_{NN}}$(TeV)	γ_L	k_{max} (GeV/c)	E_{max} (TeV)	$\sqrt{s_{\gamma N}^{max}}$ (GeV)	$\sqrt{s_{\gamma\gamma}^{max}}$ (GeV)
SPS							
$In-In$	-	0.017	168	0.30	5.71×10^{-3}	3.4	0.7
$Pb-Pb$	-	0.017	168	0.25	4.66×10^{-3}	2.96	0.5
RHIC							
$Au-Au$	0.4	0.2	106	3.0	0.64	34.7	6.0
$p-p$	6000	0.5	266	87	46.6	296	196
LHC							
$O-O$	160	7	3730	243	1820	1850	486
$Ar-Ar$	43	6.3	3360	161	1080	1430	322
$Pb-Pb$	0.42	5.5	2930	81	480	950	162
$p-O$	10,000	9.9	5270	343	3620	2610	686
$p-Ar$	5800	9.39	5000	240	2400	2130	480
$p-Pb$	420	8.8	4690	130	1220	1500	260
$p-p$	10^7	14	7455	2452	36,500	8390	4504

Table 1.1 Pertinent parameters and kinematic limits for some projectile-target combinations at several accelerator, as computeb by [3]. At first, the luminosities and the NN collision kinematics, the nucleon-nucleon center of mass energies, $\sqrt{s_{NN}}$, the Lorentz factors, γ_L are listed. Afterwards, the photon cutoff energies in the center of mass frame, k_{max}, and in the nuclear rest frame, E_{max}, as well as the equivalent maximum photonnucleon and photonphoton center of mass energies, $\sqrt{s_{\gamma N}^{max}}$ and $\sqrt{s_{\gamma\gamma}^{max}}$ respectively, are shown.

1.2.1 Phenomenological characterization

Energy of the photons

The flux of equivalent photons from a charged particle is determined from the Fourier transform of the electromagnetic field of the moving charge. The fields of a relativistic particle Lorentz contract toward a co-moving pancake (see Fig. 1.2). Photons emitted by ions are coherently radiated by the whole nucleus, imposing a limit on the minimum photon wavelength greater than the nuclear radius. In the transverse plane, where there is no Lorentz contraction, the uncertainty principle sets an upper limit on the transverse momentum of the photon emitted by the ion A of $p_T \lesssim \hbar c/R_A \approx 28$ (330) MeV/c for Pb (p) beams. In the longitudinal direction the maximum possible momentum is multiplied by a Lorentz factor γ_L, due to the Lorentz contraction of the ions in that direction: $p_{//} \lesssim \hbar c\gamma_L/R_A$. Therefore the maximum γ-γ interaction energy in a symmetric AA collision is $2\hbar c\gamma_L/R_A$, about 6 GeV at the Relativistic Heavy ion Collider (RHIC) and 200 GeV at the Large Hadron Collider (LHC). It is worth noting that the photon flux decreases exponentially above a cutoff energy determined by the size of the nucleus. In the laboratory frame, the cutoff is $k_{max} \approx \gamma\hbar c/R_A$. In the rest frame of the target nucleus, the cutoff is boosted to $E_{max} = (2\gamma_L^2 - 1)\hbar c/R_A$, about 500 GeV at RHIC and 1 PeV at the LHC. In Tab. 1.1 a prediction of the available energies in sever colliding systems is reported, as computed few years ago in [3] before the data taking started.

Virtuality of the photons

In these collisions, the accelerated ion is surrounded by a cloud of almost real photons of virtuality $|q^2| < (\hbar c/R_A)^2$. The virtuality smaller than (60 MeV)^2 for nuclei with $A > 16$ can be neglected. Since the photon interaction is long range, photons can interact with partons in the opposite nucleus even when the nuclei themselves do not interpenetrate. Since the photon ener-

gies are less than those of the nucleons, these photonuclear interactions have a smaller average center of mass energy than hadronic parton–parton collisions. Although these photons are nearly real, their high energy allows interactions at high virtualities, Q^2, in the photon–parton center of mass. Thus, as will be better explained in Sec. 1.3, massive vector mesons, heavy quarks and jets can be produced with high rates in UPCs.

1.2.2 The formalism in the Weiszsäcker-Williams approximation

The photon flux is evaluated in the impact parameter space, as is appropriate for heavy ion interactions. For a given impact parameter **b**, the flux of virtual photons with photon energy k is strongly dependent on the Lorentz factor γ_L. At the LHC the Lorentz factor in the laboratory frame γ_L is 7455 for proton-proton, 4690 for proton-lead, 2930 for lead-lead collisions. The relationship between the Lorentz contraction factor associated with the relative velocity between the colliding nuclei and the collider energy per nucleon, E/A, in GeV, is given by $\gamma = 2\gamma_L^2 - 1) \approx 2(1.0735E/A)^2$. The equivalent (or virtual) photon flux is given integrating the following relation:

$$\frac{dN_\gamma(k)}{dk} = \int \frac{d^3N_\gamma(k,\mathbf{b})}{dkd^2b} d^2b, \tag{1.3}$$

where the integrand, the photon flux per unit of area and energy, is an expression strongly dependent from the adiabaticity parameter $\zeta = kb/\gamma$ [13]:

$$\frac{d^3N_\gamma(k,\mathbf{b})}{dkd^2b} = \frac{Z^2\alpha_{em}\zeta^2}{\pi^2kb^2}\left[K_1^2(\zeta) + \frac{1}{\gamma_L}K_0^2(\zeta)\right] \tag{1.4}$$

which drops off exponentially for $\zeta > 1$, above a cutoff energy determined essentially by the size of the nucleus, $E_{cutoff} \sim \gamma\,\mathrm{MeV}/b$ (fm). This formula is a linear combination of modified Bessel functions K_i with coefficients depending on the the QED coupling $\alpha_{em} = 1/137$ and the square of ion charge Z. The photon flux for heavy ions at RHIC and at LHC (at the nominal energies foreseen in the machine project) is depicted in Fig. 1.3. Also shown, for a comparison, is the flux for the proposed electron-ion collider at RHIC and eRHIC as computed in [3].

For symmetric nucleus-nucleus (AA) collisions, such as $Pb-Pb$ collisions at the LHC, each nucleus can act equally as source or target of the photon flux. Integrating $d^3N_\gamma(k,\mathbf{b})/dkd^2b$ over impact parameters with the constraint of no hadronic interactions and accounting for the photon polarization yields, the total photon flux $dN_\gamma^Z(k)/dk$ is given by:

$$\frac{dN_\gamma^Z(k)}{dk} = 2\pi\int_{2R_A}^{\infty} bdb \int_0^R \frac{rdr}{\pi R_A^2}\int_0^{2\pi} d\phi \frac{d^3N_\gamma(k,b+r\cos\phi)}{dkd^2b}, \tag{1.5}$$

where R_A is the radius of the nucleus.

In the case of proton-nucleus (pA) collisions, the nucleus acts preferentially as the source and the proton as the target, leading predominantly to γp processes. Nevertheless there is still a small contribution from γA processes in which the proton acts as source of photons and the nucleus as the target. Thus, the expression for both types of fluxes are required for pA collisions. The flux due to the nucleus can be evaluated analytically and is given by [13]:

$$\frac{dN_\gamma^Z(k)}{dk} = \frac{2Z^2\alpha_{em}}{\pi k}\left\{\zeta_R^{pA}K_0(\zeta_R^{pA})K_1(\zeta_R^{pA}) - \frac{(\zeta_R^{pA})^2}{2}\left[K_1^2(\zeta_R^{pA}) - K_0^2(\zeta_R^{pA})\right]\right\}, \tag{1.6}$$

with reduced adiabaticity parameter, ζ_R^{pA}, given by $\zeta_R^{pA} = k(R_A + R_p)/\gamma$ and R_p the effective radius of the proton. The flux due to the proton is usually estimated using the dipole formula

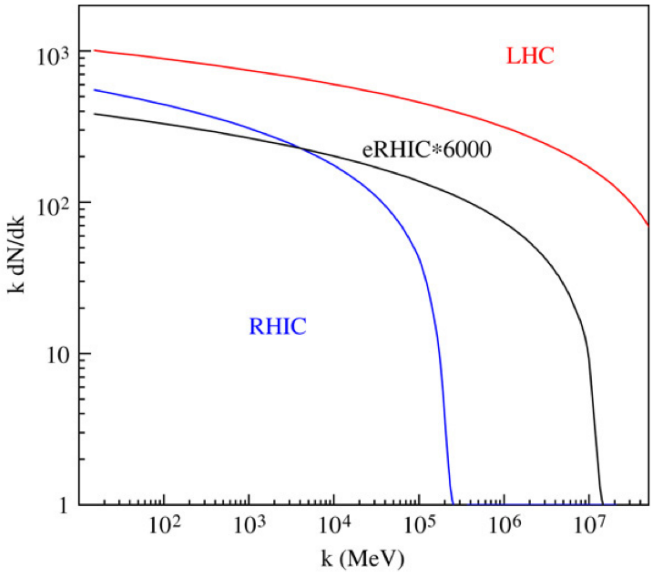

Figure 1.3 The photon flux from $\sqrt{s_{NN}}$= 200 GeV $Au-Au$ collisions at RHIC and $\sqrt{s_{NN}}$= 5.5 TeV $Pb-Pb$ collisions at the LHC, compared with that expected for 10 GeV+100 GeV $e-Au$ collisions at the proposed eRHIC [3]. The eRHIC curve has been multiplied by 6000 to account for improved gold beam parameters at eRHIC. k is given in the rest frame of the target nucleus in all three cases.

for the electric from factor [14]:

$$\frac{dN_\gamma^p(k)}{dk} = \frac{\alpha_{em}}{2\pi k}\left[1+\left(1-\frac{2k}{\sqrt{s_{NN}}}\right)^2\right]\left(\ln D - \frac{11}{6} + \frac{3}{D} - \frac{3}{2D^2} + \frac{1}{3D^3}\right), \tag{1.7}$$

where $D = 1+[0.71\ \text{GeV}^2/Q^2_{min}]$ and the minimum 4-momentum transferred is

$$Q^2_{min} = \frac{k^2}{\gamma^2(1-\frac{2k}{\sqrt{s_{NN}}})}. \tag{1.8}$$

With the knowledge of the photon flux, any generic total photoproduction cross section can be expressed as a convolution of a process cross section $\sigma^X_\gamma(k)$ and the photon flux dN_γ/dk. Thus for AA collisions:

$$\sigma^X = 2\int dk \frac{dN^Z_\gamma(k)}{dk}\sigma^{\gamma A\to X}(k), \tag{1.9}$$

with the flux given by Eq. 1.5. The factor 2 accounts for the source/target symmetry present in AA collisions. In the case of pA collisions, we have

$$\sigma^X = \int dk \left[\frac{dN^Z_\gamma(k)}{dk}\sigma^{\gamma p\to X}(k) + \frac{dN^p_\gamma(k)}{dk}\sigma^{\gamma A\to X}(k)\right], \tag{1.10}$$

with dN^Z_γ/dk and dN^p_γ/dk given by Eqs. 1.6 and 1.7, respectively.

In the Eq. 1.4 the effective photon flux is proportional to the square of the charge, Z^2, and thus significantly enhanced for heavy ions. Usually, this is better translated into an effective luminosity $L_{AB}dN_\gamma(k)/dk$, where L_{AB} is the accelerator luminosity. Fig. 1.4(a) compares $L_{AB}dN_\gamma(k)/dk$ for γp and γPb collisions in $p-Pb$ interactions to the case where the photon is emitted from an ion in a Pb-Pb collision. Fig. 1.4(b) compares the same quantity for $\gamma\gamma$ collisions [15].

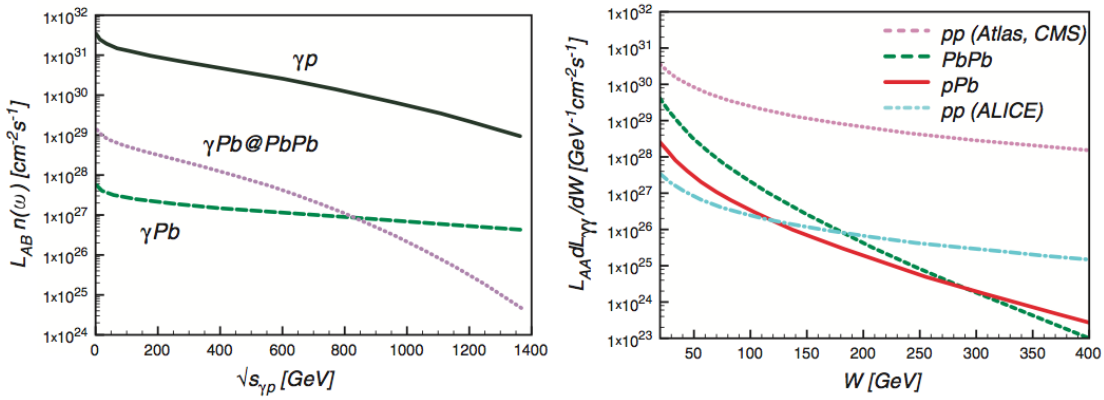

Figure 1.4 Left: effective γA luminosity for three cases at the LHC: the photon is emitted from the proton (labelled γPb), from the ion (γp) and from the ion in a $Pb-Pb$ collision ($\gamma Pb@PbPb$). Right: effective two-photon luminosities for $p-p$, $p-Pb$ and $Pb-Pb$ collisions at the LHC. In the notation adopted here, $k \equiv \omega$, $n(\omega) \equiv n(k) = dN_\gamma(k)/dk$ and $W \equiv \sqrt{s_{\gamma\gamma}}$ [15].

1.3 Photoproduction cross section in photonuclear processes

In this section the main ideas related to the physics of photonuclear production are extensively introduced: starting from the treatise of the photoproduction of heavy quarks (Par. 1.3.2), the photoproduction of vector mesons will be explained (Par. 1.3.3), in relation to the knowledge of parton distributions in nuclei and photons (Par. 1.3.4). These concepts will be introductory for the reading of Par. 1.4, where the consequences of the theory of leading-twist (LT) nuclear shadowing for UPCs are mentioned. The approach followed here, is mainly based on the computations derived in [4, 5]. These predictions will be actually illustrated, in comparison with the experimental results, in the last chapter of this thesis.

1.3.1 Why to study photoproduction in UPCs

Photoproduction processes in UPCS at hadron colliders offer the possibility of a direct determination of the gluon distribution in nucleons and nuclei. Examples of interactions in which the gluon distribution can be probed are exclusive production of heavy vector mesons and photoproduction of heavy quark-antiquark pairs. The gluon distributions are not directly accessible in deep inelastic scattering, because the gluons carry neither electrical nor weak charge. Measuring the nuclear shadowing using heavy-ion beams is particularly interesting. The nuclear gluon density, in a naive approximation, can be written as the nucleon gluon distribution, $g_N(x,Q^2)$, multiplied by the number of nucleons (A):

$$g_A(x,Q^2) = A g_N(x,Q^2), \tag{1.11}$$

with x being the fraction of the projectile momentum carried by the gluon, and Q^2 is the 4-momentum transfer squared.

Results from deep inelastic scattering of electrons on nuclear targets, however, have showed deviations from such a simple scaling for the structure function, $F_2(x,Q^2)$. Depending on x, suppressions (shadowing) of up to $\sim 30\%$ and enhancements (anti-shadowing) of up to $\sim 10\%$ have been observed [2]. The effects of shadowing on $g_A(x,Q^2)$ are hard to determine directly. The current best estimates of the modification to the gluon distribution in nuclei are obtained from the Q^2 evaluation of $F_2(x,Q^2)$ and from studies of diffractive interactions [17]. Photoproduction at heavy-ion colliders can provide a more direct measurement of $g_A(x,Q^2)$.

1.3.2 Photoproduction of heavy quarks

From the viewpoint of a Fock space decomposition, photon interactions with hadrons and nuclei can be classified as direct or resolved. In direct interactions, the photon behaves as a point-like particle ("bare photon"), while in resolved interactions the photon fluctuates into a quark-antiquark state or an even more complex partonic configuration consisting of quarks and gluons. The cross section for the photoproduction of a pair of heavy quarks, $\sigma^{\gamma H\to Q\bar{Q}X}(k)$, is thus a sum of both the direct and resolved contributions,

$$\sigma^{\gamma H\to Q\bar{Q}X}(k) = \sigma^{\gamma H\to Q\bar{Q}X}_{direct}(k) + \sigma^{\gamma H\to Q\bar{Q}X}_{resolved}(k) \tag{1.12}$$

Here H stands for a proton or a nucleus ($H = p, A$) and the total photoproduction cross section is obtained by convoluting the equivalent photon flux, $dN_\gamma(k)/dk$, with $\sigma^{\gamma H\to Q\bar{Q}X}(k)$, as described by Eqs. 1.9 and 1.10 for AA and pA collisions, respectively.

Let us now consider both processes in some detail. At leading order (LO), photon-gluon fusion leading to the production of a heavy quark pair is the only subprocess relevant to direct photoproduction. In view of the high Q^2 involved, perturbative QCD is applicable, and the direct photoproduction cross section can be expressed as a convolution of the partonic cross section for the subprocess $\gamma g \to Q\bar{Q}$ and the relevant nucleon or nuclear gluon distribution:

$$\sigma^{\gamma H\to Q\bar{Q}X}_{direct}(s) = \int dx \sigma^{\gamma g\to Q\bar{Q}}(\hat{s}) f_g^H(x,Q^2)\Theta(\zeta). \tag{1.13}$$

Being m_Q the heavy quark mass (charm or bottom), $s = W^2_{\gamma H}$ denotes the square of the center of mass energy of the photon-nucleus (or photon-nucleon) system, $\hat{s} = W^2_{\gamma g}$ that of the photon-gluon system, and $\zeta = \hat{s} - 4m_Q^2$. The gluon distribution in H, $f_g^H(x,Q^2)$, is evaluated at the pQCD factorization scale [2] $Q^2 = W^2_{\gamma g} = \hat{s}$. The function $\Theta(\zeta)$ enforces a minimum ("threshold") value of x, x_{min}, on the integral given by $x_{min} = 4m_Q^2/W^2_{\gamma H}$. The partonic photon-gluon fusion cross section is given by [19]:

$$\sigma^{\gamma g\to Q\bar{Q}}(\hat{s}) = \frac{2\pi\alpha_{em}\alpha_s(Q^2)e_Q^2}{\hat{s}}\left[\left(1+\beta-\frac{\beta^2}{2}\right)\ln\left(\frac{1+\nu}{1-\nu}\right) - (1+\beta)\nu\right] \tag{1.14}$$

with e_Q the electric charge of the heavy quark Q, α_{em} and α_s the electromagnetic and strong coupling constant respectively, $\beta = 4m_Q^2/\hat{s}$, and $\nu = \sqrt{1-\beta}$.

The resolved contribution is identical to the hadroproduction of heavy quarks, and at leading order, involves terms corresponding to gluon-gluon and quark-antiquark subprocesses. The

[2] The QCD factorization theorem provides a description for separating long-distance and short-distance effects in hadronic cross sections. The leading power contribution to a general hadronic cross section involves only one hard collision between two partons from the incoming particles (*i.e.,hadron-hadron, photon.hadron, ...*) with momenta p_A and p_B. The cross section can be factorized as [16]:

$$E_h\frac{d\sigma_{AB\to h(p')}}{d^3p'} = \sum_{ijk}\int dx' f_{j/B}(x')\int dx f_{i/A}(x)\int dz D_{h/k}(z) E_h\frac{d\hat{\sigma}_{ij\to k}}{d^3p'}\left(xp_A, x'p_B, \frac{p'}{z}\right),$$

where $\sum_{ijk}$ runs over all parton species and all scale dependence is implicit. The $f_{i/A}$ are twist-2 distributions of parton type i in hadron A (parton distribution functions, PDFs) and the $D_{h/k}$ are fragmentation functions for a parton of type k to produce a hadron h.

resolved cross section can be written as

$$\sigma_{resolved}^{\gamma H\to Q\bar{Q}X}(s)=\int dx_1dx_2\Bigg\{f_g^{\gamma}(x_1,Q^2)f_g^{H}(x_2,Q^2)\sigma^{gg\to Q\bar{Q}}(\hat{s}) \\ +\sum_q f_q^{\gamma}(x_1,Q^2)\left[f_q^{H}(x_2,Q^2)+f_{\bar{q}}^{H}(x_2,Q^2)\right]\sigma^{q\bar{q}\to Q\bar{Q}}(\hat{s})\Bigg\}\Theta(\zeta) \tag{1.15}$$

where $f_a^{\gamma}(x_1,Q^2)[f_a^{H}(x_2,Q^2)]$ is the distribution of parton a with momentum fraction $x_1(x_2)$ in a photon (H), respectively, $\hat{s}=x_1x_2s$ and $\zeta=\hat{s}-4m_Q^2$. The summation over q runs over the light flavors; i.e., $q=u,d,s$. The partonic cross sections are given by [20]:

$$\sigma^{gg\to Q\bar{Q}}(\hat{s})=\frac{\pi\alpha_s^2(Q^2)}{3\hat{s}}\left[\left(1+\beta+\frac{\beta^2}{16}\right)\ln\left(\frac{1+\nu}{1-\nu}\right)-\left(\frac{7}{4}+\frac{31}{16}\beta\right)\nu\right] \tag{1.16}$$

and

$$\sigma^{q\bar{q}\to Q\bar{Q}}(\hat{s})=\frac{8\pi\alpha_s^2(Q^2)}{27\hat{s}}\left[\left(1+\frac{\beta}{2}\right)\sqrt{1-\beta}\right] \tag{1.17}$$

Here, β and ν are as defined previously.

It is often more enlightening to represent the cross section in terms of rapidity, that is, to consider rapidity distributions. The differential cross section with respect to the rapidity of the heavy quark pair, $d\sigma/dy$, is related to the differential cross section with respect to photon energy, $d\sigma/dk$, through the relation $d\sigma/dy=kd\sigma/dk$. The rapidity distribution can, therefore, be expressed as:

$$\frac{d\sigma^{\gamma H\to Q\bar{Q}X}}{dy}=k\frac{dN_{\gamma}(k)}{dk}\sigma^{\gamma H\to Q\bar{Q}X}(k), \tag{1.18}$$

and scales directly with the photon flux dN_{γ}/dk. Thus, for pA collisions, with the convention that the proton is incident from the right and the nucleus from the left, the total rapidity distribution is

$$\frac{d\sigma^{pA\to Q\bar{Q}X}}{dy}=\left[k\frac{dN_{\gamma}^{Z}(k)}{dk}\sigma^{\gamma p\to Q\bar{Q}X}(k)\right]_{k=k_l}+\left[k\frac{dN_{\gamma}^{p}(k)}{dk}\sigma^{\gamma A\to Q\bar{Q}X}(k)\right]_{k=k_r} \tag{1.19}$$

where $k_l(k_l\propto e^{-y})$ and $k_r(k_r\propto e^{y})$ simply denote photons from the nucleus and proton, respectively, and the fluxes dN_{γ}^{Z}/dk and dN_{γ}^{p}/dk are given by Eqs. 1.6 and 1.7. As remarked earlier, the fluxes have support only at small values of k, dying out exponentially at large k. Thus, the first term on the right-hand side (γp distribution) peaks at positive rapidities, while the second term (γA distribution) peaks at negative rapidities. Since both the fluxes and process cross sections are different, the total distribution is manifestly asymmetric, and the γp term dominates due to the much larger nuclear flux dN_{γ}^{Z}/dk.

The total rapidity distribution for AA collisions can likewise be written as

$$\frac{d\sigma^{AA\to Q\bar{Q}X}}{dy}=\left[k\frac{dN_{\gamma}^{Z}(k)}{dk}\sigma^{\gamma p\to Q\bar{Q}X}(k)\right]_{k=k_l}+\left[k\frac{dN_{\gamma}^{Z}(k)}{dk}\sigma^{\gamma A\to Q\bar{Q}X}(k)\right]_{k=k_r} \tag{1.20}$$

with $k_l(k_r)$ simply denoting photons from the nucleus incident from the left(right) and the flux dN_{γ}^{Z}/dk given by Eq. 1.5. Here the process cross sections and the left/right fluxes are identical; thus, the respective rapidity distributions are mirror images of each other and, consequently, the total distribution is symmetric about midrapidity ($y=0$).

1.3.3 Exclusive photoproduction of vector mesons

The dominant coherent interaction leading to the production of a hadronic final state is the exclusive production of vector mesons,

$$H + H \rightarrow H + H + V$$

where $H \equiv p, A$. One speaks of coherent photoproduction only when the photon from the electromagnetic field of one of the projectiles interacts coherently with the nuclear field of the ion A, that is $\lambda_\gamma \sim R_A$, producing in the final state a vector meson V. The most likely case in which this happens is when considering AA collisions, as in this thesis. Exclusive vector meson photoproduction on proton and nuclear targets has been studied since the mid-1960s using photon beams and since 1992 at the HERA electron-proton accelerator [2]. The first results from a heavy-ion collider on exclusive ρ^0 production ($Au + Au \rightarrow Au + Au + \rho^0$) were recently published by the STAR Collaboration at RHIC [18].

The bulk of the photon-hadron cross section can be explained by the photon first fluctuating to a $Q\bar{Q}$ pair, which interacts with the target through the gluon exchange. Since the photon has quantum numbers $J^{PC} = 1^{--}$, it preferentially fluctuates into a vector meson. The lifetime of the fluctuation is determined by the uncertainty principle. For a photon of virtuality q fluctuating to a state of mass M_V the lifetime is:

$$\Delta t \approx \frac{\hbar}{\sqrt{M_V^2 c^4 + q^2 c^2}} \approx \frac{\hbar}{M_V c^2}.$$

The last approximation is always true at hadron colliders due to the low virtuality of the photons. The cross section for the exclusive elastic photoproduction of a vector meson V on H ($H \equiv p, A$) can be written as:

$$\sigma^{\gamma H \rightarrow VH}(k) = \left.\frac{d\sigma^{\gamma H \rightarrow VH}}{dt}\right|_{t=0} \int dt |F_H(t)|^2, \tag{1.21}$$

where $d\sigma^{\gamma H \rightarrow VH}/dt|_{t=0}$ is the forward scattering amplitude, $F_H(t)$ is the form factor and t is the momentum transfer from the target nucleus squared. The dynamical information is encoded in the forward scattering amplitude while the momentum transfer of the elastic scattering is determined by the form factor which is, in general, dependent on the spatial attributes of the target H.

There have been studies of the photoproduction of J/ψ and Υ in ultra-peripheral collisions at LHC (see, for instance, Refs.[3, 24]). In this discussion, what is adopted is the simple amplitude calculated from leading-order two-gluon exchange in perturbative QCD [25] and corrected for other relevant effects - such as relativistic corrections, inclusion of the real part of the scattering amplitude, next-to-leading order (NLO) effects, etc., see [26] - through a phenomenological multiplicative correction factor ζ_V, as did in [4].

For elastic photoproduction on protons, the corrected LO amplitude can be written as

$$\left.\frac{d\sigma^{\gamma p \rightarrow Vp}}{dt}\right|_{t=0} = \zeta_V \frac{16\pi^3 \alpha_s^2 \Gamma_{ee}}{3\alpha_{em} M_V^5} [x g_p(x, Q^2)]^2. \tag{1.22}$$

Here, M_V is the mass of the vector meson (J/ψ and $\Upsilon(1s)$ in this case), $x = M_V^2/W_{\gamma p}^2$ is the fraction of the nucleon momentum carried by the gluons, and $g_p(x, Q^2)$ is the gluon distribution in a proton, evaluated at a momentum transfer $Q^2 = (M_V/2)^2$. Γ_{ee} is the leptonic decay width of the vector meson. This quantity has been extensively measured in the case of J/ψ meson [21] and the most recent fit, performed by [22], is depicted in Fig. 1.5. The previous equation can be

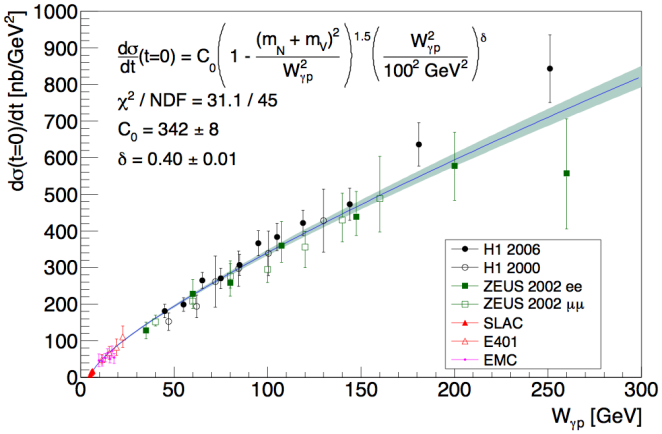

Figure 1.5 Fit performed by [22] to the forward J/ψ photoproduction cross section data published by [21]

easily generalized to the nuclear case,

$$\left.\frac{d\sigma^{\gamma A\to VA}}{dt}\right|_{t=0} = \zeta_V \frac{16\pi^3\alpha_s^2\Gamma_{ee}}{3\alpha_{em}M_V^5}[xg_A(x,Q^2)]^2, \tag{1.23}$$

where

$$g_A(x,Q^2) = g_p(x,Q^2)\times R_g^A(x,Q^2) \tag{1.24}$$

is the nuclear gluon distribution obtained mapping the proton gluon distribution with the gluon modification function $R_g^A(x,Q^2)$. The correction factor ζ_V is usually estimated by constraining the computed cross sections for elastic vector meson photoproduction on protons, $\sigma^{\gamma p\to Vp}(W_{\gamma p})$, to reasonably reproduce the photoproduction data from HERA, as did in [6]. It is worth noting that in contrast to photoproduction of heavy quarks, the quadratic dependence of the cross section on the gluon distribution has the significant implication of making exclusive vector meson production a very sensitive probe of nuclear gluon modifications. Consequently, the priority within the ALICE UPCs research program is the collection of data related to the signal of photoproduced vector mesons, as it will be discussed in the last chapter.

Few considerations concerning the momentum-squared transferred dependence ($t-$dependence) of the cross section: for a proton, the standard practice is to parametrize the $t-$dependence in the form of a rapidly decreasing exponential function, $e^{b|t|}$, where b is referred to as the slope parameter. Integrating this function with respect to t gives a multiplicative factor $1/b$ with units GeV^2. In the case of a nucleus, the nuclear form factor is given by the Fourier transform of the nuclear density distribution:

$$F_A(t) = \int d^3r\rho_A(r)e^{i\mathbf{q}\cdot\mathbf{r}}, \tag{1.25}$$

where q is the momentum transferred. It is customary to model the density distribution as a Woods-Saxon distribution with parameters from electron scattering,

$$\rho_A(r) = \frac{\rho_0}{[1+e^{[(r-R_A)/d]}]}, \tag{1.26}$$

with central density ρ_0, radius R_A and skin depth d. For ^{208}Pb in use at LHC, $\rho_0 = 0.16\text{fm}^{-3}$, $R_A = 1.2A^{1/3}$ fm and $d = 0.549$ fm [23]. Since the Fourier transform of a Woods-Saxon density distribution does not admit an analytic form, it is employed a commonly used modified hard

sphere (a convolution of a hard sphere with a Yukawa term) to approximate $\rho_A(r)$ in $F(t)$ (see [6]):

$$F(q=\sqrt{|t|}) = \frac{4\pi\rho_0}{Aq^3}[\sin(qR_A) - qR_A\cos(qR_A)]\left[\frac{1}{1+a^2q^2}\right]. \tag{1.27}$$

The range of the Yukawa term a is 0.7 fm, and the form factor is a simple product of the Fourier transforms of the hard sphere and the Yukawa term.

For the proton, the photonucleon cross section $\sigma^{\gamma p\to Vp}(k)$ is obtained through

$$\sigma^{\gamma p\to Vp}(k) = \frac{1}{b}\frac{d\sigma^{\gamma p\to Vp}}{dt}\bigg|_{t=0}, \tag{1.28}$$

with slope parameter b (assumed to be 4.5 GeV^{-2} in [4]). The photonuclear cross section is given by

$$\sigma^{\gamma A\to VA}(k) = \frac{d\sigma^{\gamma A\to VA}}{dt}\bigg|_{t=0}\int_{t_{min}(k)}^{\infty} dt|F(t)|^2. \tag{1.29}$$

Here, $t_{min}(k) = (M_V^2/4k\gamma_L)^2$, as is appropriate for narrow resonances [27]. The total cross sections for pA and AA collisions are obtained by a convolution of $\sigma^{\gamma p\to Vp}(k)$ and $\sigma^{\gamma A\to VA}(k)$ with the relevant photon flux as described in Par. 1.2.2. It is worth noting that the photon energy, k, is related to the rapidity of the vector meson y by

$$k = \frac{M_V}{2}e^y, \tag{1.30}$$

a very important relation to be considered when collecting data at different rapidities. Thus, as in the case of photoproduction of heavy quarks, the differential cross section with respect to rapidity is given by

$$\frac{d\sigma^{\gamma H\to VH}}{dy} = k\frac{dN_\gamma(k)}{dk}\sigma^{\gamma H\to VH}(k), \tag{1.31}$$

and the corresponding expressions for rapidity distributions in pA and AA collisions are of the form given by Eqs. 1.19 and 1.20. The symmetry attributes of the distributions are also similar.

1.3.4 Parton distributions in nuclei and photons

As mentioned earlier, the direct contribution to the photoproduction of heavy quarks is dependent solely on the gluon distributions in protons and nuclei, same as for the elastic photoproduction of vector mesons. The resolved contribution, on the other hand, requires the distributions of light quarks and antiquarks and gluons in photons, protons, and nuclei. Thus, in addition to the usual requirement of nucleon and nuclear parton distributions (nPDs), there is also the need for the relatively poorly known parton distributions in photons (γPDs), thereby increasing the level of the theoretical uncertainties in the calculation of photoproduction of heavy quarks. Although the direct contribution is dominant, this dominance does not make weaker the need to have a good control on the resolved contribution.

Parton distributions in nuclei

It is rather well-known that the distributions of partons (*i.e.*, quarks and gluons) in nuclei are quite different from the distributions in free nucleons; that is, they are "modified" by the complex, many-body effects in the nucleus. These nuclear effects are usually parametrized in terms of "nuclear modifications" $R_a^A(x,Q^2)$, which, in general, depend on the parton specie a, the nucleus A, momentum fraction x, and scale Q^2. The nuclear effects can be categorized based on

different intervals in x. At small values of x ($x \lesssim 0.04$), we have the phenomenon generally referred to as shadowing. This is a depletion, in the sense that in this interval, the distribution of a parton a in the nucleus is smaller compared to the corresponding distribution in a free proton, *i.e.*, $R_a^A < 1$. Antishadowing, which is an enhancement ($R_a^A > 1$), occurs in the range $0.04 \lesssim x \lesssim 0.3$. Another depletion, the classic EMC effect [28], is present in the interval $0.3 \lesssim x \lesssim 0.8$, while for $x > 0.8$, the Fermi motion region, we have another enhancement. It is important to note that although both shadowing and the EMC effect (antishadowing and Fermi motion) correspond to depletion (enhancement), the physical principles and mechanisms governing these phenomena are quite different. With the knowledge of $R_a^A(x,Q^2)$, nuclear parton distributions can be expressed as a convolution of free nucleon parton distributions and nuclear modifications, *i.e.*, $f_a^A(x,Q^2) = f_a(x,Q^2) \otimes R_a^A(x,Q^2)$.

While the determination of quark and antiquark distributions in nucleons and nuclei is, in general, a nontrivial task, that of gluons is even more problematic. Gluons are electrically neutral, and thus their distributions cannot be extracted directly from deeply inelastic scattering (DIS) and Drell-Yan (DY) processes, which account for the major part of the data used in global fits. Their distributions are, in general, inferred from sum rules and the Q^2 evolution of sea quarks distributions. The situation is even worse in the nuclear case: the available data is much less than for nucleons, and there is the added complication of a mass dependence. It is, therefore, not unusual for nuclear gluon distributions from different global fits to differ significantly, especially in the magnitude of the various nuclear effects (shadowing, antishadowing, etc.). This is especially obvious at low Q^2 (*i.e.*, around their initial starting scales) since evolution to high Q^2 tends to lessen the differences. Earlier global analyses [29] relied heavily on fixed-target nuclear DIS and DY lepton-pair production. Incorporation of data on inclusive hadron production in deuteron-gold collisions has been implemented in Ref. [30], and neutrino-iron data in Ref. [31]. It is worth mentioning also the approach in Ref. [32] utilizing the Gribov picture of shadowing. Despite all these advances, the nuclear gluon distribution is still currently the least constrained aspect of global fits to nuclear parton distributions, as significant uncertainties still persist at both small and large x.

Five recent nucleon and nuclear parton distributions are mostly utilized in literature [4] . For the single proton, the Martin-Stirling-Thorne-Watts (MSTW08) parton distributions [33] are available and constrained by a large number of data - especially from HERA and the Tevatron- in global fits performed up to next-to-next-to-leading order (NNLO). The distributions from MSTW08 serve two purposes: as the free nucleon distributions used in conjunction with nuclear modifications and also as a "special nuclear distribution in the absence of nuclear effects. The latter case is particularly useful for highlighting the influence of the various nuclear effects on observables. In the nuclear case, much less extensive experimental data on nuclear DIS are available in the perturbative region ($Q^2 \gtrsim 1$ GeV^2), only for $x \gtrsim 0.01$. As a result, there are large uncertainties in the nPDFs relevant for LHC kinematics. Some recent version for nPDFs are consequently introduced. Two sets are by Eskola, Paukunnen, and Salgado, namely EPS08 and EPS09[34, 35]. The third is the Hirai-Kumano-Nagai (HKN07) distributions [36] and the last one is derived by D. de Florian and R. Sassot (nDS) in [37]. While EPS08 is only to leading order (LO), both EPS09, HKN07 and nDS are available as global fits of data on charged leptons DIS with nuclear Drell-Yan in proton nucleus collisions, up to next-to-leading order (NLO) [4, 15].

It is instructive to compare the characteristics of the gluon distributions from the four aforementioned sets based on the strength of their nuclear modifications. In Fig. 1.6 we show the nuclear modifications for gluons in Pb, $R_g^{Pb}(x,Q^2)$ from EPS08, EPS09, and HKN07 at the factorization scale $Q^2 = M_{J/\psi}^2$, appropriate for the elastic photoproduction of the J/ψ meson. As

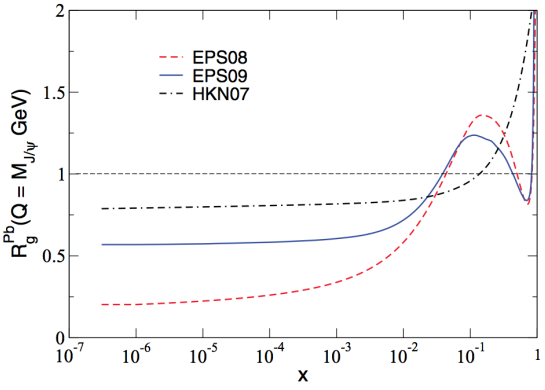

Figure 1.6 Ration of bound over free proton gluon distributions (nucler gluon modifications) in Pb, $R_g^{Pb}(x, Q^2 = M_{J/\psi}^2)$), from EPS08 (dashed line), EPS09 (solid line) and HKN07 (dashed-dotted line), respectively [4]

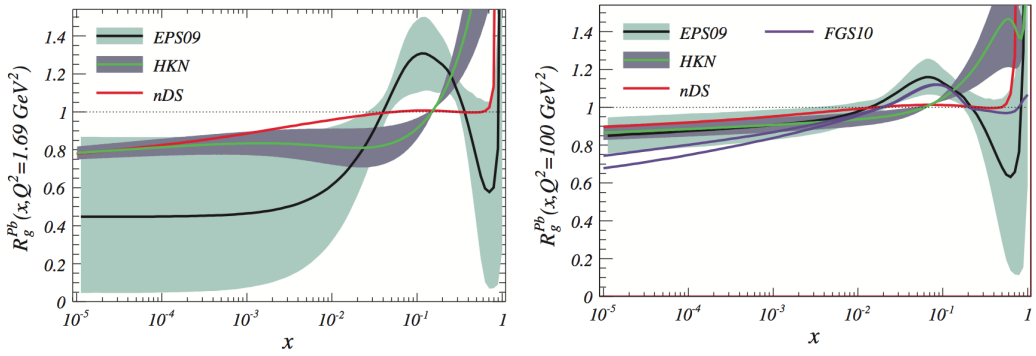

Figure 1.7 Nuclear PDFs shown again as the ratio $R_g^{Pb}(x, Q^2)$ (here the uncertainties have also been included). They were obtained by NLO global fits EPS09, HKN07 and nDS at two different virtualities, $Q^2 = 1.69$ GeV^2 and $Q^2 = 100$ GeV^2. Also shown for $Q^2 = 100$ GeV^2 are the results from FGS10 in which gluon shadowing is computed from DIS diffraction cross section measured at HERA [15]. .

already stated, one can view the MSTW08 gluon distribution as a nuclear gluon distribution in the limit of zero nuclear effects ($R_a^A = 1$). At this scale, HKN07 has a rather weak gluon shadowing, which extends well into the antishadowing region, no antishadowing and gluon EMC effect, and an early onset of Fermi motion. EPS09 exhibits a moderately strong shadowing and appreciable antishadowing and EMC effect, with a quite strong Fermi motion. Nuclear modifications are strongest in EPS08: an especially strong shadowing and substantial antishadowing, EMC, and Fermi motion. Thus, in terms of shadowing we have a progression from zero effects to weak effects, moderate (intermediate) effects, then to strong effects as one progresses from MSTW08 to EPS08. The issue of uncertainties in parton distributions is becoming increasingly important, especially in relation to precision tests of QCD. Discussions on uncertainties in nuclear parton distributions can be found in Refs. [34, 35, 36]. In spite of these successes, the gluon distribution remains poorly constrained for the nucleus, as can be seen in a more recent computation reported by [15] (Fig. 1.7) where different sets of nPDFs are shown together with the corresponding uncertainty bands. DGLAP evolution is, however, very efficient in removing the nuclear effects for gluons at small$-x$, which quickly disappear for increasing Q^2. In this way, these uncertainties become smaller for the hardest available probes except for the large$-x$ region where substantial effects could survive for large virtualities (not the case of vector meson photoproduction in ultra-peripheral $Pb-Pb$ collisions). This region is, however, dominated by valence quarks which in turn are rather well constrained by DIS data with nuclei. An alternative

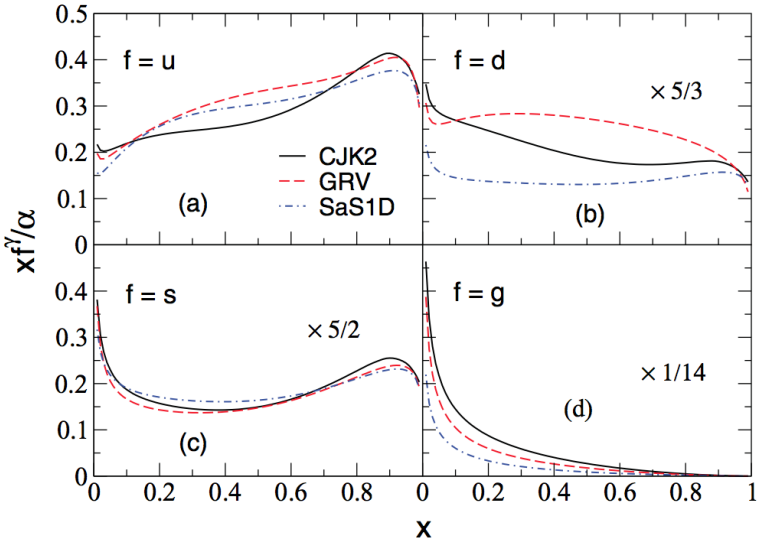

Figure 1.8 Parton distributions in the photon for *(a)* up, *(b)* down, *(c)* strange quarks, and *(d)* gluons at $Q^2 = 10$ GeV^2 for three distribution sets: CJK2 (solid line), GRV (dashed line), and SaS1d (dash-dotted line), respectively. For better visuality, the down quark distributions *(b)* have been enhanced by a factor of 5/3, the strange quark distributions *(c)* by 5/2, and the gluon distributions *(d)* by 1/14 [4]. .

approach, called FGS10 ([38]) computes the small-x shadowing by its connection to the hard diffraction in electron-nucleon scattering. It has been used to obtain the nuclear PDF at an initial scale Q_0 which are then evolved by NLO DGLAP equations. The inputs in this calculation are the diffractive PDFs measured in DIS with protons at HERA. These distributions are dominated by gluons, resulting in a stronger shadowing for gluons than the corresponding one for quarks. In Fig. 1.7, the results from this approach for the gluon case are also plotted. The differences at small$-x$ become even larger at smaller virtualities (not shown) [38].

Finally, it is worth noting that in contrast to the RHIC, where there are constraints at mid-rapidity ($x \gtrsim 10^{-2}$) for nuclear distributions from DIS and DY data, the LHC probes completely unexplored regions of phase space. This complicates the interpretation of the $Pb-Pb$ LHC data, as it will be better shown at the end of this chapter. A more extended knowledge of the gluon nPDFs from the analysis of UPCs and, independently, from the ongoing analysis of data of the $p-Pb$ benchmarking program started at the beginning of 2013 will be partially remove these uncertainties.

Parton distributions in photons

Parton distributions in photons (γPDs) are derived from experimentally determined photon structure function $F_2^\gamma(x,Q^2)$, in conjunction with appreciable theoretical inputs. These inputs, which are necessary in implementing the parametrizations of photon parton distributions from the structure function, account in part for some of the observable differences in the available photon parton distribution sets. Another source of differences is in the choice and scope of experimental data from which F_2^γ is extracted. At present there is an appreciable number of photon parton distribution sets available, both at leading and next-to-leading orders. It should be noted that unlike in the case of a nucleon, there are no valence quarks present in the photon; therefore, antiquark distributions are the same as quark distributions. Furthermore, there are no sum rules governing the gluon content; thus, the gluon distribution is almost totally unconstrained. The gluon distribution is a major contributor to $F_2^\gamma(x,Q^2)$ through the $\gamma^* g \to q\bar{q}$ channel, which has

significant numerical support only at small x.

In light of the relatively poor known situation, especially in the gluon sector, different photon parton distribution sets have been used in phtoproduction cross section studies. Two sets are relatively older and have been in common use: the Gluck-Reya-Vogt (GRV) set [39] and that by Schuler and Sjostrand (SaS1d) [40]. The third set, the Cornet-Jankowski-Krawczyck (CJK2) set [41], is more recent and has facility to estimate error on a calculated quantity due to the uncertainties in the input photon parton distributions. In Fig. 1.8 we show the parton distributions from these three sets for the light (u,d,s) quarks and gluon. The up quark is the best constrained component of photon parton distributions, and even in this case there are clear differences between the three sets. This is also the case for the down quark. Only for the strange quark distribution there is good agreement between the three sets. But these differences pale in comparison with that of gluons, where the differences between the sets are quite significant almost across the whole x interval, with CJK2 having the largest magnitude, while SaS1d has the lowest, with the GRV somewhat intermediate. For the LO-resolved contribution to heavy quark photoproduction, the two competing partonic subprocesses are the $gg \to Q\bar{Q}$ and $q\bar{q} \to Q\bar{Q}$, and it is thus to be expected that significant differences will arise in the resolved cross sections whenever the $gg \to Q\bar{Q}$ component is appreciable.

1.4 UPCs and "small$-x$" physics

It is now convenient to have a deeper treatise of what mentioned in the introductive motivations of Par. 1.3. High energy coherent J/ψ photoproduction on nuclei is of a particular interest since the large $c-$quark mass, m_c, provides a hard scale $Q \geq m_c$ justifying the use of the factorization theorem of perturbative QCD quoted in 1.3.2. This allowed one to develop several models predicting the cross section of J/ψ photoproduction on nuclear targets at high energies. To better figure out the features of UPCs and the reasons for which ALICE Collaboration decided to perform an UPCs research program beside the standard one, it is therefore convenient to mention about these other ideas presented in alternative theories attempting to describe the photonuclear processes (Pars. 1.4.1, 1.4.2). In prevision of the experimental results discussion of the last chapter, and their comperison with all these theories, it is very useful to summarize all the main concepts presented until now, in term of an *ad hoc* physical quantity called nuclear suppression factor, $S(W)$ (Par. 1.4.3), as did by [22].

1.4.1 Approaching the black disk regime with the LHC

Data from HERA show that the gluon and sea quark distributions rise quickly as their momentum fraction x drops. At small enough x , the power law increase of the proton parton densities may change to a slower growth proportional to powers of $\ln(1/x)$. The increase of the parton densities is regulated by phenomena such as shadowing, recombination reactions $(gg \to g)$, as well as possible tunneling between different QCD vacua that are suppressed at large x. These phenomena are most significant in the central core of a nucleon. Scattering off the periphery of the nucleon will dominate at small x, causing the cross section to increase asymptotically as fast as $\propto \ln^3(1/x)$ [42]. The large diffractive gluon densities observed at HERA demonstrate nonlinear effects for squared momentum transfer of the virtual photon of up to $Q^2 \sim 4$ GeV^2 at the smallest x values studied, $x \sim 10^{-4}$. At the LHC, these QCD phenomena are visible at larger x in central collisions of both protons and heavy ions and their knowledge is very important to separate cold nuclear matter QCD effects from the properties of the hot matter (QGP, Quak Gluon Plasma) produced and studied in ALICE.

Studies of small x deep-inelastic scattering at HERA substantially improved our understanding of strong interactions at high energies. There are several key findings of HERA in this field. Rapid growth of the small x parton densities was observed over a wide range of Q^2. A significant probability for hard diffraction was seen, consistent with approximate scaling and a logarithmic Q^2 dependence ("leading-twist" dominance). HERA also found a new class of hard exclusive processes - light vector meson production at large Q^2 and heavy $Q\bar{Q}$ vector mesons at all Q^2. These processes are described by the QCD factorization theorem [16] (see also Par. 1.3.2) and related to the generalized parton distributions in the target. In the small x limit, they can be calculated for zero squared momentum transfer, t, using standard parton distributions. This new class of interactions probes small $q\bar{q}$ dipole interactions with hadrons. The t dependence provides direct information on the gluon distribution of hadrons in the transverse plane as a function of x.

Combined analyses of inclusive DIS and hard vector meson production suggest that the strength of the interactions, especially in channels where a hard probe directly couples to low x gluons, approaches the maximum possible value – the black disk regime (BDR) – for $Q^2 \leq 4$ GeV^2. This conclusion is confirmed by studies of hard inclusive diffraction [42]. However, the Q^2 range over which the black disk regime holds is relatively small, with even smaller values for processes where a hard probe couples to a $q\bar{q}$ dipole with $Q^2 \sim 1$ GeV^2, making it difficult to separate perturbative from non perturbative effects and draw unambiguous conclusions. The interaction regime where hard probes of small target x occur with high probability should be a generic feature of strong interactions at high energies. This feature is related to high gluon densities, reached for any target at sufficiently small x. Extended targets are expected to reach this high density regime at substantially higher x. At very high gluon density, even the notion of inclusive parton densities is ill-defined.

The onset of the BDR corresponds to a drastic departure from the linear regime of QCD. Observing the onset of nonlinear QCD dynamics at small x would be of great importance. The problems which emerge in the BDR kinematics can be visualized by considering DIS interactions and exclusive diffractive processes in the language of small dipoles interacting with the target. In the leading-log approximation, the inelastic quark-antiquark (gluon-gluon) dipole-hadron cross section for a dipole of size d has the form [43]:

$$\sigma_{diph}(s_{diph}, d^2) = \frac{\pi^2}{4} C_F^2 d^2 \alpha_s(Q_{eff}^2) x g(x, Q_{eff}^2) \tag{1.32}$$

where $x = Q_{eff}^2/s_{diph}$, and s_{diph} is the square of the dipole-hadron center-of-mass energy. Here C_F^2 is the Casimir operator, equal to 4/3 for $q\bar{q}$ and 3 for gg, $\alpha_s(Q_{eff}^2)$ is the LO strong coupling constant and $g(x, Q_{eff}^2)$ is the LO gluon density in the target. The latters are evaluated at $Q_{eff}^2 \propto d^{-2}$. Since the gluon densities increase at small x, the cross section in Eq. 1.32 ultimately becomes larger than allowed by the unitarity constraint, πr_h^2, where r_h is the transverse radius of the gluon distribution in the hadron at the corresponding x. Since the unitarity bound corresponds to complete absorption at impact parameters $b \leq r_h$, the resulting diffractive cross section reflects absorption at small b. If the regime of complete absorption at $b \leq r_h$ is reached, the diffractive absorption cross section becomes nearly equal to the inelastic-scattering cross section. At sufficiently high energies, the small x gluon fields resolved by the small color dipole become so strong that the dipole cannot propagate through extended nuclear media without absorption, signaling the breakdown of the linear scaling regime of Eq. 1.32 and the onset of the BDR.

In the dipole picture, a high-energy photon can be considered to be a superposition of large and small size dipoles, as already stated in Par. 1.3.2. Smaller and smaller dipoles begin to

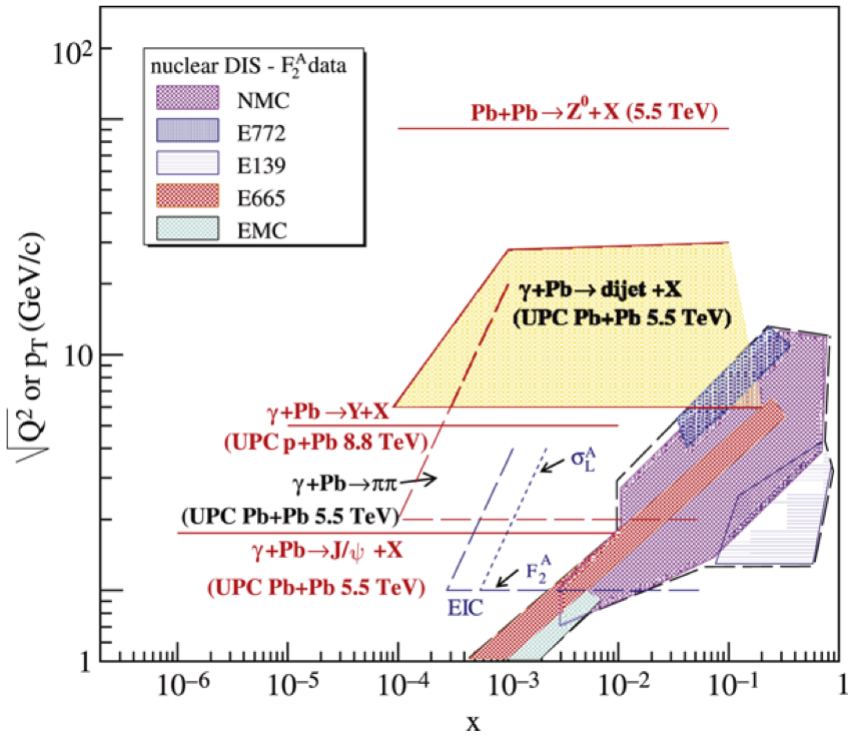

Figure 1.9 The kinematic range in which UPCs at the LHC can probe gluons in protons and nuclei in quarkonium production, dijet and dihadron production. The Q-value for typical gluon virtuality in exclusive quarkonium photoproduction is shown for J/ψ and Υ as derived in [3]. The transverse momentum of the jet or leading pion sets the scale for dijet and $\pi\pi$ production respectively. For comparison, the kinematic ranges for J/ψ at RHIC, F_2^A and σ_L^A at eRHIC and Z^0 hadro-production at the LHC are also shown..

interact in the BDR with increasing energy. Photons contain more small dipoles than hadrons such as pions, leading to faster growth of $\sigma_{tot}(\gamma p)$ than given by the Froissart bound for hadrons [3]. Thus real photon interactions are sensitive to these small dipoles. As a result, a number of theoretical issues concerning the onset of the BDR can be studied using UPCs. The energy scale at which the dipole-target cross section in Eq. 1.32 is tamed by the unitarity constraint near the BDR and no longer undergoes rapid growth is poorly known, as is the energy dependence of the cross section. The energy at which the dipole cross section makes the transition from color transparency (no screening) to color opacity (strong screening) and ultimately the BDR, also needs to be determined. Answers may be found by selecting processes where gluons interact directly. At the LHC, high gluon densities can be achieved at lower energies using nuclei in UPCs: to reach the regime where Eq. 1.32 breaks down, measurements need to be extended to higher energies, smaller x, and to higher gluon densities, at the same energy and x, using nuclei. Nuclear beams were discussed for HERA but were not be implemented. Studies of small x physics at the LHC using hadronic pp or pA collisions will be rather difficult because, at central rapidities, the backgrounds due to multiple hard collisions will likely prevent measurements at virtualities less than $Q^2_{eff} \sim 100 - 200$ GeV^2. Thus, instead of using eA collisions to reach the small x regime, many of the approaches used at HERA can be implemented at the LHC using UPCs in both AA and pA collisions. A primary focus of UPC studies in AA and pA collisions is on hard interactions in the kinematics which probe high gluon densities in nucleons and nuclei. Hard scatterings on nuclear targets will extend the low x range of previous studies by nearly three orders of magnitude. In pA collisions, the HERA x range could be extended to an order

of magnitude smaller x. Thus all three HERA highlights: gluon density measurements, gluon-induced hard diffraction, and exclusive J/ψ and Υ production can be studied in ultraperipheral UPCs. Fig. 1.9 shows the x and Q^2 ranges covered by UPCs at the LHC. For comparison, the kinematic range of both Z^0 production in pp collisions at the LHC and the nuclear structure function at *eRHIC* are also shown, as computed by [3]. The x range of ep collisions at eRHIC is a factor of ~ 30 lower than at HERA for the same p_T .

For the purposes of this work we will now concentrate only to the features concerning the exclusive photoproduction of vector mesons.

1.4.2 Exclusive quarkonium production

Although calculations of the absolute cross section do involve significant higher-twist corrections, the strong increase in the J/ψ photoproduction cross section at HERA clearly indicates that heavy quarkonia are produced via coupling to small x gluon fields. Thus J/ψ and Υ photoproduction provide one of the cleanest tests of small $q\bar{q}$ dipole interactions with gluon fields. In the case of nuclear targets, several channels will be accessible: coherent processes, $\gamma A \to VA$, quasi-elastic processes, $\gamma A \to VA'$, and rapidity-gap processes such as large t light vector meson production, $\gamma A \to VX$. A highly nontrivial prediction of QCD is that, at sufficiently high energies, even small dipoles should be strongly absorbed by extended targets both due to leading-twist gluon shadowing and higher-twist multiple dipole rescattering. The A dependence of the coherent and quasi-elastic reactions, both change by $A^{-2/3}$ when going from weak absorption to the regime of strong absorption, as now it will be illustrated. The coherent dipole-scattering cross section is $\propto A^{4/3}$ in the weak absorption impulse approximation (a combination of A^2 from coherence at $t = 0$ and $A^{-2/3}$ from the integral over t) and $\propto A^{2/3}$ for strong absorption over the surface area of the target. Likewise, the quasi-elastic A dependence varies between A (weak absorption: volume emission) and $A^{1/3}$ (strong absorption: edge emission).

Dipole absorption is expected to reveal itself through strong suppression of coherent quarkonium production at $x_{eff} = m_V^2/s_{\gamma N} \leq 10^{-3}$ and at midrapidity for $x_{eff} \leq 5 \times 10^{-3}$. The AA measurements probe $x_{eff} = m_V/2E_N$ since $s_{\gamma N} = 2E_N m_V$ when $E_N \gg m_V, m_N$, correspondingto $x_{eff} = 2.5 \times 10^{-3}$ for Υ and 7.5×10^{-4} for J/ψ . Measurements at lower x_{eff} (higher effective energy) would require identifying which nucleus emitted the photon. An advantage of studying quasi-elastic reactions is the dissociation of the nucleus that absorbed the photon. As a result, the quasi-elastic x_{eff} range is a factor of 10 higher than coherent processes because the measurement is not restricted to midrapidity. Measurements of low p_T J/ψ production away from $y = 0$ appear to be easier for several of the detectors. At forward rapidity, the difference between the minimum x reached in breakup processes and coherent production is even larger.

The interaction of small color singlets with hadrons is one of the most actively studied issues in high-energy QCD. In exclusive electroproduction of mesons at high Q^2, as well as J/ψ and Υ photoproduction, the QCD factorization theorem separates the hard scattering amplitude into a product of the photon wave function, the vector meson wavefunction at zero transverse separation and the generalized parton densities, making evaluation of the vector meson production amplitude possible [44]. The leading-twist approximation (Fig. 1.10) differs strongly from predictions based on the Glauber model and two-gluon exchange models. The LT approximation accounts for the dominance of the space-time evolution of small quark–gluon wave packets in electroproduction, leading to the formation of a softer gluon field which effectively increases the dipole size with energy. In perturbative QCD, similar to QED, the total cross section for the interaction of small systems with hadrons is proportional to the area occupied by the color charge in the projectile hadron [50], predicting color transparency hard interactions with nuclei. Incoherent cross sections are expected to be proportional to the nuclear mass number, A, while

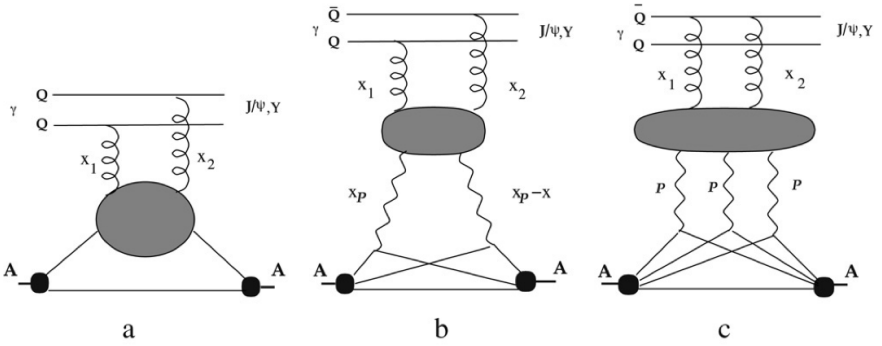

Figure 1.10 Leading-twist diagrams for quarkonium production from nuclear targets. .

the coherent amplitude is proportional to A times the nuclear form factor, F. The approximation of a quarkonium projectile as a colorless $Q\bar{Q}$ dipole can be formally derived from QCD within the limit $m_Q \to \infty$ and a fixed, finite momentum fraction, $x = 4m_Q^2/s$. In these kinematics, the quarkonium radius is sufficiently small to justify the applicability of pQCD. Such reactions are therefore an effective way of studying the properties of perturbative colorless interactions in the vacuum (the "perturbative Pomeron") at finite t. In this class of processes, the projectile wavefunction may be described as a superposition of different size configurations (qq, qqg, ...) leading to fluctuations in the interaction strength. Interactions of real and virtual photons with heavy nuclei can therefore provide unique information since the photon wavefunction contains both hadron-like configurations (vector meson dominance) and photon-like configurations (light $q\bar{q}$ components and heavy $Q\bar{Q}$ components). In high-energy photonuclear interactions, the BDR is manifested by inelastic diffraction of the photon into a multitude of hadronic final states while elastic diffraction, $\gamma \to \gamma$, is negligible. On the other hand, only elastic hadron diffraction survives in the BDR, hiding the detailed dynamics. Moreover, it is possible to post-select a small or large configuration of the photon wavefunction by choosing a particular final state. The LHC kinematics and detector acceptances greatly increase the energy range covered by HERA. Nuclear scattering provides a complementary method of studying this dynamics of small dipole propagation through the nuclear medium: nuclear targets represent in this way ideal probes of the spacetime evolution of small dipoles of size d which can be selected in high-energy γN scattering either by considering small x processes with $Q^2 \propto 1/d^2$, or by studying special diffractive processes such as quarkonium or dijet production. In the energy regime we are interested, the dipole cross section depends on the gluon distribution in the target and nuclear shadowing of the gluon distribution is expected to reduce it compared to a proton target. Moreover, theoretically at high energies one expects the transition of the regime described by the linear dynamics, where only the parton emissions are considered, to a new regime where the physical process of recombination of partons becomes important in the parton cascade and the evolution is given by a non-linear evolution equation (for recent reviews on the topic see Ref. [45]). This regime is characterized by the limitation on the maximum phase-space parton density that can be reached in the hadron wavefunction, the so-called parton saturation [46]. The transition is specified by a typical scale, the saturation scale Q_{sat}, which is energy dependent [49]. Parton saturation is expected to occur at low values of Bjorken x - *i.e.* when the gluon density inside protons and nuclei becomes large. It can be described by an effective theory derived from QCD: the color glass condensate (CGC) - see *e.g.* [47] for a recent review - which generalizes the BFKL evolution equation [48] to situations where the large density of gluons leads to nonlinear effects such as recombination. Understanding the spacetime evolution has consequences for other branches

of physics, including the early universe since the emergence of color-singlet clusters may play a role in the quark-hadron transition. This program makes it possible to study coherent (and some incoherent) photonuclear interactions at energies which exceed those at HERA by at least an order of magnitude: UPCs at the LHC reach both the large t and moderate W regime where the onset of the perturbative color transparency limit, $\sigma \propto A$, is expected as well as the onset of the BDR at large W where $\sigma \propto A^{1/3}$ [3].

1.4.3 The nuclear suppression factor

At this point a summary is necessary to group all the informations descending from difference approaches hereby presented in the evaluation of the exclusive photoproduction cross section of quarkonia state. For the purposes of this work it is better to concentrate uniquely on the J/ψ exclusive coherent photoproduction in $Pb-Pb$ collisions and introduce a physical quantity – as little as possible model dependent– that allows an immediate comparison among the presented data of the last chapter and the prediction derived starting from the discussed concepts of leading twist shadowing, perturbative QCD factorization and partons saturation. One strategy to achieve this goal is to analyse the ALICE result presented at the end, in terms of the nuclear suppression factor $S(W_{\gamma p})$[22]. $S(W_{\gamma p})$is defined through the ratio of the experimentally measured coherent photoproduction cross section at a given $W_{\gamma p}$to the cross section calculated in the impulse approximation (IA) which neglects all nuclear effects except for coherence:

$$S(W_{\gamma p}) \equiv \left[\frac{\sigma^{exp}_{\gamma Pb \to J/\psi\ Pb}(W_{\gamma p})}{\sigma^{IA}_{\gamma Pb \to J/\psi\ Pb}(W_{\gamma p})} \right]^{1/2}. \tag{1.33}$$

Such a definition of $S(W_{\gamma p})$ for coherent vector meson photoproduction on nuclear targets corresponds to the standard estimate of nuclear suppression in terms of A_{eff}/A [51]. Since the nucleus remains intact in the considered process, the transverse momentum distribution of J/ψ is dictated by the elastic nuclear form factor $F_A(t)$. The cross section in the impulse approximation is (see Par. 1.3.3):

$$\sigma^{IA}_{\gamma Pb \to J/\psi\ Pb}(W_{\gamma p}) = \left. \frac{d\sigma_{\gamma p \to J/\psi\ p}(W_{\gamma p})}{dt} \right|_{t=0} \Phi_A(t_{min}), \tag{1.34}$$

where $\Phi_A(t_{min}) = \int_{t_{min}}^{\infty} dt |F_A(t)|^2$. It is important to point out that the suppression factor $S(W_{\gamma p})$ is practically model independent since the estimate of the cross section in the impulse approximation is based on experimental data.

Using the fit of experimental data depicted in Fig. 1.5 to predict the value of the forward amplitude and integrating over the nuclear form factor, it is possible to predict the cross section in the impulse approximation at a given value of photon-nucleon energy $W_{\gamma p} = W^*_{\gamma p}$, namely $\sigma^{IA}_{\gamma Pb \to J/\psi\ Pb}(W^*_{\gamma p})$, so that, in comparison with collected data at the same energy, it is possible to extract a particular value of the nuclear suppression factor, $S(W^*_{\gamma p})$. This value, model-independent and computed starting from the experimental data, can be compared to its pure theoretical estimation, according to the different model available and previously introduced. The earliest approach to the calculation of the cross section of vector meson photoproduction on nuclei is based on the vector meson dominance (VMD) model, see the review in [52]. In this approach, a high energy photon converts into a vector meson at a long distance (time) before the target. Then, the vector meson interacts coherently with the nucleus by means of multiple interactions with the target nucleons. This process of hadron-nucleus interaction is usually described by the Glauber theory. In assumption that the multiple interactions dont distort the shape of the

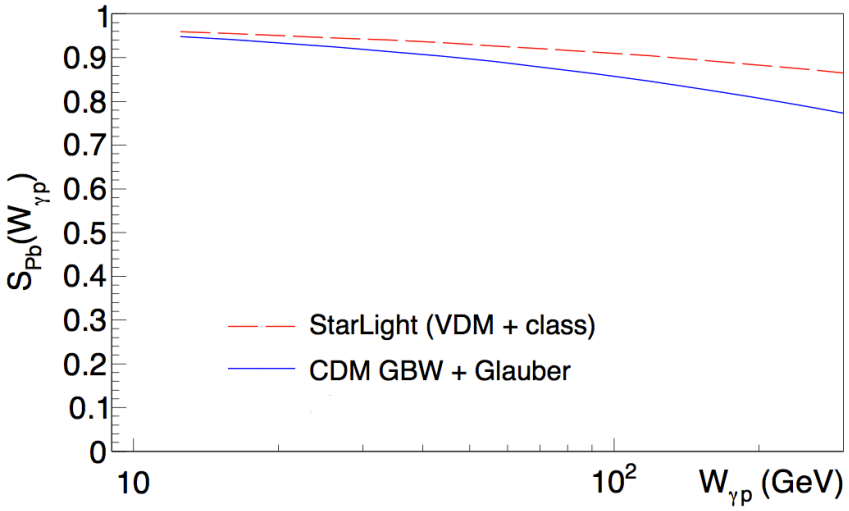

Figure 1.11 Nuclear suppression factor estimates in the Glauber model with the color dipole cross section and in the Starlight approach [22]. .

transverse momentum distribution of the vector meson but result only in the absorption effects the suppression factor for coherent vector meson production on the nucleus can be estimated as

$$S_A(W_{\gamma p}) = \frac{\sigma_{VA}(W_{\gamma p})}{A\sigma_{VN}(W_{\gamma p})}, \tag{1.35}$$

σ_{VN} is the total vector mesonnucleon cross section. The total vector mesonnucleus cross section σ_{VA} can be calculated in the optical limit of the Glauber theory:

$$\sigma_{VA}(W_{\gamma p}) = 2\int d^2b\left[1 - exp\left\{-\frac{\sigma_{VN}(W_{\gamma p})}{2}T_A(\mathbf{b})\right\}\right], \tag{1.36}$$

where $\mathbf{b}$ is the impact parameter, $T_A(\mathbf{b}) = \int \rho_A(\mathbf{b},z)dz$ and ρ_A is like in Eq. 1.26.

In the case of J/ψ photoproduction, the application of the VMD approach is problematic because the standard VMD model does not take into account that the spacetime picture of production of heavy quarkonium states that involves three stages: the production of "frozen small-size $q\bar{q}$ configurations, their interaction with the target, and the conversion of $q\bar{q}$ into the bound final-state. This spacetime picture can be modelled using the color dipole framework to calculate the cross section of the interaction of the $c\bar{c}$ configuration with the nucleon and the Glauber theory (eikonal model) to describe the propagation of the dipoles of the fixed transverse size through the nuclear medium [22]. Therefore, the nuclear suppression factor can be estimated using the phenomenological Golec-Biernat-Wusthoff dipole cross section [53]:

$$\sigma_{VN}(W_{\gamma p}) = \sigma_{c\bar{c}N}(W_{\gamma p}) = \sigma_0\left[1 - exp\left\{-0.25\langle d\rangle^2\left(\frac{x_0}{x}\right)^{2\lambda}\right\}\right], \tag{1.37}$$

where $\langle d\rangle \approx 0.25$ fm is the average size of the $c\bar{c}$ configuration in J/ψ; $\sigma_0 = 29.12$ mb, $\lambda = 0.277$ and $x_0 = 0.000041$ were obtained in [53] from the fit to the nucleon DIS data at small Q^2 and x. From the equation one can sees that this model assumes a gradual increase of the cross section with a decrease of x and, hence, an eventual onset of the saturation regime at very small x. Fig. 1.11 presents the nuclear suppression factor for lead, $S_{Pb}(W_{\gamma p})$, as a function of $W_{\gamma p}$. The result of the calculation using Eqs. 1.35 and 1.37 is shown by the blue solid line and will

be compared in the last Chapter with the experimental ALICE measurement. It is worth noting here that for the discussed kinematics, the results for the dipole-nucleon cross section obtained in different dipole models are rather close since they are constrained well by the DIS data for these energies. Note also that in the discussed model, the nuclear shadowing effect is driven by the $\sigma_{cc\bar{c}N}$ dipole cross section and, hence, shadowing is suppressed (a higher twist effect) for the dipoles of such a small size.

One can also estimate the nuclear suppression in the approach used in StarLight generator of ultraperipheral collisions [54]. In StarLight, the total cross section $\sigma_{J/\psi\,A}(W_{\gamma p})$ is calculated using the classical probabilistic formula[3]:

$$\sigma_{VA}(W_{\gamma p}) = \int d^2b \left[1 - exp\{-\sigma_{VN}(W_{\gamma p})T_A(\mathbf{b})\}\right], \tag{1.38}$$

while the values of $\sigma_{J/\psi\,N}(W_{\gamma p})$ are found from the HERA experimental data on $\gamma p \to J/\psi\, p$ cross sections [21] using the VMD model. As a result, the estimated value of σ_{VN} is rather small, which leads to the small nuclear suppression factor $S_A(W_{\gamma p})$. Indeed, the prediction for $S_{Pb}(W_{\gamma p})$ calculated using Eqs. 1.35 and 1.38 with the parameters from StarLight, which is shown by the red dashed line in Fig. 1.11, is constantly greater than the previous one.

It is of particular interest to have a comparison with the predictions of perturbative QCD, discussed in Par. 1.3.3. At high energies and small transverse momenta of J/ψ ($W_{\gamma p} \gg M_J/\psi \gg p_T$), in the leading order pQCD, the cross section of coherent J/ψ photoproduction on the proton is proportional to the proton gluon density $g_p(x,Q^2)$ squared [25, 44], as already shown in Eq. 1.22 that, it will be rewritten underlying the hard scale (Q^2) dependence:

$$\left.\frac{d\sigma_{\gamma p\to J/\psi\, p}}{dt}\right|_{t=0} = C(Q^2)[xg_p(x,Q^2)]^2, \tag{1.39}$$

where $x = M^2_{J/\psi}/W^2_{\gamma p}$ again. In the approximation that the Fermi motion of the quarks is neglected, the factor $C(Q^2) = M^3_{J/\psi}\,\Gamma_{ee}\pi^3\alpha_s^2(Q^2)/(48\alpha_{em}Q^8)$, where Γ_{ee} is the width of the J/ψ electronic decay. It is worth reminding that the accuracy of the LO pQCD calculations of the J/ψ photoproduction cross section is still a subject of discussions and the value of the hard scale Q^2 in the the gluon density is not fixed reliably [22]. Extending Eq. 1.39 for the description of J/ψ production on nuclei and accounting for the transverse momentum distribution dictated by the nuclear form factor, on has

$$\sigma^{pQCD}_{\gamma A\to J/\psi\, A}(W_{\gamma p}) = \left.\frac{d\sigma_{\gamma p\to J/\psi\, p}}{dt}\right|_{t=0}\left[\frac{g_A(x,Q^2)}{Ag_N(x,Q^2)}\right]\Phi_A(t_{min}) \tag{1.40}$$

In the impulse approximation (IA), $g_A(x,Q^2) = Ag_N(x,Q^2)$ and, hence, the nuclear suppression factor for coherent J/ψ photoproduction on nuclei is:

$$S_A(W_{\gamma p}) = \frac{g_A(x,Q^2)}{Ag_N(x,Q^2)} \equiv R^{IA}(x,Q^2). \tag{1.41}$$

Hence, in the leading order pQCD, the suppression of coherent J/ψ photoproduction on nucleus as compared to the impulse approximation results from the coherent nature of the small x screening of the gluon field of the nucleus which is generally accepted to be characterized by the $R^{IA}(x,Q^2)$ factor, that maps the proton gluon distribution into the nuclear one (compare also with Eq. 1.24). In the last chapter, the predicted trend of the nuclear suppression S_A will be depicted in term of R^{IA}, in comparison with the collected data.

[3]Note that the classical probabilistic formula and the Glauber formula give close values of the total σ_{VA} cross section only when $\sigma_{VN}T_A(\mathbf{b}) \ll 1$.

1.5 Lepton pairs production in two-photon processes

Since photons couple to all charged particles, two-photon processes involve a wide range of reactions as the production of free lepton pairs, bound-free pairs, multiple pairs, vector meson pairs, heavy quark pairs, etc. . The large ion charge leads to high two-photon rates. In this section the strong photon-ion coupling constant is discussed and how the non-perturbative QED effects arising from its strength is observed in lepton pair production, in particular e^+e^-, at the LHC[4]. While the role of higher order QED in electromagnetic heavy ion reactions is interesting in itself, it is also useful as a simpler model for investigating aspects of non-perturbative QCD. Though the primary heavy ion program involves the technically more challenging quantitative understanding of non-perturbative QCD, the more tractable theoretical treatment of higher-order QED should be experimentally verified. At present, both the experimental and theoretical state of the art of higher order QED is unsatisfactory in UPCs. Although some theoretical questions remain, more experimental data is greatly needed [3].

Leading-order calculations of charged-particle-induced lepton pair production date back to the works of Landau-Lifshitz and Racah [55]. The purpose was to test the newly born Dirac theory for the positron. Starting with the Dirac equation for the electron and its antiparticle, they found

$$\sigma = \frac{28}{27\pi}\sigma_0[l^3 - 2.198l^2 + 3.821l - 1.632], \tag{1.42}$$

where $\sigma_0 = (Z_1 Z_2 \alpha_{em} 2\hbar/m_c)^2$, $l = \ln(\gamma_{L,1}\gamma_{L,2})$, and $\gamma_{L,i}$ is the Lorentz factor of ion i in the laboratory system. The first term of this equation can be simply obtained from Eq. 1.1 and the cross sections for $\gamma\gamma$ pair production. The production cross sections for heavy lepton pairs ($\mu^+\mu^-$, or $\tau^+\tau^-$) can be obtained similarly. The production of $\mu^+\mu^-$pairs using hadron beams was first observed in 63 GeV pp collisions at CERN's Intersecting Storage Rings [56]. Because the cross sections depend on the inverse of the square of the particle mass, production of heavier pairs ($\mu^+\mu^-$, $\tau^+\tau^-$) is much smaller than for e^+e^-. Their Compton wavelength, $\lambda_i = \hbar/m_i c$, is smaller than the nuclear radius R. This requires the replacement $l \to L = \ln(\gamma_{L,1}\gamma_{L,2}\delta/m_i cR)$ in Eq. 1.42, where $\delta = 0.681\ldots$ is a number related to Eulers constant.

Due to experimental difficulties, Eq. 1.42 has never been fully tested. It remains disappointing that these 70-year-old QED calculations are still not fully tested. Although many aspects of QED have been tested to high precision, studies involving strong fields are much less advanced; pair production with relativistic heavy ions is therefore one important example. The 1937 Racah's formula for the total cross section is remarkably accurate when compared with more recent Monte Carlo calculations [58] of e^+e^-production. However, for the LHC lead beams, $Z\alpha_{em} \sim 0.6$ is not small. For heavy ions, the e^+e^-production probabilities are close to one, and lowest-order perturbative calculations of the cross sections violate unitarity (*i.e.* $d^2\sigma/d^2b > 1$) even at fairly large impact parameters ($b \sim \lambda_C = 386$fm[13]). Unitarity can be restored if higher order terms are included in the calculations. A general sum of the contribution of diagrams like those in Figs. 1.1e, f and unitarity corrections (involving the production of virtual e^+e^-pairs) was obtained in [60]. These observations led to more detailed calculations involving high order processes, such as the exchange of multiple photons (Coulomb distortion) and the production of multiple pairs (Figs. 1.1e, f). For example, to account for the Coulomb distortions one needs to add to Eq. 1.42 a term of the form:

$$\sigma_C = -\frac{28}{9\pi}[f(Z_1\alpha_{em}) + f(Z_2\alpha_{em})]\sigma_0 l^2 \tag{1.43}$$

[4] A complete treatise of two-photon processes can be found in [2, 3, 57].

where

$$f(x) = x^2 \sum_{n=1}^{\infty} \frac{1}{n(n^2+x^2)} \tag{1.44}$$

is the Bethe-Maximon correction. For $Pb-Pb$ collisions at LHC, the Coulomb distortion correction reduces the pair-production cross section by 14%. Other unitarity corrections further reduce the cross sections by 3% [60]. The importance of higher order effects is still under debate. Recent nonperturbative calculations have found that the e^+e^-cross section is identical to that obtained from lowest–order perturbation theory [57]. Non-perturbative effects should be present in the production of multiple pairs. These results were criticized in Ref. [61], which concluded that higher order terms contribute 25% of the e^+e^-cross section at RHIC. Measurements of single and multiple electron/positron pairs should help resolving these theoretical difficulties and serve as a probe of strongfield QED.

Luckily, in the recent times the interest in these processes has grown again, and one of the purposes of this thesis is to show a comparison among the ALICE collected data for the channel $\gamma\gamma \to e^+e^-$ and the available predictions at the leading order (StarLight Monte Carlo generator, [54]) or with the inclusion of high order effects, as did in [59].

1.6 Implications of photoproduction studies on the ALICE standard research program

In this chapter the importance of photoproduction and low-x studies for the physics pursued at the LHC, in particular in the ALICE research program, was extensively stressed. The concepts summarizing the informations hereby given rely on the ideas of nuclear gluon's distribution modifications, shadowing, saturation and distinction between non-perturbative and perturbative QCD as a function of the transfer momentum in the scattering processes. These concepts enter largely in the standard heavy ion program of ALICE for the study of the quark gluon plasma (QGP). Very briefly, thermodynamic considerations and QCD calculations suggest that strongly interacting matter can exist in different phases, depending on the temperature and the density of the system. A phase transition characterised by a specific critical temperature and baryochemical potential brings a system of deconfined quarks and gluons (QGP) into a state where partons are confined inside hadrons. Confinement is intimately related to the appearance of hadron masses, that are generated dynamically by strong interaction inside the hadrons. Despite the very accurate knowledge of the perturbative regime of QCD, the non-perturbative domain is still not fully understood and so are confinement and the generation of the hadron masses. Reducing the uncertainties on the initial structure and the in-medium effects of the colliding nuclei is extremely important also for the evolution of the system in $A-A$ collisions from cold nuclear matter to hot partonic matter. For all dynamical models of this evolution, knowledge of the initially produced particle density is crucial. Ultimately, however, this density varies with the uncertainty of the nPDFs and controlling these uncertainties is a decisive step in addressing one of the central issues in the dynamics of heavy-ion collisions.

It is worth noting that the perspective presented up to the present is only one of the several methodologies to better understand and disentangle the effects characterizing a collision among ultra-relativistic heavy ions. An other fundamental approach (in which the study of UPCs enter again as an important contributor) is the observation of $p-A$ collisions, in which one takes care only of the so called "cold nuclear matter effects", responsible of the initial state effects of a standard $A-A$ interaction. In a way, one can summarize what happens in this collision in term

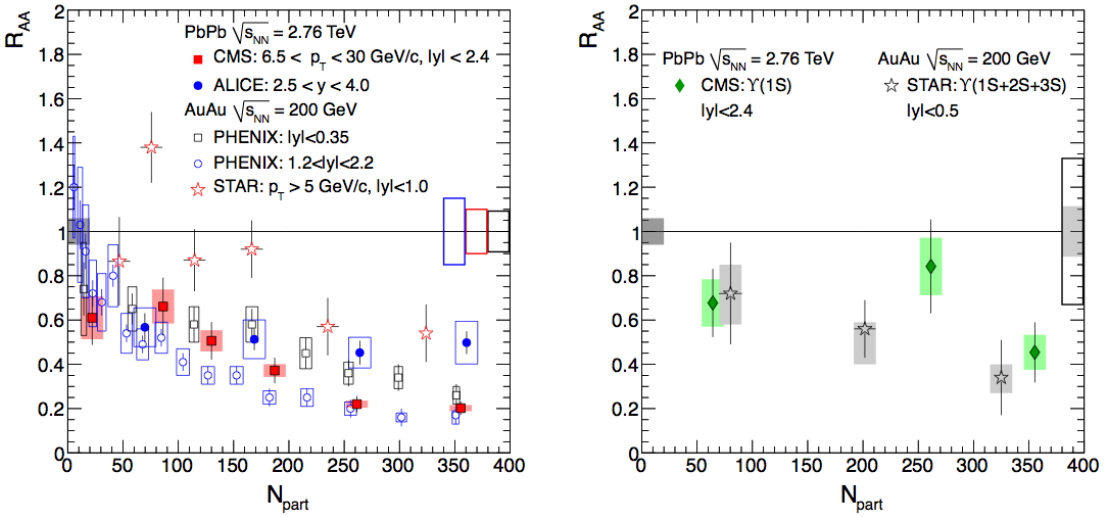

Figure 1.12 Measured nuclear modification factor as a function of produced multiplicity for J/ψ (left) and Υ (right).

of two contributors entering in a "conceptual" equation:

$$P_{A-A} = \sum_n I_n + \sum_n H_n, \tag{1.45}$$

where P_{A-A} is the observed phenomenology in the heavy ion collision, I_n is one of the initial state effects due to the partonic structure of the nucleus and H_n is the contribution of hot matter effects (in pQCD regime) that ALICE sets as its goal. Since these two terms strongly depend on the knowledge of nuclear PDFs, shadowing effects, etc., it is clear why the ALICE Collaboration enthusiastically pursued both a UPCs program in 2010 ($Pb+Pb \to \rho^0 + Pb + Pb$), 2011 ($Pb + Pb \to J/\psi + Pb + Pb$), 2013 ($p + Pb \to J/\psi + p + Pb$) and a $p-Pb$ one in 2013.

1.6.1 The nuclear modification factor

It is convenient to discuss with few examples how the uncertainties in the nPDFs affect the terms in Eq. 1.45. One of the observables that are sensitive to the interaction of hard partons with the deconfined hot matter is the nuclear modification factor R_{AA}. This quantity is defined as the ratio of particle production measured in nucleus-nucleus (AA) to that expected from the proton-proton (pp) spectrum scaled by the average number $\langle N_{coll} \rangle$ of binary nucleon-nucleon collisions occurring in the nucleus-nucleus interaction. Using the nuclear overlap function, which is defined as the convolution of the nuclear density profiles of the colliding ions in the Glauber model [62], the nuclear modification factor of the transverse momentum (p_{T}) distribution can be expressed as:

$$R_{AA}(p_{\mathrm{T}}) = \frac{1}{\langle T_{AA} \rangle} \frac{d^2N_{AA}/dp_{\mathrm{T}}d\eta}{d^2\sigma_{pp}/dp_{\mathrm{T}}d\eta} \tag{1.46}$$

where the AA spectrum corresponds to a given collision-centrality class and $\langle T_{AA} \rangle$ is the average nuclear overlap function for that centrality class and is proportional to $\langle N_{coll} \rangle$. This ratio is unity by construction if nucleus-nucleus collisions are just simple superpositions of nucleon-nucleon collisions. On the other hand, deviations of these ratios from unity, $R_{AA} < 1$, would imply contributions from nuclear or QGP effects, like in-medium energy loss.

Heavy quarkonia are important probes of the QGP since they are produced early in the collision and their survival is affected by the surrounding medium. The bound states of charm and

bottom quarks are predicted to be suppressed in heavy ion collisions in comparison with pp, primarily as a consequence of deconfinement ("melting") in the QGP [63]. The magnitude of the suppression for different quarkonium states should depend on their binding energy, with strongly bound states such as the Υ showing less or no modification. However, J/ψ production, the classical deconfinement signal, has puzzled expectations and interpretations ever since the first nuclear suppression was measured with Oxygen beams at the SPS, now attributed to cold nuclear matter effects rather than deconfinement. The "anomalous" suppression seen later with heavier beams turned out to be rather similar in magnitude at SPS and RHIC. This could indicate suppression of only the high mass charmonium states $\psi'$and χ_c, which populate about 40% of the observed J/ψ , and which should dissociate very close to or even below the critical transition temperature. Alternatively, it has been suggested that the increasing (with energy) J/ψ suppression is more or less balanced by enhanced production via recombination of two independently produced charm quarks [64]. A compilation of first LHC results on quarkonia production for both J/ψ (left) and Υ (right) is shown in Fig. 1.12 as a function of produced multiplicity (N_{part}), together with data from RHIC. While errors are still large, and the overall amount of suppression at LHC remains qualitatively similar to RHIC, the detailed pattern is quite different and intriguing. The p_{T}integrated R_{AA} of about 0.5, measured for the J/ψ at forward rapidity (closed circles), depends very little on centrality and is almost a factor of two larger than the one measured at RHIC in central collisions, also at forward rapidity (open circles); the difference is smaller but still significant when comparing with RHIC midrapidity data (open squares). On the contrary, the high p_{T}data at LHC (full squares) show a stronger suppression than the high p_{T}RHIC results (open stars). While such a pattern would be unexpected in a pure suppression scenario, it is qualitatively consistent with the recombination model, which predicts substantial regeneration effects only at low transverse momentum. The Υ suppression is very similar both at RHIC and LHC. As only about 50% of the observed $\Upsilon(1s)$ are directly produced, and the $\Upsilon(2s/3s)$ states seem to be more suppressed than the ground state, the measured R_{AA} is compatible at both RHIC and LHC with suppression of the high mass bottonium states only.

The ALICE results published in [65] concerning the measured J/ψ suppression at forward rapidity, illustrate clearly how important is the knowledge of the nPDFs for a better interpretation of the collected data. The observed suppression is larger than the one expected from cold nuclear matter effects, which include nuclear absorption and (anti-) shadowing. At LHC energies, J/ψ nuclear absorption is likely to be negligible and the modification of the gluon distribution function is dominated by shadowing effects. An estimate of shadowing effects is shown in Fig. 1.13. The shadowing is, respectively, calculated with the nDSg [37] and the EPS09 [35] parametrizations of the nuclear parton distribution function (nPDF). For nDSg (EPS09) the upper and lower limits correspond to the uncertainty in the factorization scale (uncertainty of the nPDF). The effect of shadowing shows no dependence with rapidity and its overall amount is reduced by the addition of a transverse momentum cut. At most, shadowing effects are expected to lower the R_{AA} from 1 to 0.7. Recent color glass condensate (CGC) calculations for LHC energies may take into account a larger initial state suppression (the $R_{AA} \approx 0.5$ previously discussed). However, any J/ψ suppression due to initial state effects, CGC or shadowing, will be stronger at lower pt contrary to the data behavior.

Similar issues on the effects of cold nuclear matter and shadowing have been recently faced also in [66], where the suppression of high transverse momentum D meson in central $Pb-Pb$ collisions is shown by the ALICE Collaboration.

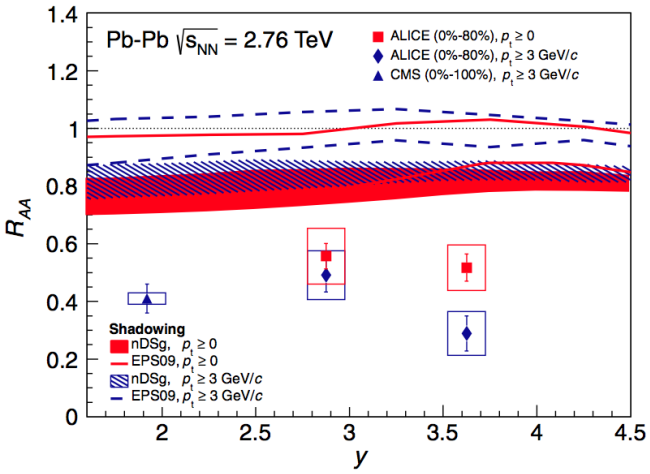

Figure 1.13 Centrality integrated inclusive J/ψ R_{AA}measured in $Pb-Pb$ collisions at $\sqrt{s_{NN}}$ =2.76 TeV as a function of rapidity for two p_{T}ranges. The two models [35, 37] predict the R_{AA}due only to shadowing effects for nDSg (shaded areas) and EPS09 (lines) nPDF, respectively..

Chapter 2

ALICE detector at the LHC

ALICE (A Large Ion Collider Experiment) has been designed and optimized to study the high particle-multiplicity environment of ultra-relativistic heavy-ion collisions. It has been collecting data during the first phase of the Large Hadron Collider operations, from start-up on November 2009 to the beginning of the first long technical shut-down in February 2013. During the first three years of operations LHC provided $p-p$ collisions at $\sqrt{s} = 0.9, 2.76, 7$ and 8 TeV, $Pb-Pb$ collisions at $\sqrt{s_{NN}} = 2.76$TeV and finally $p-Pb$ collisions at $\sqrt{s_{NN}} = 5.02TeV$. The first section of this chapter focuses on the LHC performance and includes details on the accelerator parameters that allow the LHC to perform as a lead ion collider. A detailed description of the ALICE sub-detectors involved in the analysis of ultra-peripheral collisions at mid-rapidity follows in the Sec. 2.2. The description of the Time-Of-Flight (TOF) system will be developed in the next chapter. The final part of this chapter is dedicated to the offline computing and reconstruction system based on the GRID framework.

2.1 The Large Hadron Collider

The Large Hadron Collider (LHC) [67], is a two-ring-superconducting hadron accelerator and collider installed in the 26.7 km tunnel that hosted the LEP machine and it completes the CERN accelerator complex together with the PS and SPS, among the others shown in Fig. 2.1. Four main experiments are located in four different interaction points along its circumference. ATLAS and CMS, the biggest ones, are multi-purpose detectors. LHCb is dedicated to the physics of the flavour, focusing on the study $CP-$violation using B meson decay channels. ALICE is dedicated to the physics of Quark Gluon Plasma through the observation of high energy heavy ion collisions, although physics programs in $p-p$ collisions have been carried out. The LHC was initially designed to provide $p-p$ collisions at the energy of $\sqrt{s} = 14$ TeV and $Pb-Pb$ collisions at $\sqrt{s_{NN}} = 5.5$ TeV. However, after the technical incident of 2008 [68] due to the quenching of a magnet, in 2010 and 2011 the LHC run at half of the design energy, thus providing $p-p$ collisions at $\sqrt{s} = 7$ TeV and $Pb-Pb$ collisions at $\sqrt{s_{NN}} = 2.76$ TeV. The excellent performance of the machine lead to the decision of increasing the centre-of-mass energy to $\sqrt{s} = 8$ TeV for $p-p$ collisions during the 2012 run [69].

Besides energy, the most important accelerator parameter is the instantaneous luminosity L, which is the proportionality factor between the event rate R and the interaction cross section of the process under study (σ_{int}):

$$R = L\sigma_{int} \tag{2.1}$$

The instantaneous luminosity depends only on the colliding beam parameters at the interaction

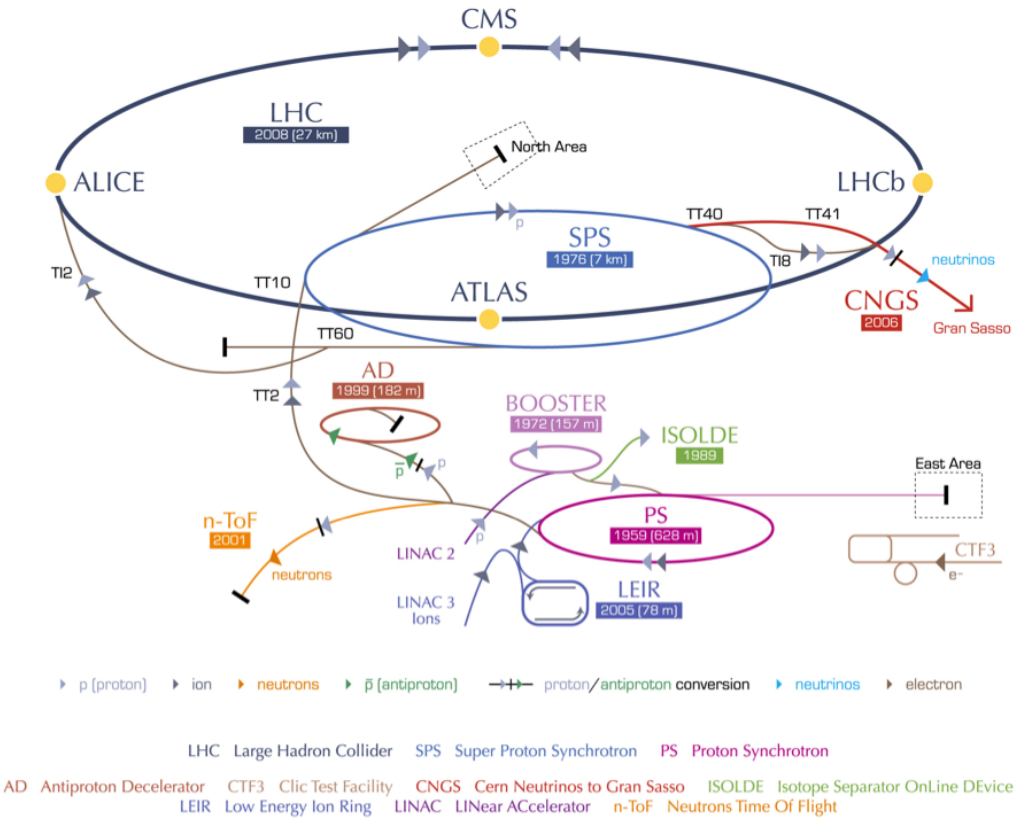

Figure 2.1 Schema of the CERN accelerator complex.

point and can be determined as

$$L = \frac{N_b^2 n_b f \gamma_L}{4\pi\varepsilon_n \beta^*} F \tag{2.2}$$

where N_b is the number of particles per bunch, n_b the number of bunches per beam, f the revolution frequency, γ_L the relativistic Lorentz factor, ε_n the normalized transverse beam emittance, β^* the amplitude function at the interaction point (IP), F the geometrical reduction factor that accounts for the crossing angle at the IP. It is worthy to remind that the transverse emittance and the amplitude function are related to the bunch cross-sectional size (σ_L) by the relation:

$$\sigma_L^2 = \frac{1}{\pi}\beta\varepsilon. \tag{2.3}$$

The transverse emittance tells how successful was the process of "packing" protons into bunches during the injector chain: a low emittance particle beam is such that the particles are confined to a small distance and have nearly the same momentum. This is important to keep the particle confined in their orbit all along the beam transport and accelerating chain that is optimised for a given design momentum. The β function is determined by the accelerator magnet configuration, more precisely by the quadrupole focusing strength. If the amplitude is small, the beam is squeezed. The value of the amplitude function at the interaction point, referred to as β^*, is the most significant. In order to achieve higher luminosity, it is important to keep the emittance low and β^* as small as possible, depending on the capability of the beam-focusing hardware near the interaction point. Moreover, in order to have β^* small at the interaction point, β is kept at larger values along the orbit. Since the emittance changes as a function of the beam momentum

during the acceleration, the normalised emittance, $\varepsilon_n = \gamma_L \beta \varepsilon$, which does not vary during the acceleration is most commonly considered, as in Eq. 2.2.

If it is assumed that the particles in each bunch are distributed in the three spatial directions according to Gaussian distributions with σ_{xy} and σ_z being respectively the size in the transverse plane and in the longitudinal direction (along the beam pipe), the F factor can be obtained from the total crossing angle at the IP, θ_c, as

$$F = \left[1 + \left(\frac{\theta_c \sigma_x}{2\sigma^*_{xy}}\right)^2\right]^{-1/2} . \tag{2.4}$$

The bunch transverse and longitudinal sizes are the same for both beams, as well as the number of particles per bunch. The latter is limited to be lower than $N_b = 1.15 \times 10^{11}$ because of the linear beam-beam tune, which measures the interaction that each particle undergoes when two bunches collide, and by the mechanical aperture of the LHC that also constrains the acceptable transverse emittance to $\varepsilon_n = 3.75$ μm for a $\beta = 180$ m in the LHC arcs. The number of bunches per beam instead has been varying according to the definition of different filling schemes during the machine operations. The beam parameters, ε and β^* in particular, have been optimized in order to tune the luminosity in the different interaction points, allowing all experiments to exploit their different capability. The two higher luminosity experiments, ATLAS and CMS run at a peak luminosity of the order of $L = 10^{33}$ cm^{-2}s^{-1} while LHCb run at the design luminosity value of $L = 10^{32}$ cm^{-2}s^{-1}. The maximum luminosity sustainable by ALICE in $p-p$ collisions is limited to the value $L = 10^{30}$cm^{-2}s^{-1} in order to avoid pile-up in the main tracker detector, being ALICE an experiment not optimised for data taking at high rate in $p-p$.

2.1.1 The injection chain

The LHC is supplied with protons from the pre-existing CERN accelerators, that have been partially upgraded to meet the requirements of the brand new machine for unprecedented high intensity proton bunches, small transverse and well defined longitudinal emittance, and finally bunch spacing of 25 ns. Several other conditions needed to be taken into account, such as the limit on the beam intensity that comes form the capacity of the cryogenic system to absorb the synchrotron radiation, the space-charge effect in the injectors, the requirement for the beam emittance to fit the aperture of the LHC superconducting magnets, among others. These considerations lead to a use of actual parameters as reported in Par. 2.1.3, different from those predicted in [67].

The proton source is a hydrogen tank from which the protons are extracted and injected in the Linear Accelerator 2 (Linac2), where they are accelerated up to 50 MeV. In the 4−rings Proton Synchrotron Booster (PSB) protons reach momentum of 1.4 GeV before being accelerated up to 25 GeV in the Proton Synchrotron (PS) accelerator, where a multiple splitting technique is used to generate the bunch trains. The four PSB rings accelerate one proton bunch per ring to a momentum of 1.4 GeV. A two-batch filling scheme allows to inject into the 8−slot PS three plus three (or alternatively four plus two) bunches from the PSB. Once in the PS the six bunches are split into three still at the injected energy of 1.4 GeV. Then the beam is accelerated up to 25 GeV before each bunch is split twice in two via 20 MHz and 40 MHz radio-frequency (RF) systems which have been installed during the LHC construction. A last RF system, playing at 80 MHz, splits the bunches into 4 ns long ones, to fit into the 200 MHz SPS buckets. After the debunching-rebunching procedure in the PS, the out-coming train contains 72 filled and 12 consecutive empty bunches for a total 84 buckets. The empty gap covers 320 ns, which also corresponds to the rise-time of the injection and extraction kickers. When the protons pass to

the Super Proton Synchrotron accelerator (SPS) they finally reach 450 GeV and then they are injected at the threshold energy into the LHC. After the injection of all bunches from the SPS to the LHC is completed, the energy ramp up procedure starts and accelerates the beams to the final energy. The LHC RF cavities operate at 40 MHz. In the ultimate LHC filling pattern, each of the available bunch slots is split in 10 buckets, each of them being 2.5 ns long. Only one out of 10 is filled with a bunch, thus leaving us with the minimum bunch separation of 25 ns. Considering the empty slots, the injection scheme explains why 2808 is the maximum number of bunches that can be arranged in the 3564 available 25 ns slots of the LHC. Most of the buckets end up not containing an actual bunch, however the nominally empty buckets can in fact contain small populations of particles, which are called satellite or ghost bunches, depending on the fact that they may be within the same 10-bucket slot as a nominal bunch or in slot supposed to be empty, respectively. As it is exposed in Par. 2.1.3, the satellite bunches have also been used to provide collisions to ALICE during the $p-p$ run, whenever luminosity needed to be kept under control and to lower values, avoiding dangerous pile-up in the detector.

2.1.2 The LHC as heavy ions accelerator

LHC was designed to perform as well as heavy ion collider. The particle source is a 3 cm lead cylinder, which is heated to about 500° C in order to vaporise a small number of atoms that, once partially ionised by a strong electric field, are accelerated in a linear device, in order to strip off the remaining electrons, until the ions become $^{208}Pb^{82+}$. Lead ions are then injected and accumulated in a Low Energy Ion Ring (LEIR) and then are sent to the PS, from which they follow the same injection chain as the protons. With the nominal magnetic field of 8.33 T in the dipole magnets, the ions can reach a beam energy of 2.76 TeV/nucleon, yielding to $\sqrt{s_{NN}}$ = 5.5 TeV. The nominal luminosity value is 1.0×10^{27} cm^{-2}s^{-1}, while for early operations a two-orders of magnitude lower value was foreseen.

2.1.3 LHC operations in symmetric collisions

2010, 2011 and 2012 $p-p$ runs

The total number of recorded collision events is most commonly expressed in terms of integrated luminosity (L_{int}) with units of inverse cross section and is reported as function of time for the different experiments and periods in Fig. 2.2

2010 and 2011 *PbPb* runs

The first collisions between stable beams of ^{208}Pb took place on the November 7^{th}, 2010, after a very short period of nearly 50 hours of commissioning [70]. The beam energy was 3.5 Z TeV, corresponding to a centre-of-mass energy of $\sqrt{s_{NN}} = 2.76$ TeV per nucleon pair. Despite this value represented half of the nominal centre-of-mass energy, still it was 13.8 times higher than the energy ever reached in heavy ion collisions. By the end of the run on December 6^{th}, 2010, an integrated luminosity of $L_{int} = 10\ \mu$b^{-1} had been delivered to ALICE, ATLAS and CMS, with a peak luminosity of $L = 3.0 \times 10^{25}$ cm^{-2}s^{-1}. In Tab. 2.1 the effective parameters (averaged over bunch-to-bunch and horizontal-vertical variations) recorded during the 2010 fill with the peak luminosity are reported [69]. A second $Pb-Pb$ run was performed in November 2011 at the same collision energy but with an increased peak luminosity. Fig. 2.3 summarizes the integrated luminosity in $Pb-Pb$ collisions as function of data-taking time for the three experiments in 2010 and 2011. The increase of the statistics by more than a factor 10 is clearly visible comparing the two periods.

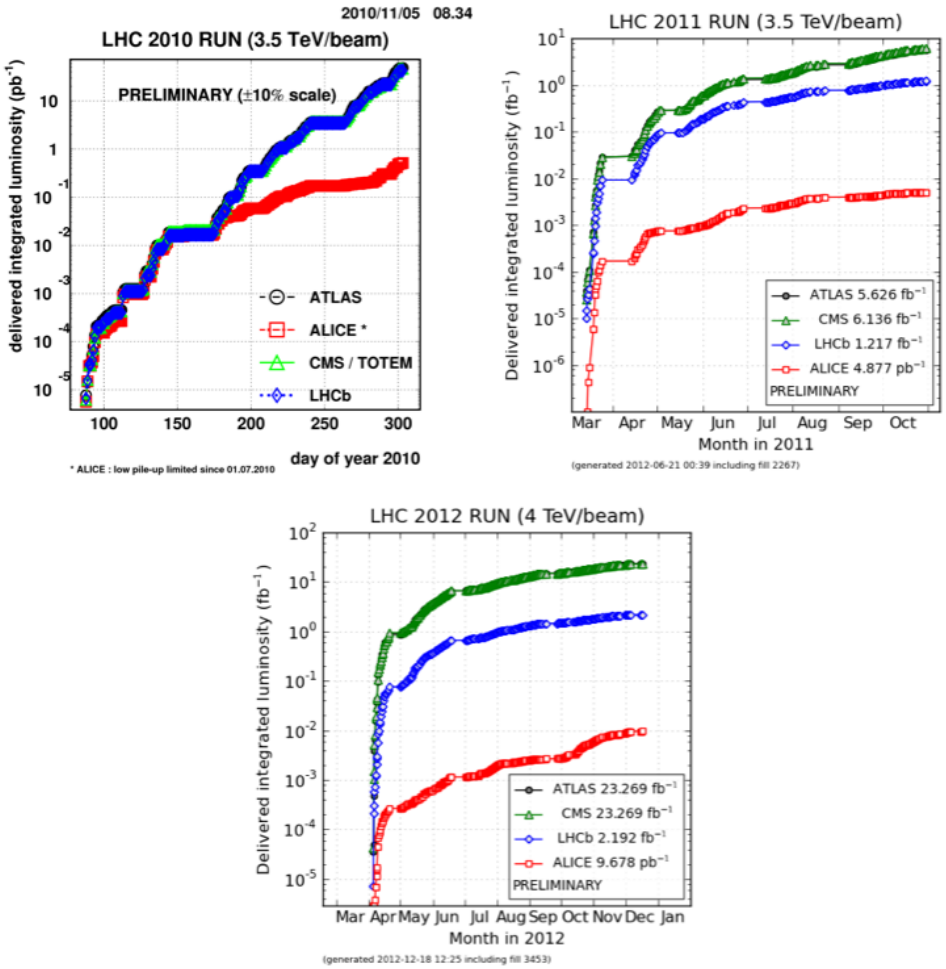

Figure 2.2 Total integrated luminosity recorded by the LHC experiments during 2010 (*top left*), 2011 (*top right*) and 2012 (*bottom center*) in $p-p$ collisions at $\sqrt{s} = 7$ TeV and $\sqrt{s} = 8$ TeV (in 2012 only).

2.2 ALICE: A Large Ion Collider Experiment

The main goal of ALICE experiment at the LHC [71] is the study of nuclear matter under extreme conditions of temperature and energy density as those reached in ultra-relativistic heavy ion collisions. The aim is to study the QCD predicted phase transition from the common hadronic matter to the so-called quark-gluon-plasma, in which quarks and gluons are free and not confined inside hadrons. Since ALICE is the only LHC experiment designed for $Pb-Pb$ collisions, it has to be able to measure as many observables as possible in the widest phase space region. ALICE is also interested in the study of $p-p$ interactions, that are a crucial reference for $Pb-Pb$ collisions. With respect to these experiments, ALICE is endowed by an excellent Particle IDentification (PID) performance, obtained combining different PID techniques from different detectors that are optimized in different momentum regions. In this section a brief description of the ALICE detector is given.

2.2.1 ALICE components

ALICE detectors can be classified in three groups:

Barrel detectors: they are hosted inside the external magnet previously used in the L3 ex-

Beam Energy	E = 1.38 A TeV =3.5 Z TeV
No. of bunches/ring	$k_b = 137$
Ions/bunch	$N_b = 11.2 \times 10^7$
Normalised emittance	$\varepsilon_n = 2\mu$m
Optical function	$\beta^* = 3.5$ m
Luminosity	$L = 3 \times 10^{25}$ cm^{-2}s^{-1}

Table 2.1 Effective parameters at peak luminosity in 2010 *PbPb* run (fill 1541).

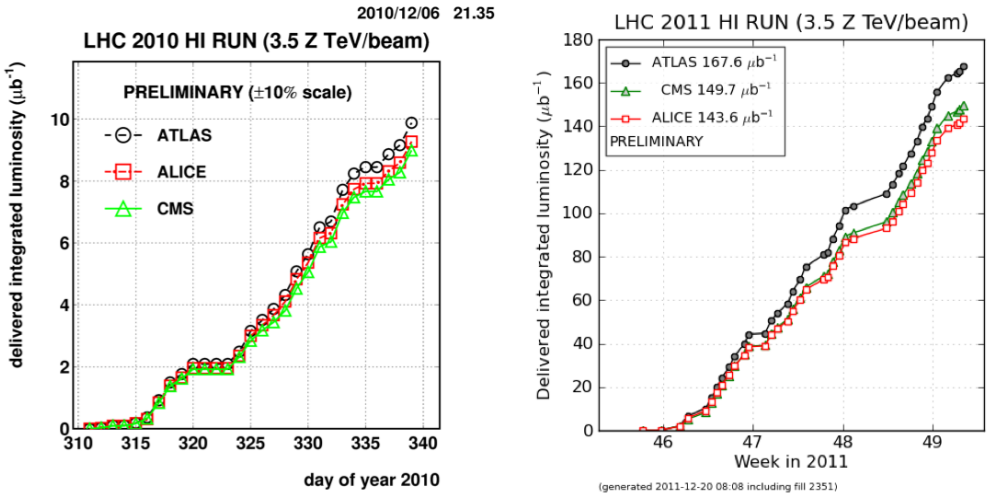

Figure 2.3 Total integrated luminosity recorded by the LHC experiments during 2010 (*left*) and 2011 (*right*) in $Pb-Pb$ collisions at $\sqrt{s_{NN}} = 2.76$ TeV.

periment at LEP, that covers a pseudorapidity interval $-0.9 \leq \eta \leq 0.9$ (corresponding to a polar acceptance $\pi/4 \leq \theta \leq 3\pi/4$). The azimuthal ϕ acceptance is 2π. They are mainly dedicated to the vertex reconstruction, tracking, particle identification and momentum measurement. Starting from the interaction point and going outward, we find the following detectors:

(i) Inner Tracking System (ITS);
(ii) Time Projector Chamber (TPC);
(iii) Transition Radiation Detector (TRD);
(iv) Time Of Flight (TOF)[1].

In the mid-rapidity region there are also two detectors with limited acceptance:

(i) High-Momentum Particle Identification Detector (HMPID);
(ii) PHOton Spectrometer (PHOS);
(iii) ElectroMagnetic CALorimeter (EMCAL).

Forward detectors: placed in the high pseudo-rapidity region (small angles with respect to the beam pipe) they are small and specialized detector systems used for triggering or to measure global event characteristics. They are:

[1]The description of the TOF system is skipped in this chapter since it will be be extensively treated in the next next one.

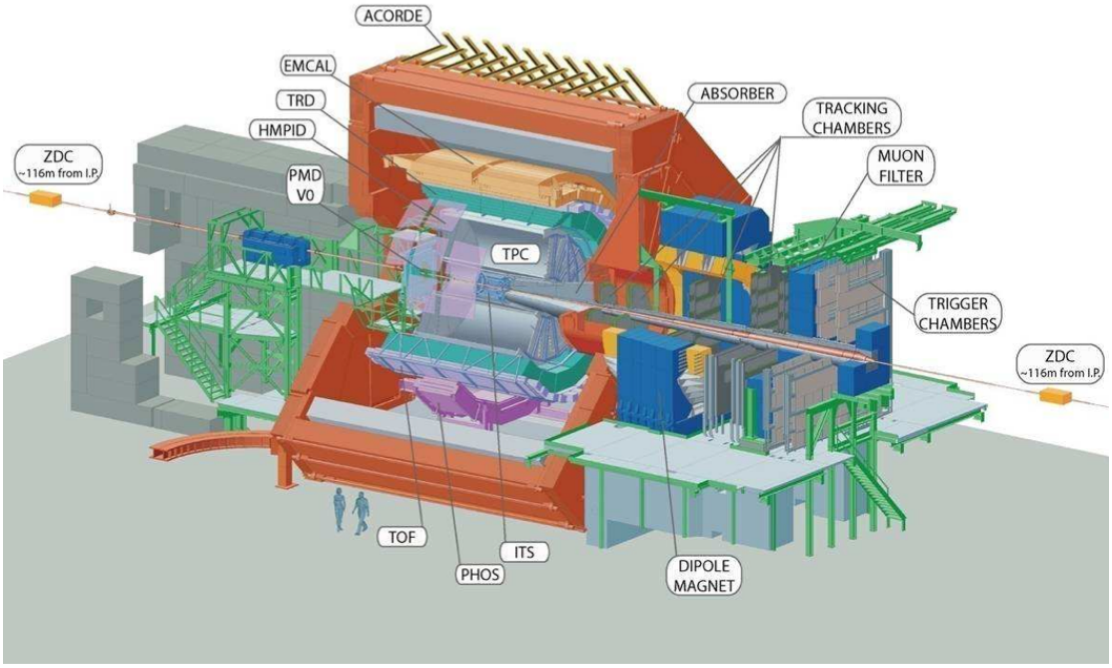

Figure 2.4 Sketch of the barrel detectors and of the muon spectrometer of the ALICE experiment. The central barrel is hosted inside the L3 solenoid magnet (red octogonal shape). From the IP outwards, we find the ITS, TPC, TRD and TOF detectors, together with the small acceptance detectors, (HMPID, PHOS) and EMCAL. On the right-hand side of the experiment, the muon spectrometer is composed of a dipole magnet, 14 planes of tracking and triggering chambers and absorber plates. In the ALICE conventions, the "A side" of the detector is the region opposite to the muon arm, that consequently is called "C side"

(i) Time Zero (T0) to measure the event time;

(ii) V0 detectors to reject the beam-gas background and to trigger minimum bias events. On the A side the V0 covers a pseudorapidity region of $2.8 < \eta < 5.1$, whereas on the C side it observes the interval $-3.7 < \eta < -1.7$;

(iii) Forward Multiplicity Detector (FMD) to provide multiplicity information over a large fraction of the solid angle ($-3.4 \leq \eta \leq -1.7$ and $1.7 \leq \eta \leq 5$);

(iv) Photon Multiplicity Detector (PMD) to measure the multiplicity and the spatial distribution of photons on an event-by-event basis in the $2.3 \leq \eta \leq 3.7$ region;

(v) Muon spectometer, to detect muons from heavy-quark vector mesons resonances in the region $-4.0 < \eta < -2.5$;

(vi) Zero Degree Calorimeter (ZDC), positioned along the beam pipe at 116 m from the interaction point to measure and trigger on the impact parameter of the collision.

Cosmic-rays detector: Used in combination with the trackers, an array of scintillators (ACORDE) is installed on top of the L3 magnet to trigger on cosmic rays.

In Figs. 2.4 and 2.5 a schematic view of the ALICE experiment is depicted, while in Fig. 2.6 a summary of the ALICE subsystem characteristics is reported. In the following paragraphs more details on the sub-detectors used in the two analysis of ultra-peripheral events both at forward and central rapidity.

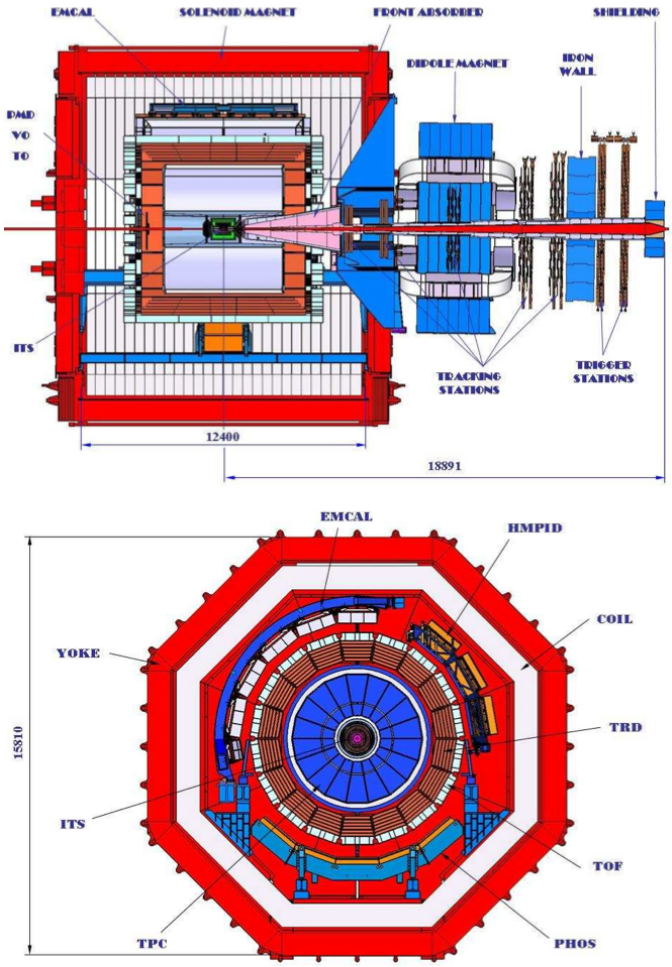

Figure 2.5 ALICE 2D cut views along the *yz* direction (*top*) and *xy* direction (*bottom*). The ALICE coordinate system is defined as follow: the *x* axis is perpendicular to the beam direction, pointing to the accelerator centre; the *y* axis is perpendicular to the *x* axis and to the beam direction; finally the *z* axis is parallel to the beam direction. The positive *z* axis is pointing in the direction opposite to the muon spectrometer.

The magnets

The ALICE experiment includes a solenoid magnet previously used in L3 experiment of LEP, and a dipole magnet situated next to the solenoid one, as a part of the forward muon spectrometer. The value of the uniform field provided by the solenoid magnet is variable up to 0.5 T which is a compromise between the momentum resolution, the acceptance al low p_{T}, and the efficiency in the track reconstruction. The dipole magnet is placed 7 m from the interaction vertex at 10 cm distance from the solenoid. The field produced by the dipole magnet is perpendicular to the beam direction with a nominal value of $B \sim 0.2$ T.

The Inner Tracking System

The Inner Tracking System (ITS) [71], as the closest tracking detector to the LHC beam pipe, is the main contributor for measuring the primary vertex of the collision. Its six concentric cylindrical layers are based on three different technologies of silicon detectors: pixels, drifts and

Detector	Acceptance (η, ϕ)	Position (m)	Dimension (m^2)	Channels
ITS layer 1,2 (SPD)	± 2, ± 1.4	0.039, 0.076	0.21	9.8 M
ITS layer 3,4 (SDD)	± 0.9, ± 0.9	0.150, 0.239	1.31	133 000
ITS layer 5,6 (SSD)	± 0.97, ± 0.97	0.380, 0.430	5.0	2.6 M
TPC	± 0.9 at r=2.8 m ± 1.5 at r=1.4 m	0.848, 2.466	readout 32.5 m^2 Vol. 90 m^3	557 568
TRD	± 0.84	2.90, 3.68	716	1.2 M
TOF	± 0.9	3.78	141	157 248
HMPID	± 0.6, $1.2^\circ < \phi < 58.8^\circ$	5.0	11	161 280
PHOS	± 0.12, $220^\circ < \phi < 320^\circ$	4.6	8.6	17 920
EMCal	± 0.7, $80^\circ < \phi < 187^\circ$	4.36	44	12 672
ACORDE	± 1.3, $-60^\circ < \phi < 60^\circ$	8.5	43	120
Muon Spectrometer				
Tracking station 1	$-2.5 < \eta < -4.0$	-5.36	4.7	1.08 M
Tracking station 2		-6.86	7.9	
Tracking station 3		-9.83	14.4	
Tracking station 4		-12.92	26.5	
Tracking station 5		-14.22	41.8	
Trigger station 1	$-2.5 < \eta < -4.0$	-16.12	64.6	21 000
Trigger station 2		-17.12	73.1	
ZDC:ZN	$\lvert\eta\rvert < 8.8$	± 116	2×0.0049	10
ZDC:ZP	$6.5 < \lvert\eta\rvert < 7.5$ $-9.7^\circ < \phi < 9.7^\circ$	± 116	2×0.027	10
ZDC:ZEM	$4.8 < \eta < 5.7$, $-16^\circ < \phi < 16^\circ$ and $164^\circ < \phi < 196^\circ$	7.25	2×0.0049	2
PMD	$2.3 < \eta < 3.7$	3.64	2.59	2 221 184
FMD disc 1	$3.62 < \eta < 5.03$	inner: 3.2		
FMD disc 2	$1.7 < \eta < 3.68$	inner: 0.834 outer: 0.752	0.266	51 200
FMD disc 3	$-3.4 < \eta < -1.7$	inner:-0.628 outer:-0752		
V0A	$2.8 < \eta < 5.1$	3.4	0.548	32
V0C	$-1.7 < \eta < -3.7$	-0.897	0.315	32
T0A	$4.61 < \eta < 4.92$	3.75	0.0038	12
T0C	$-3.28 < \eta < -2.97$	-0.727	0.0038	12

Figure 2.6 Summary of the ALICE detector subsystems. The acceptance in η is calculated from the nominal IP. The position is the approximate distance from the interaction point to the face of the detector, corresponding to the radius for the barrel detectors or to the position along the beam for the others. The dimension corresponds to the total area covered by the active detector elements. Channels refers to the total number of independent electronic readout channels. In case a detector is subdivided into sub-detectors, the numbers refer to the individual components.

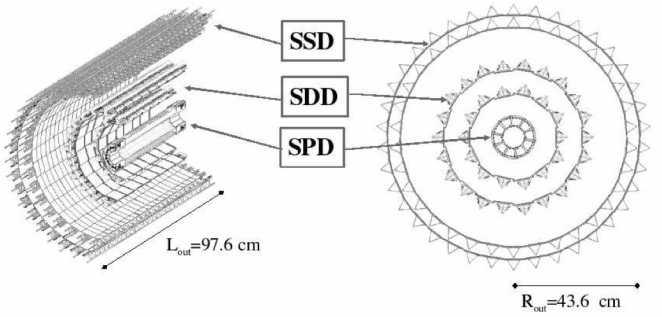

Figure 2.7 Layout of the ITS.

strips, as schematized in Fig. 2.7. The ITS is located at radius between 4 and 43 cm, surrounding the LHC beryllium beam pipe that is 800 μm thick and has a radius of 2.9 cm. The detector layout has been designed taking into account the high multiplicity environment foreseen for central $Pb-Pb$ collisions (a few thousands of particles per unit of rapidity were expected at the top energy), so that the occupancy is kept on the order of few percent.

The two innnermost ITS layers constitute the SPD, Silicon Pixel Detector. A total of 9.8×10^6 readout channels receive signals from the 20 half-staves of the SPD, each of them consisting of 240 modules with 1200 readout chips. Thanks to the high-granularity the SPD has also been used for the trigger system, especially for the minimum bias event selection. The SPD is mainly used to determinate the primary vertex position, with a resolution of the order of 100 μm.

The Silicon Drift Detector (SDD) is based on modules with a sensitive area of 70.17 $(r\phi) \times$ 75.26 (z) mm^2, divided into two drift regions where electrons move in opposite directions under a drift field of approximately 500 V/cm. The SDD modules are mounted on a linear structure called ladder. The SDD inner layer is made of 14 ladders with 6 modules each, the outer layer has 22 ladders, each of them with 8 modules. The position of the particle along z is reconstructed from the centroid of the collected charge along the anodes, while the position along the drift r coordinate is obtained from the measured drift time with respect to the trigger time. This reconstruction requires a precise knowledge of the drift speed, that is measured during frequent calibration runs, given its strong dependence from the humidity and temperature gradients in the SDD volume.

The Silicon Strip Detector (SSD) building block is a module composed of one double-sided strip detector connected to two hybrids hosting the front-end electronics. The sensors are 300 μm thick and with an active area of $73(r) \times 40(z)$ mm^2. Each sensor has 768 strips on each side, almost parallel to the z beam axis direction, with a pitch of 95 μm. The innermost SSD layer is composed of 34 ladders, each of them grouping 22 modules along the beam direction, while the other SSD layer is made of 38 ladders, each of them with 25 modules.

Since the four outer layers have analogue readout, they are used for particle identification via energy loss (dE/dx) measurement in the non-relativistic region for low momentum particles (down to p_{T}= 100 MeV). An example of the particle identification capabilities of the ITS is shown in Fig 2.8 for heavy-ion collisions: electrons can be identified from 80 MeV$/c$ up to 160 MeV$/c$ with a 2σ separation from π. Pions are separated from kaons up to 0.6 GeV$/c$ and kaons from protons up to 0.8 GeV$/c$.

A high resolution on the impact parameter is important to reconstruct secondary vertices from hyperons and heavy-flavour (B and D mesons) hadrons decay. The material budget in the active volume has been kept to a minimum, to avoid worsening of the impact parameter resolution due to multiple-scattering effects. Fig. 2.9 shows the transverse impact parameter

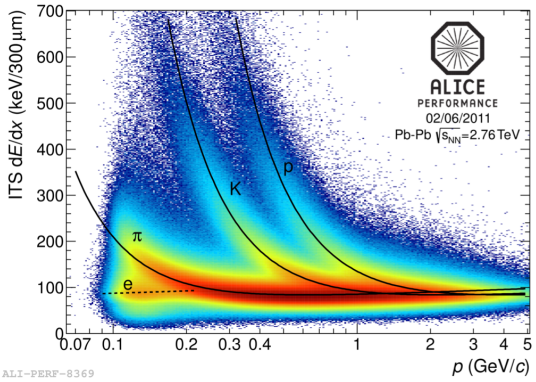

Figure 2.8 Energy loss distribution, dE/dx, of charged particles as function of their momentum, both measured by the ITS alone, in $Pb-Pb$ collisions at 2.76 TeV. The lines are a parametrization of the detector response based on the Bethe-Bloch formula.

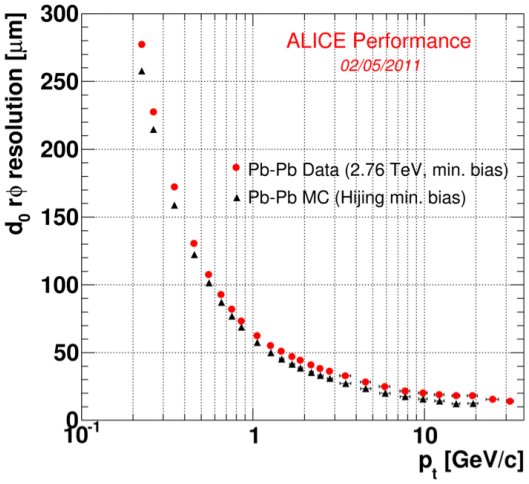

Figure 2.9 Transverse impact parameter resolution as function of the particle transverse momentum, obtained for well reconstructed tracks having two measured points in the SPD. The resulting impact parameter resolution is the convolution of the track-position and the primary-vertex resolutions. Data (*red dots*) come from 2010 $Pb-Pb$ dataset. Comparison with Monte Carlo simulation (*black triangles*) is also shown.

resolution as function of p_{T}, as measured in 2010 $Pb-Pb$ collisions. The resolution in the $r\phi$ plane is nearly 50 μm for 1 GeV$/c$ particles and decreases at higher momentum. A small improvement in the resolution is reached in $Pb-Pb$ collisions with respect to $p-p$, as the high multiplicity of central $Pb-Pb$ collisions implies a better primary vertex resolution.

The ITS can improve the momentum and angular resolution for tracks reconstructed by the TPC and allows to reconstruct tracks traversing dead TPC regions or very low momentum tracks that do not reach the TPC. ALICE exploits the ITS capability only with a dedicated tracking algorithm to recover very low momentum particles. The main difference with respect to the global tracking, is the starting point. The ITS StandAlone (ITS SA) tracking starts from the primary vertex and it reconstructs tracks, matching the clusters coming from the different ITS layers through selected angular windows.

The Time Projection Chamber

The Time Projection Chamber (TPC) [71], Fig. 2.10,is the main tracking detector of the central barrel, covering the pseudorapidity range $|\eta| < 0.9$ and the full azimuthal angle. The detector

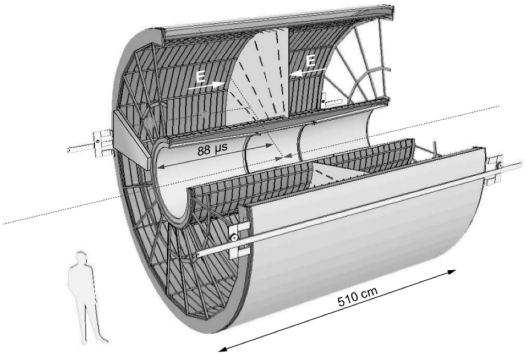

Figure 2.10 ALICE Time Projection Chamber (TPC).

design was optimized given the necessity to provide excellent tracking performance in a high multiplicity environment, to keep the material budget as low as possible in order to have low multiple scattering and secondary particle production, to limit the detector occupancy at the inner radius but still guarantee a good momentum resolution for high-p_{T}particles. The TPC is cylindrical in shape with an inner radius of 80 cm, determined by the maximum acceptable track density, and an outer radius of 250 cm, determined instead by the minimum track length for which the resolution on dE/dx is lower than 10%. The overall length along the beam direction is 500 cm. The TPC volume is filled with 90 m^3 of a mixture of $C_2H_2F_4(90\%)$, $i-C_4H_{10}(5\%)$ and $SF_6(5\%)$, optimized for drift velocity, low electron diffusion and low radiation length. A central cathodic plane divides the TPC in two drift regions. After ionization by a charged particle, the electrons drift toward the end-cap readout planes. The electron drift velocity of 2.7 cm/s over 250 cm (each of the two TPC drift region separated by the central cathode) gives a maximum drift time of 88 μs, therefore setting a limit on the event rate sustainability of the TPC. At high interaction rate the pile-up effect becomes relevant. Although tracks from pile-up events can be rejected using cuts on the primary vertex position and arrival time, this is one of the main factors that also forces ALICE to run at lower instantaneous luminosity with respect to the other LHC

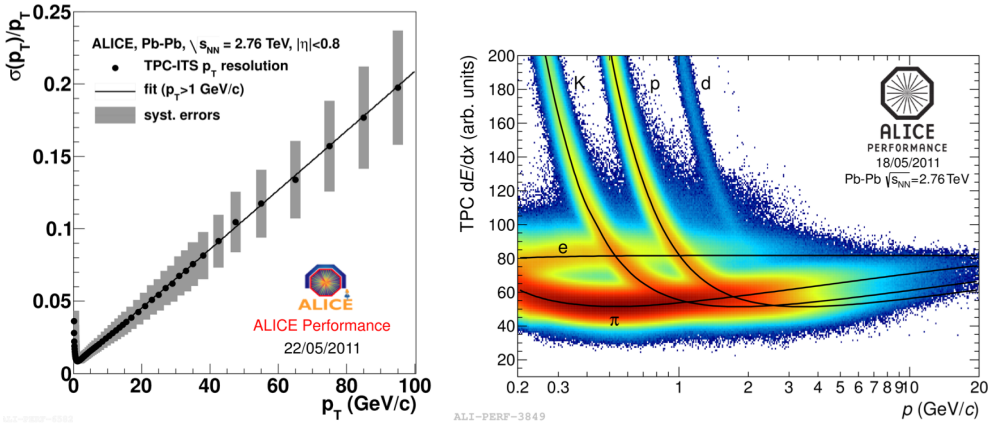

Figure 2.11 Relative transverse momentum resolution for TPC+ITS combined tracking (*left*) and TPC energy loss (*right*), in $Pb-Pb$ collisions at $\sqrt{s_{NN}}$ = 2.76 TeV.

experiments. Another limiting factor is the long TPC dead time, that slows down the readout frequency despite the fact that the slowest detector (in terms of readout electronics) is the SDD, with a busy time of 1 ms. The end-cap planes are divided in 18 sectors along the azimuthal angle and house the multiwire proportional readout chambers (with cathod-pad read-out). The radial thickness of the TPC is of 3.5% of the radiation lenght, at central rapidity and grows to 40% towards the acceptance edges.

The TPC is able to track particles in a wide momentum range, from about $p_{\mathrm{T}} \sim 0.1$ GeV$/c$ up to $p_{\mathrm{T}} \sim 100$ GeV$/c$ with good momentum resolution and efficiency $> 90\%$ for $p_{\mathrm{T}} > 100$ MeV$/c$, where the limiting factor are the interactions in the ITS material. Measuring the deflection in the magnetic field, the ITS and the TPC are able to determine the momentum of the charged particles with a resolution better than 1% at low $p_{\mathrm{T}}$and better than 20% for $p_{\mathrm{T}} \sim 100$ GeV$/c$, as reported in Fig. 2.11. The charge collected in the TPC readout pads is used to measure particle energy loss. The momentum measurement and the dE/dx information allow to separate the various charged particle species in the low momentum region: thanks to its good dE/dx resolution, the TPC can identify particles with $p_{\mathrm{T}} < 1$ GeV$/c$. An example of the TPC PID performance is shown always in Fig. 2.11, where the energy loss distribution for the different species is fitted by a Bethe-Bloch function, similarly to the ITS case.

The Time Of Flight

The Time Of Flight, a large area array for particle identification ($e, \pi, K, p, \ldots$) in the momentum range from 0.2 to 2.5 GeV$/c$, will be extensively presented in the next chapter.

The ElectroMagnetic CALorimeter

Opposite in the azimuth of PHOS, the ElectroMagnetic CALorimeter (EMCAL) [71] covers the the azimuthal range $80^\circ < \phi < 187^\circ$ and the pseudo-rapidity range $|\eta| < 0.7$. The *Pb*-scintillator sampling calorimeter has been designed to enhance ALICEs jet physics capabilities, measuring the neutral energy, together with the TPC, measuring the charged particles. With a lower granularity, but larger η acceptance than PHOS, it is optimized to study jet production rates and jet-quenching effects in heavy ion collisions. Furthermore, it is also able to measure γ, π^0, η, and $e^{\pm}$ particles.

V0s, ZDC

The V0 detector [71] is a small angle detector consisting of two arrays of scintillator counters, named V0A and V0C, installed on both sides of the ALICE detector at a distance of 340 cm from the IP on the side opposite to the muon spectrometer (V0A) and 90 cm from the IP (V0C) on the other side. Each array is segmented into 32 individual counters distributed in four rings and each connected with 1mm diameter Wave-Length-Shifting (WLS) fibre, that guide the light to an Hamamatsu photo-multiplier. The V0 provides the minimum bias trigger for the central barrel detectors in pp and PbPb collisions together with the SPD, the centrality triggers (implemented since 2011) and an early "wake-up" signal for the TRD, prior to the Level 0 (L0) trigger. V0 is also used to remove the collision background due to particles of the beam that interact with residual particles in the beam pipe, the so called "beam-gas" background. Starting from the measurement of the number of particles reaching the scintillators, which is directly proportional to the ADC counts and correlated with the number of primary particles, the V0 provides an estimation of the centrality of the collision [72]. In the last chapter it will be shown how

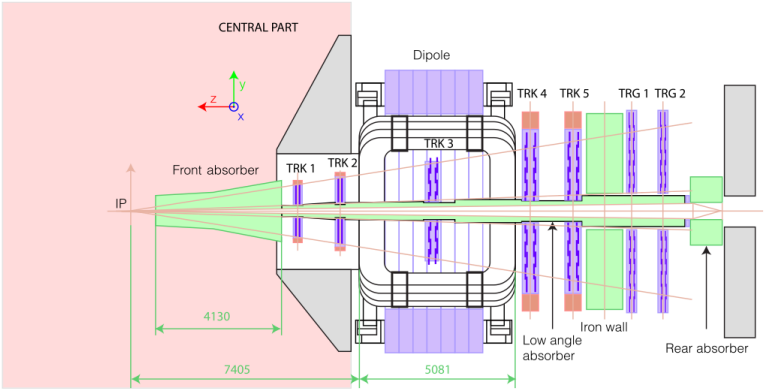

Figure 2.12 The ALICE muon spectrometer layout

this implies a specific requirement for the triggers dedicated to the selection of ultra-peripheral events, in which no hadronic interactions occur.

The centrality of the collision can be alternatively estimated by detecting the spectator nucleons that keep their trajectory in the forward direction along the beam pipe. For this purpose two Zero-Degree Calorimeters (ZDC) [71] are placed at 116 m on either side of the interaction point, very close to the beam pipe. The ZDC are also used to estimate the reaction plane in nucleus collisions and to reject parasitic collisions. The ALICE detector indeed, is placed close to the injection line from SPS to LHC. At the injection between SPS and LHC, some small fragments of the bunch of the beams can fall in the wrong radio frequency bucket. When these fragments collide with the main bunch of the second beam, they can produce parasitic collisions displaced about 30 cm from the centre of the experiment. Each ZDC is made of two calorimeters: one, for the spectator neutrons (ZN), is placed between the beam pipes; one, for the spectator protons (ZP), is located externally to the outgoing beam pipe where positive particles are deflected and separated by the neutrons by the magnets in the LHC beam pipe. Two small electromagnetic calorimeters (ZEM) are placed at about 7 m from the IP, on both sides of the LHC beam pipe, on the opposite side with respect to the muon spectrometer. The ZDCs are quartz-fibre sampling calorimeters, with passive element absorbers. The ZEM are used in particular to distinguish central from peripheral and ultra-peripheral collisions: in central collisions a small amount of energy is deposited in the ZDC, but similarly it could be the case for very or ultra-peripheral collisions, where spectator nucleons can bound into fragments which do not get out from the beam pipe and cannot be detected from the hadronic calorimeters. The ZEM allow to discriminate between events with different centrality by measuring the energy of the particles emitted at forward rapidity that increases with the collision centrality.

FMD

The FMD [71] provides charged-particle multiplicity information in the pseudorapidity range $-3.4 < \eta < -1.7$ and $1.7 < \eta < 5.0$, extending the pseudorapidity region where the SPD is able to provide multiplicity information. Charged particles are counted in rings of silicon strip detectors located at three different positions along the beam pipe. FMD3 and FMD2 are located on either side of the ITS detector (at about 75 cm from the IP) while FMD1 is placed at 320 cm from the IP on the opposite side with respect to the muon spectrometer.

Muon spectrometer

The main interest of the muon spectrometer [71] is the detection of muons in the pseudorapidity region $-4.0 < \eta < -2.5$. With this detector the complete spectrum of heavy-quark vector meson resonances (like J/ψ , ψ', Υ, Υ, ...) as well as the ϕ-meson can be measured in the $\mu^+\mu^-$decay channel. The simultaneous measurement of all the quarkonia species with the same apparatus allows a direct comparison of their production rate as a function of different parameters such as the collision centrality and the transverse momentum. In addition to vector mesons, the unlike-sign dimuon continuum up to masses around 10 GeV$/c^2$ can be measured. Since at the LHC energies the continuum is expected to be dominated by muons from the semi-leptonic decays of open charm and open beauty, this channel will allow to study the production of heavy flavours. This study is motivated by the QCD prediction of a reduction of the production of resonances with heavy quarks.

The spectrometer (Fig. 2.12) consists of the following components: a ten interaction length (λ_I) thick absorber filtering the muons absorbing hadrons and photons from the interaction vertex; a high granularity tracking system of 10 detection planes; a large dipole magnet; an inner beam shield to protect the chambers from primary and secondary particles produced at high rapidity. Besides, the muon spectrometer is provided with a cone shaped absorber made of carbon, covered by a thin layer of tungsten with a length of 3.5 m and placed at a distance of 0.9 mm from the collision point. Another absorber with a conical geometry and a length of 18.1 m and an angle of 2° made of a high Z material is present to screen the detector from particles produced in the interactions at high pseudorapidity. Moreover, a dipole magnet which produce a field of 3 T·m and a 1.2 m thick iron wall (7.2 λ_I) which absorbs secondary punch-through hadrons from the front absorber and low momentum muons from π and K weak decays, are part of the spectrometer too. The "active" detector consists of 4 plates which make up the muon triggering system to select muon candidates with a transverse momentum larger than a given programmable threshold (more details in the last chapter). They use resistive plate chambers (RPC) working in the streamer regime, whose aim is to select events with a $\mu^+\mu^-$pair at high p_{T}. In addition to the trigger chambers, the muon spectrometer has 10 tracking chambers characterized by a high granularity, and with a spatial resolution of 100 μm. Four chambers are placed in front of the dipole magnet, two inside and four afterwards.

2.3 ALICE On-line Systems

Five on-line systems support and allow the ALICE sub-detectors to record data from physics interaction and enable them to monitor and configure their hardware. In what follows they are briefly described as did in [73, 74].

2.3.1 Data Flow Systems

The different requirements per sub-detector, established in read-out time as well as data size, and also the different physics channels to be studied, account for ALICEs three-stage data-taking strategy, with the goal of managing with optimal data-taking rates in different physics processes in central heavy ion collisions. The general schema of the data flow can be seen in Fig. 2.13.

Event rates and the data volume produced in ALICE vary significantly between $p-p$ and heavy-ion collisions. The event size of the TPC as main contributor to the data volume (more than 80%) changes strongly depending on the charged particle multiplicity.

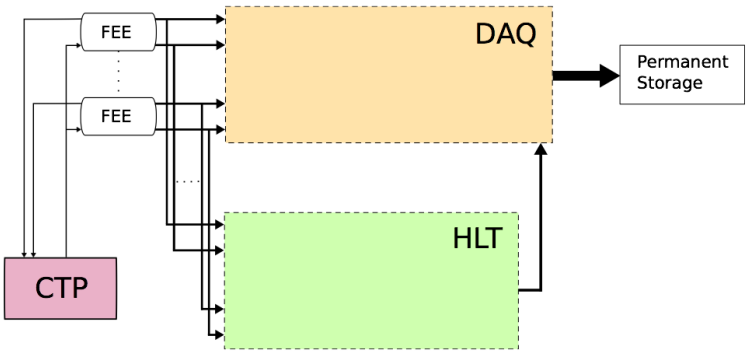

Figure 2.13 The Front-End Electronics (FEE) is triggered by the Central Trigger Processor (CTP) and sends the read out event fragments to the Data AcQuisition (DAQ), which immediately forwards a direct copy to the High-Level Trigger (HLT). Here a trigger decision is computed or data is compressed and sent to the DAQ, which then discards the event or starts the event building process. Finally, all accepted events are saved on permanent mass storage systems ready for offline reconstruction and data-analysis.

$p-p$ **collisions:** the data volume depends strongly on the luminosity due to event pile-up in the TPC. At a luminosity of $L = 3 \times 10^{30}$ cm^{-2}s^{-1} an interaction rate of 140 kHz is expected, which leads to a pile-up of about 25 events in the TPC and, therefore, to an average event size of about 2.5 MByte/event. The event rate is limited to 1kHz by the read-out rate of the SDD detector. The TPC itself is limited to a read-out rate of 3.5 kHz due to space charge considerations. At the beginning of the 2010 $p-p$ data taking at $\sqrt{s}$ = 7 TeV, the average event size was measured to be 890 kByte/event at an average read-out rate of 845 Hz [73]. The instantaneous peak luminosity was $L \approx 10^{29}$ cm^{-2}s^{-1} at an interaction rate of about 6 kHz [59]. In 2011, the instantaneous peak luminosity increased up to $L \approx 10^{30}$ cm^{-2}s^{-1}.

$Pb-Pb$ **collisions:** for central collisions and in the worst predicted case scenario of charged particle multiplicity $dN_{ch}/d\eta = 8000$, sizes of about 86 MByte/event have been expected for the barrel detectors. On average, minimum bias heavy-ion collisions are expected to have a charged particle multiplicity of 25% of central collisions. As the TPC event size scales almost linearly with the number of charged particles, ALICEs average minimum bias event size is anticipated to be about 22 MByte/event. At a maximum luminosity of $L = 10^{27}$ cm^{-2}s^{-1} for $Pb-Pb$ collisions an interaction rate of 8 kHz is expected. The actual read-out rate is reduced to about 300 Hz for central collisions which is limited by the TPC and 1 kHz for minimum bias events, limited by the read-out time of the TPC and other detectors.

In the first $Pb-Pb$ run in November 2010 a peak luminosity of $L \approx 2.5 \times 10^{25}$ cm^{-2}s^{-1} and an interaction rate of about 200 Hz was reached. The average minimum bias event size was measured to be 13.6 MByte/event at an average read-out rate of 115 Hz. In the second *PbPb* run in 2011 the peak luminosity increased up to $L \approx 4 \times 10^{26}$ cm^{-2}s^{-1} with an interaction rate of about 3.5 kHz [73].

These observations and assumptions lead to three extreme scenarios of read-out data volume:

- 1 kHz minimum bias $p-p$ collisions with about 2.1 GByte/s;
- 1 kHz minimum bias $Pb-Pb$ collisions with about 22 GByte/s;
- 300 Hz central $Pb-Pb$ collisions with about 26 GByte/s.

ALICEs maximum sustained bandwidth to the permanent storage is 1.25 GByte/s, which is estimated to be sufficient to provide the necessary statistics for the various physics channels and, at the same time, is a compromise on cost and performance for the mass storage systems. This emphasizes the importance of data reduction by the High-Level Trigger (HLT) to fulfil these requirements.

Trigger System

The Central Trigger Processor (CTP) [74] collects trigger inputs from the fast trigger detectors, computes a decision, and sends the readout signal to all ALICE detectors. An anticipated interaction rate of 8 kHz ($L \sim 10^{27}$ cm^{-2}s^{-1}) in heavy-ion collisions and a large span of detector read-out times lead to a three-level design, where the Level 0 (L0) signal reaches the detectors after 1.2 μ. The Level 1 (L1) allows more time for more advanced trigger inputs after 6.5 μs.

Pile-up of central heavy-ion collisions in the TPC cannot be easily reconstructed due to the very high particle multiplicity. This can be taken into account by the past-future protection at the final trigger stage, the Level 2 (L2). After the drift time of the TPC of 88 μs the L2 *accept* (L2a) or L2 *reject* (L2r) signals are sent to the detectors.

2.3.2 Data Acquisition System

On the L2a signal, the detector readout starts and the detector Front-End-Electronics (FEE) sends the detector data via 460 optical fibres to the Data AcQuisition (DAQ) using a standardized ALICE protocol, the Detector Data Link (DDL) [74]. The DAQ is structured in three layers, according to data locality. In the first level, the read out detector data is received by Peripheral Component Interconnect-Extended (PCI-X) cards, the DAQ Read-Out Receiver Cards (D-RORCs), inserted in commodity PCs called Local Data Concentrators (LDCs).

The LDCs build sub-event fragments and send them to the second level, the global event building, which is implemented as an event-building network of commodity PCs, the Global Data Concentrators (GDCs). In the final stage, the complete events are transferred via a fibre-channel storage network to permanent storage, for later offline reconstruction and analysis of the events.

In parallel, an exact copy of the incoming detector data in the D-RORC is sent via a second DDL on the same D-RORC to the HLT, which computes an even more sophisticated trigger decision and sends the decision and additional data to extra assigned LDCs. If an event gets rejected by the HLT, it is already discarded on the LDC level to spare the event building step. Three different run modes of the DAQ can be distinguished, determined by the activity of the HLT.

- *Mode A:* DAQ only - HLT disabled.
  No data is sent to the HLT and no HLT decision is expected by the DAQ.

- *Mode B:* DAQ + HLT analysis.
  Data is sent to the HLT, which processes the data, and computes a decision. However, the DAQ only checks for data integrity but does not consider the HLT decision.

- *Mode C:*DAQ + HLT enabled.
  Data is sent to the HLT, which processes the data, computes a decision, and the DAQ executes the decision.

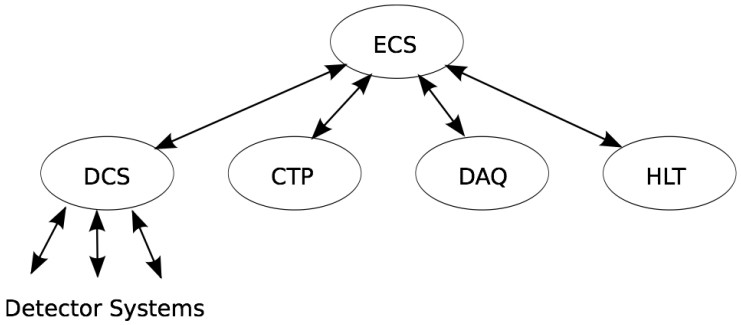

Figure 2.14 The Experiment Control System (ECS) is the top level entity steering the ALICE data-taking process. It controls and configures CTP, DAQ, and HLT directly and the detector systems indirectly via the Detector Control System (DCS).

2.3.3 High-Level Trigger System

The High-Level Trigger (HLT) [74] is a large high performance computing farm based on commodity PCs, situated in parallel to the DAQ in the data flow. It performs full reconstruction of the detector data online and allows for complex trigger and compression algorithms based on the full event information obtained from the reconstruction. Three main tasks of the HLT can be highlighted.

Filtering: acceptance or rejection of events on the basis of the on-line reconstruction and analysis.

Selection: selection of a physics Region-Of-Interest (ROI) within one event, storing only part of the readout detector data.

Compression: reduction of the event size with lossless and lossy[2] compression algorithms, applied on detector and reconstructed data.

2.3.4 High-Level Trigger System

Two control systems watch over the ALICE sub-detectors and the other online systems as indicated in Fig. 2.14.

Detector Control System The Detector Control System (DCS) [74] is responsible for the configuration and monitoring of the different detectors. Several parameters like temperature, pressure, and voltage of the detectors' subsystems are monitored and archived for the use in the online and offline event reconstruction. Furthermore, the DCS handles ALICEs communication with the LHC.

Experiment Control System On top of all the detectors and online systems sits the Experiment Control System (ECS) [74] and naturally implements interfaces to all of them. This top control layer steers the data-taking and all other systems. It allows the operators in the ALICE Control Room (ACR) to configure the whole experiment via the ALICE Configuration Tool (ACT) and, therefore, to start and stop the data-taking process. The CTP,

[2]In information technology, "lossy" compression is a data encoding method that compresses data by discarding (losing) some of it. The procedure aims to minimize the amount of data that needs to be held, handled, and/or transmitted by a computer.

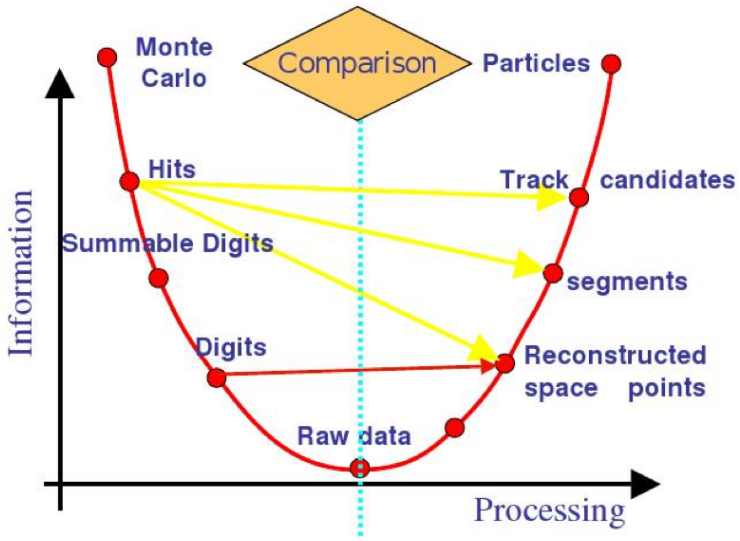

Figure 2.15 Data processing framework.

DAQ, HLT, and DCS are directly configured and controlled from the ECS, where the detectors are managed indirectly via the DCS.

2.4 ALICE offline computing: the AliRoot framework

The ALICE offline framework, AliRoot [75], is an object-oriented software framework, based on the ROOT system [76], entirely written in C++, with some external programs (hidden to the users) still in FORTRAN. It offers integrated I/O with class schema evolution, an efficient hierarchical object store with a complete set of object containers, a C++ interpreter allowing one to use C++ as scripting language. The data processing framework is shown schematically depicted in Fig. 2.15. In this way it is possible to allow simulation, reconstruction and data analysis both from collisions ($p-p$, $Pb-Pb$, $p-Pb$) and cosmic events within the same framework [79]. Given the unprecedented amount of data collected at the LHC and the computational cost of data processing, the worldwide Grid distributed computing system [78] is the ideal stage to host this unprecedented effort. The ALICE Collaboration has developed the AliEn (ALICE Environment) framework [77] to reconstruct and analyze the data in a distributed environment. AliEn provides a global file system, or catalogue, for data storage and an interface to execute the jobs on the Grid. A distributed system, such as the Grid, allows to split the jobs analysis into many identical subjobs that run in parallel on different computer nodes. Users can implement custom analysis code or run the AliRoot analysis tools on the available datasets by specifying the version of the AliRoot or ROOT packages deployed on the Grid. The AliEn interface can be used to distribute and to monitor the progress of the jobs. The ALICE Virtual Organization (VO) is composed of more than 80 sites distributed all over the world. The software programs run on Worker Nodes (WN) machines, while the Storage Elements (SE) are responsible for managing physical files in the site and providing an interface to the mass storage. The Computing Element (CE) service is an interface to the local WN batch system that manages the computing resources of the site [69]. In this last part of the chapter, the main features of the framework are mentioned.

2.4.1 Event simulation

The whole simulation process, represented by the left part of the parabolic path in Fig. 2.15, includes the following steps:

Event generation of final-state particles. An event generator produces a set of particles with their momenta, origin point and identity. This set of particles, where one maintains the production history (in form of mother-daughter relationship and production vertex), forms the kinematic tree. The collision within the AliRoot framework is simulated by a physics generator code like PYTHIA [80], HIJING [81] or a parameterisation (with the class *AliGenParam*) of the kinematical variables. Final state particles are fed to the transport program. Nevertheless, there is also the possibility to use external kinematic generators, not belonging to the AliRoot framework. This is exactly the case of the analysis presented in this thesis: to simulate photoproduction of vector mesons and lepton pairs, the StarLight generator [54]) was adopted (see Sec. 1.4.3). In StarLight, the event is simulated following the kinematics discussed in the previous chapter, and the final state - *e.g.,* $l^{\pm}(\pi^{\pm})$ from J/ψ (ρ^0) decays - constitutes the input to fed the standard AliRoot's kinematic tree. From this step on, the simulation proceeds as discussed below.

Particle transport. Particles emerging from the interaction of the beam particles are transported through the detector material, simulating their interaction with it, and the energy deposition that generates the detector response (*hits*). Hits contain also information (track labels) about the particles that have generated them. The main models used to transport generated particles through the detector are GEANT [82] and FLUKA [83].

Signal generation and detector response. During this phase the detector response is generated from the energy deposition of the particles traversing it. This is the ideal detector response, before the conversion to digital signal and the formatting of the front-end electronics is applied. The detector response is proportional to the particle energy loss. There is one main exception, namely the calorimeter (PHOS and EMCAL) hits, where a hit is the energy deposition in the whole detecting element volume. This happens because inside these detectors the particle is completely stopped.

Digitisation. The detector response is digitised and formatted according to the output of the front-end electronics and the data acquisition system. The results should resemble closely the real data that is produced by the detector. Furthermore in some detectors digits are used for comparison with a given threshold, for example in TOF and ITS pixel layers. These are in fact "digital" detector in the sense that they are requested only for an on-off response, depending on the threshold overcoming. There are two types of digits: *summable digits*, where low thresholds are used, in order to preserve the possibility to add signals from other particles (event merging), and *digits*, where real thresholds are used, and the result is similar to what one would get in the real data taking. In some sense the summable digits are precursors of the digits. The noise simulation is activated when digits are produced. There are two differences between the digits and the *raw data* format produced by the detector: firstly, the information about the Monte Carlo particle generating the digit is kept, and secondly, the raw data are stored in binary format (like the detector data) while the digits are stored in ROOT classes. Two conversion chains are provided in AliRoot: $hits \rightarrow summable\ digits \rightarrow digits$, and $hits \rightarrow digits$.

Summable digits are used for the so called "event merging", where a signal event is embedded in a signal-free underlying event. This technique is widely used in heavy-ion

physics and allows to reuse the underlying events with substantial economy of computing resources. Optionally it is possible to perform the conversion $digits \rightarrow raw\ data$, which is used to estimate the expected data size, to evaluate the high level trigger algorithms, and to carry on the so called computing data challenges. The *AliSimulation* class provides a simple user interface to the simulation framework.

2.4.2 Reconstruction

Most of the ALICE detectors are tracking detectors. Each charged particle going through them leaves a number of discrete signals that measure the position of the points in space where it has passed. The task of the reconstruction algorithms is to assign these space points to tracks and to reconstruct their kinematics. This operation is called track finding. In ALICE it is required a good track-finding efficiency for tracks down to p_{T}= 100 MeV$/c$ even at the highest track density. Given this situation, most of the development is done for $Pb-Pb$ central events, since lower multiplicities are considered an easier problem once the high-multiplicity ones can be handled. However, the opposite may be true for some quantities, such as the main vertex position, where a high track multiplicity will help to reduce the statistical error. Track reconstruction is represented by the right part of the parabolic path in Fig. 2.15. The reconstruction steps are:

Raw data. This is a digitised signal (ADC count) obtained by a sensitive pad of a detector at a certain time.

Rec Points. Reconstructed space points: this is the measurement of the position where a particle crossed the sensitive element of a detector (often, this is done by calculating the centre of gravity of the "cluster", which is a group of contiguous cells with signals above applied threshold).

Tracks. Reconstructed tracks: this is a set of five parameters (the curvature, two angles with respect to the coordinate axes, two positions) of the trajectory of particles together with the corresponding covariance matrix estimated at a given point in space and the information of the detector in which reconstruction occurred.

This procedure is used for both real and simulated data.

Due to the unknown multiplicity in $Pb-Pb$ collisions at the LHC energies at its design time, ALICE tracking was foreseen to be able to deal with a multiplicity up to 8000 particles per unit of rapidity and an occupancy in the TPC inner part that can reach 40% [84]. The track finding procedure developed for the central barrel (ITS, TPC, TRD, TOF) is based on the Kalman filter algorithm, widely used in high-energy physics experiments. The Kalman filter method allows to have track finding at fitting simultaneously, its main property is the possibility to extract the optimal estimate of the track geometrical parameters point by point, since it is a local based method. For this reason it is very useful also to extrapolate the track from a detector to another. In the Kalman Filter algorithm energy loss and multiple scattering are accounted for in a direct and simple way. The ALICE track reconstruction [85] is based on the following steps [86]:

- Primary vertex determination using only SPD informations, for a fast interaction point position estimate.

- Track reconstruction in the TPC. Track finding in the TPC from the outer to the inner part. The outermost pad rows and the primary vertex position from previous step are used as seed.

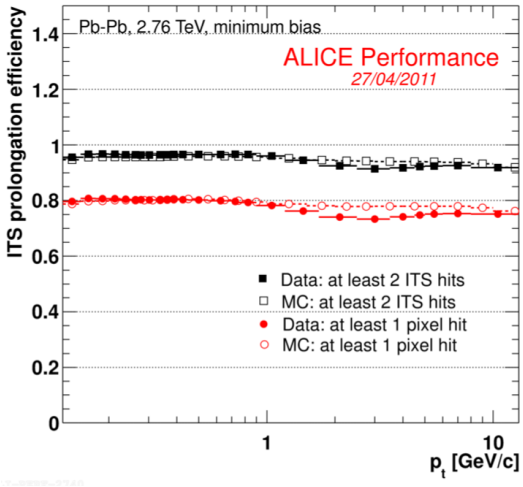

Figure 2.16 TPC-to-ITS prolongation efficiency in $Pb-Pb$ collisions (*full markers*) compared with Monte Carlo simulation (*empty markers*). Black points correspond to the efficiency in the case that two points are in the full ITS, red points to the case where one hit in the pixels detector is required.

- Track reconstruction in the ITS. TPC tracks are matched to the SSD layers and matched with ITS points down to the innermost SPD layer. First the vertex position is used to guide the track finding and maximize efficiencies for primary tracks. Without the vertex position information is possible, then, to reconstruct displaced tracks from the interaction point.

- Back-propagation and refit of the track outward in ITS and TPC, up to the outer radius of the TPC. Extrapolation and track matching in the TRD.

- Propagation to the outer layer (TOF, HMPID, PHOS, EMCal) for Particle Identification.

- Reconstructed tracks are refitted inward TRD, TPC, ITS and re-propagated to the primary vertex reconstructed in the first step.

- Primary vertex recalculation using tracks to obtain the optimal resolution.

The output of the whole reconstruction operation is the Event Summary Data (ESD) which contains all the information about the event both at track or event level. Technically, the ESD is a ROOT tree (*TTree*) with objects of type *AliESDEvent* stored in the "AliESD.root" file. In order to allow a more efficient analysis a summary of the most relevant information is extracted from the ESDs in the format of Analysis Object Data (AOD). For each data sample, the files containing ESD and AOD are stored and distributed worldwide on the Grid, where the users can access them through AliEn, the ALICE Environment framework.

In the Kalman filtering phase it is therefore a good asset to evaluate the quality of tracking procedure between consecutive detectors. For example, the prolongation tracking efficiency between TPC and ITS is shown in Fig. 2.16, as a function of the transverse momentum. It has been studied in minimum bias $Pb-Pb$ events by using the TPC tracks as a reference and looking for the prolongation in the ITS [86]. The prolongation efficiency is above 97% in the whole momentum range (black points) when at least two points in the ITS are required. The efficiency exhibits a drop to 85% if one of the two points is constrained to be in the pixels detector (red points), due to the presence of inactive modules in the SPD. Fig. 2.16 also shows an agreement well within 2% between the Monte Carlo HIJING simulation (empty markers) and the data. It

is interesting to recall that despite the difference in the event shape and multiplicity, the ITS reaches the same tracking performance in $p-p$ and *PbPb* collisions [86], thanks to the high segmentation and the low material budget. The performance of the the global TPC+ITS ALICE tracking in terms of transverse momentum resolution is reported in Fig. 2.11: the resolution is about 10% for tracks of about 50 GeV$/c$ and goes well below 3% for tracks below 10 GeV$/c$.

2.4.3 Data quality assurance offline

The AliRoot Quality Assurance (QA) framework is aimed to provide an automatic way to assess the quality of the data at various level of Monte-Carlo simulation and Monte-Carlo and real data reconstruction. The various levels include Raw data, SDigits, Digits, RecPoints and ESDs. QA data objects are produced as ROOT histograms and are stored in a ROOT file. The comparison of these objects with either user defined values of with user defined reference result in a quality statement. More precisely, the result of the checking is represented per detector as a severity level in a bit map and stored in the QA object (*AliQA*). Each histogram is automatically cloned for the various Event Species (*kLowMult*, *kHighMult*, *kCosmic* and *kCalib*) and for the activated trigger classes. The statistics of the QA data objects is user defined. The number of events to process defines a cycle. A run can include several cycle and a cycle can span over several run. Since a run can included several event species, the filling of the histograms according to the event species is controlled by the framework.

Chapter 3

The Time-Of-Fight (TOF) detector

The large Time-Of-Flight (TOF) array is one of the main detectors devoted to charged hadron identification in the midrapidity region of the ALICE experiment at the LHC. It separates pions from kaons at 3σ up to 2.5 GeV/c, and protons from kaons up to 4 GeV/c, where most of the interesting particles are created in the hadronization of the hot deconfined medium.

The TOF [87] is a large area detector covering a cylindrical surface of 141 m^2 with an inner radius of 3.7 m, a pseudorapidity interval $|\eta| < 0.9$ and full azimuthal coverage. It exploits the innovative Multigap Resistive Plate Chamber (MRPC) technology [88], capable of an intrinsic time resolution better than 50 ps with an efficiency close to 100% and a large operational plateau. Each MRPC is segmented into 96 readout pads of area 2.5×3.5 cm^2. The whole system is made of 1593 MRPCs, for a total of 152928 channels, arranged into 90 gas-tight modules which are grouped into 18 SuperModules (SM) each covering an azimuthal angle of 20 degrees. Taking into account all the time uncertainties that will be explained in this chapter, the overall resolution of the ALICE TOF detector, in $Pb-Pb$ collisions, reaches the design value of about $\sigma_{TOF} = 80$ ps [89].

Before going into technical details and performance it is convenient to explain what behind the technique of the time-of-flight.

3.1 The time-of-flight technique in ALICE

The time-of-flight technique consists in measuring the β factor of a particle by the independent measurements of the time of flight t and the length L of its trajectory, from the vertex of production to the sensitive element of the timing system. The ALICE TOF is located at 3.7 m from the beam axis: with a magnetic field of 0.5 T, the momentum threshold for this detector, calculated only from geometrical constraints is ~ 280 MeV/c. Taking into account the material budget, according to a Monte Carlo simulation [87], the momentum threshold is ~ 300 MeV/c for $\pi^{\pm}$, ~ 350 MeV/c for $K^{\pm}$ and ~ 450 MeV/c for protons and antiprotons. With the momentum information available it is therefore possible to obtain an indirect measure of the mass of the particle. A particle of momentum p, moving on a trajectory of length L with a time-of-flight t has a mass m

$$m = \frac{p}{\beta\gamma_L} = p\sqrt{\frac{t^2}{L^2} - \frac{1}{c^2}}. \tag{3.1}$$

The resolution of the mass depends on three terms, that are functions of the resolution on the momentum, on the time-of-flight and on the track path: length

$$\frac{1}{m}\frac{\partial m}{\partial p} = \frac{\delta p}{p} \tag{3.2}$$

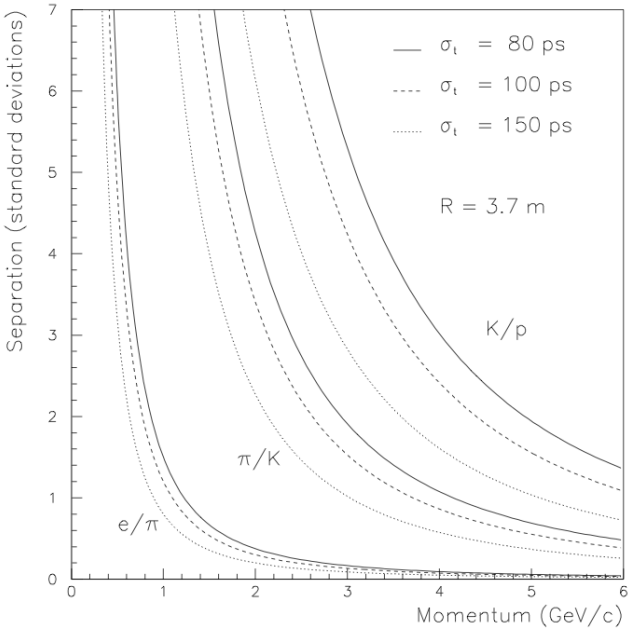

Figure 3.1 Analytical computation of the particle separation with a TOF detector, given a global time resolution σ_t (in the notation adopted here $\sigma_t \equiv \sigma_{TOF} \equiv \delta t$) [87].

$$\frac{1}{m}\frac{\partial m}{\partial t} = \left(\frac{E}{m}\right)^2 \frac{\delta t}{t} \tag{3.3}$$

$$\frac{1}{m}\frac{\partial m}{\partial L} = \left(\frac{E}{m}\right)^2 \frac{\delta L}{L} \tag{3.4}$$

Square-summing these three terms we get

$$\delta m^2 = \left(\frac{m}{p}\right)^2 \delta p^2 + \frac{p^2+m^2}{t^2}\delta t^2 + \frac{p^2+m^2}{L^2}\delta L^2 \tag{3.5}$$

from which one can sees that if $p \gg m$, the mass resolution is mainly determined by the resolution on the time-of-flight and on the track length.

Assuming no uncertainties in the evaluation of the time zero of the event (for convenience $t_{ev} = 0$) and a global TOF resolution of 80 ps - the designed resolution proposed in [87]) - it is easy to predict that the detector can achieve a 3σ separation for π/K up to transverse momenta of about 2.5 GeV$/c$, 4 GeV$/c$ for K/p separation. To distinguish two particles with the same p and L but with different masses indeed, it is necessary that the difference between the two time-of-flights is larger than the measure resolution. The difference between the time-of-flight of two different particles of mass $m_{i,j}$ with same p and L is derivable by Eq. 3.1 indeed as:

$$\Delta t = \frac{L}{2c}\frac{m_i^2 - m_j^2}{p^2}. \tag{3.6}$$

The capability to distinguish these two particles, called *separation*, can be expressed in terms of number of sigma,

$$n_{i/j} = \frac{\Delta t}{\delta t} = \frac{L(m_i^2 - m_j^2)}{2cp^2\delta t}, \tag{3.7}$$

where δt is the global time resolution of the TOF detector, that in a more convenient way it will be denominated σ_{TOF} for what follows. The performance of a TOF system for particle ID

(PID) mainly depends, of course, on its intrinsic timing resolution. The nominal capabilities of a TOF array with a system resolution from 80 to 150 ps, located at R = 3.70 m from the vertex, are shown in Fig. 3.1 for particles emitted at 90 degrees.

In ALICE, the TOF total time resolution σ_{TOF} is the sum of different contributions related to the its layout:

$$\sigma^2_{TOF} = \sigma^2_{MRPC} + \sigma^2_{TDC} + \sigma^2_{Clock} + \sigma^2_{ClTRM} + \sigma^2_{FEE} + \sigma^2_{Cal} \tag{3.8}$$

where σ_{MRPC} is the MRPC intrinsic time resolution ($\sigma_{MRPC} \sim 40$ ps), the intrinsic resolution of the readout boards - due to the signal digitalisation - is $\sigma_{TDC} = 20$ ps, σ_{Clock} e σ_{ClTRM} are the resolutions related to the fluctuation of the clock signal ($\sigma_{Clock} \sim 15$ ps) and its distribution towards the front-end cards ($\sigma_{ClTRM} \sim 10$ ps), $\sigma_{FEE} \sim 10$ ps is related to the jitter of the front-end electronics and σ_{Cal} summarises the uncertainties on the calibration constants, such as the cable lengths and paths on the readout boards [87].

As mentioned before, the time-of-flight used to identify a particle is measured with respect to the LHC clock. Since the bunches have a small but finite size and it is not possible to determine which of the particles in the bunches have collided, the actual time of the collision may differ from the nominal beam crossing by a time that is related to the size of the bunches[1]. Therefore, the event time has to be measured on an event-by-event basis and subtracted to the measured TOF time t. In the following, the event time will be referred as event-time, t_{ev}, of the event. Accordingly, the time-of-flight t taken to travel from the primary production vertex to the TOF layer will be $t - t_{ev}$ and the total time resolution will be affected by a contribution $\sigma_{t_{ev}}$. It is also worth noting that up to the present, we assumed no major influences on the knowledge of the length L of the trajectory and the momentum of the particles. In the most general case, without any approximation, one has to take into account explicitly all those time uncertainties coming from the measurement of these quantities, so that it is necessary to introduce a last term, σ_{trk}, that summarizes all the contributions deriving from the Kalman-Filter tracking procedure. Anyway, when treating the performance of the TOF detector (Sec. 3.3), it will be easy to understand that these are minor correction, especially when considering tracks with momentum greater than 1 GeV$/c$.

In conclusion, the most general expression for the detector global time resolution is

$$\sigma^2_{tot} = \sigma^2_{TOF} + \sigma^2_{trk} + \sigma^2_{t_{ev}} \equiv \sigma^2(p, m_i, t_{ev}), \tag{3.9}$$

in which the dependence from the momentum, particle species and event time is highlighted, as it will be more extensively shown in Sec. 3.3.

3.2 The ALICE TOF detector

A large-coverage TOF detector, operating efficiently, with an excellent intrinsic response and an overall occupancy not exceeding the $10-15\%$ level at the highest predicted charged-particle density of $dN/d\eta = 8000$ was required to fulfil ALICE physics purposes. This led to the current design with more than 10^5 independent TOF channels. Since a large area had to be covered, a gaseous detector was chosen. In the framework of the LAA project at CERN an intensive *R&D* programme has shown that the best solution for the TOF detector was the Multi-gap Resistive-Plate Chamber (MRPC) [71].

[1] This would be true even if the bunch crossing would be synchronized with the LHC clock.

3.2.1 RPC and MRPC

Resistive Plate Chambers are ionization chambers whose parallel plates (the anode and cathode) produce an uniform electric field inside the whole sensible volume. When a charged particle goes through this volume it produces a primary ionization that, if the field is strong enough, gives rise to an avalanche process. The signals read by the pick-up electrodes (*pads*) on the anode and the cathode plates are produced by the motion in the electric field of the electron-ion pairs created in the avalanche process. The advantages of the parallel plate configuration with respect to a traditional wire chamber with a radial electric field is that the drift effect on electrons disappears: since the field is uniform, the electrons do not have to travel before to reach a volume where the field is strong enough to produce an avalanche. This means that there is no time uncertainty related to the point where the primary ionization is produced. This point determines only the amount of charges produced, and so it is strongly related to the efficiency. The only condition to generate a signal is that the avalanche has travelled enough to produce a signal over the detectable threshold. This length has no influence on the time resolution of the device but only on the time elapsed between the crossing of the particle and the arrival of the signal.

The uncertainty related to the signal formation has two components: on one side the fluctuation of the number of primary pairs, which has a poissonian distribution dependent only on the gas type and not on the electric field, and which has an influence only on the detector efficiency. On the other side there is the fluctuation on the development of the avalanche, which influences the time resolution. The detector intrinsic time resolution is therefore due to the fluctuations of the time required to create (in the avalanche) a sufficient number of electrons to produce a signal over a threshold that depends both from the detector layout and the performance of the front-end electronics. The amount of time in which the signal is strong enough to be over this threshold before the discharge is called Time-over-Threshold (ToT). The time resolution can be estimated in the following way:

$$\sigma_t \sim \frac{1}{(\alpha - \eta) v_D} \tag{3.10}$$

in which α is the Townsend coefficient, η is the attachment coefficient and v_D is the electron drift velocity. All this parameters are related to the type of gas and to the strength of the electric field.

Despite their good performance, traditional RPCs are not satisfactory for the ALICE TOF necessities. As already said, they are made of two parallel plane electrodes of high resistivity material to prevent the formation of a spark inside the detector. The applied potential can be high enough to work in the streamer region so the RPCs have an efficiency close to 100%. Despite all that, they cannot be employed because of the high radiation characterizing $Pb-Pb$ collisions at the LHC. In such conditions the efficiency and the time resolution would largely decrease due to the pile up of the charges induced on the resistive planes which also would reduce the electric field inside the gap.

The problem could be avoided decreasing the resistivity of the plate; in this way the induced charges would be dissipated faster but the efficiency would be lower since the signal would extend over a larger number of read-out channels. Another solution could be the reduction of the amount of charges operating in the avalanche mode (instead of in the streamer one), making the gap thinner or the electric field lower. The disadvantages of such choice would be that in the first case the efficiency would decrease, since the first ionization process depends on the quantity of crossed gas, while in the second case the time resolution would worsen according to Eq. 3.10.

A compromise between the time resolution and efficiency requirements has been imple-

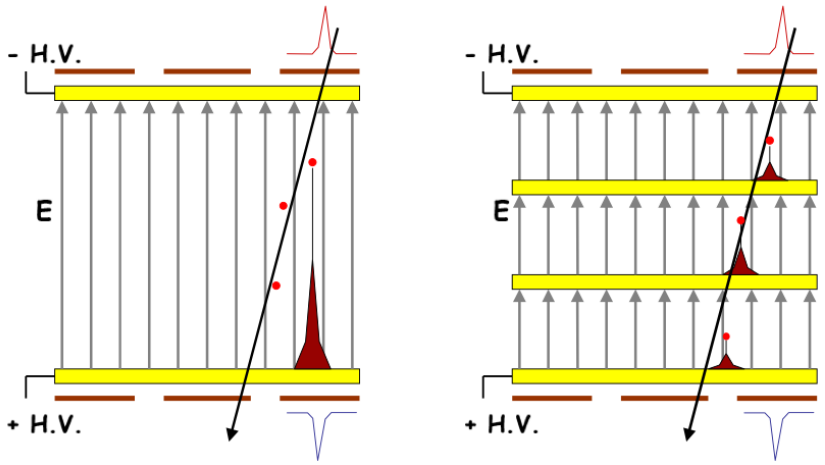

Figure 3.2 Schematic diagram and principle of operation of the RPC (left) and the MRPC (right).

mented with the TOF double-stack Multigap RPCs. The choice of using Multigap Resistive Plate Chambers [90] as basic unity for the TOF comes from the possibility to achieve very low intrinsic time resolution, not bigger than $\sigma_{MRPC} \sim 50$ ps, while operating in presence of a high track multiplicity and potentially high detector occupancy. One MRPC stack is a chamber formed by two parallel resistive planes where the gap between the electrodes is divided in a given number of smaller gaps by electrically floating high-resistivity planes, that are transparent to the fast signals coming with the electrons. The avalanche induced by the passage of ionizing radiation stops at each intermediate plane in such a way that its dimension is constrained and the time resolution is improved. The signal on the pick-up electrodes is induced by the movement of the fast electrons towards the the anodic planes and it is the analogue sum of the signals given by each avalanche. The active volume of the detector is simply the sum of each gap. In a double-stack MRPC, two single MRPCs share the anodic plane: the electrodes are closer so that border effects between adjacent pads are smaller and the number of gaps can be increased while the applied potential difference can be half.

Fig. 3.3 depict the layout of a TOF double-stack MRPC. It consits of a 10-gaps double-stack MRPC *strip* 122 cm long and 13 cm wide, with an active area of 7.4×120 cm^2, segmented in 96 readout pads, each of 3.5×2.5 cm^2. The external planes are 550 μm thick glasses with surface resistivity $\rho = 2 \div 25$ M$\Omega/\Box$. The High Voltage (HV) is applied through electrodes connected to their external surface. The Printed Circuit Boards (PCB) with the readout pads are layered externally together with the honeycomb panels that maintain the rigidity of the system. The five gaps per stack are created by four internal glasses, 400 μm thick, that are kept at a distance of 250 μm by a Mylar fishing line. The strips are filled with a non-flammable gas mixture made of $C_2H_2F_4$ (90%) SF_6 (5%) and C_4H_{10} (5%) that allow respectively to

- reach a high ionisation density;
- quench the photons from recombination of the primary ion pairs;
- absorb the electrons that are emitted by the cathode and prevent the production of secondary avalanches.

Despite the fact that the total gas volume is quite reasonable, 16 m^3, the costs of the gas mixture have lead to design a close circuit for gas circulation in the modules, the flux being approximately 2.7 m^3/hour and new gas being injected every few days. The MRPCs performance

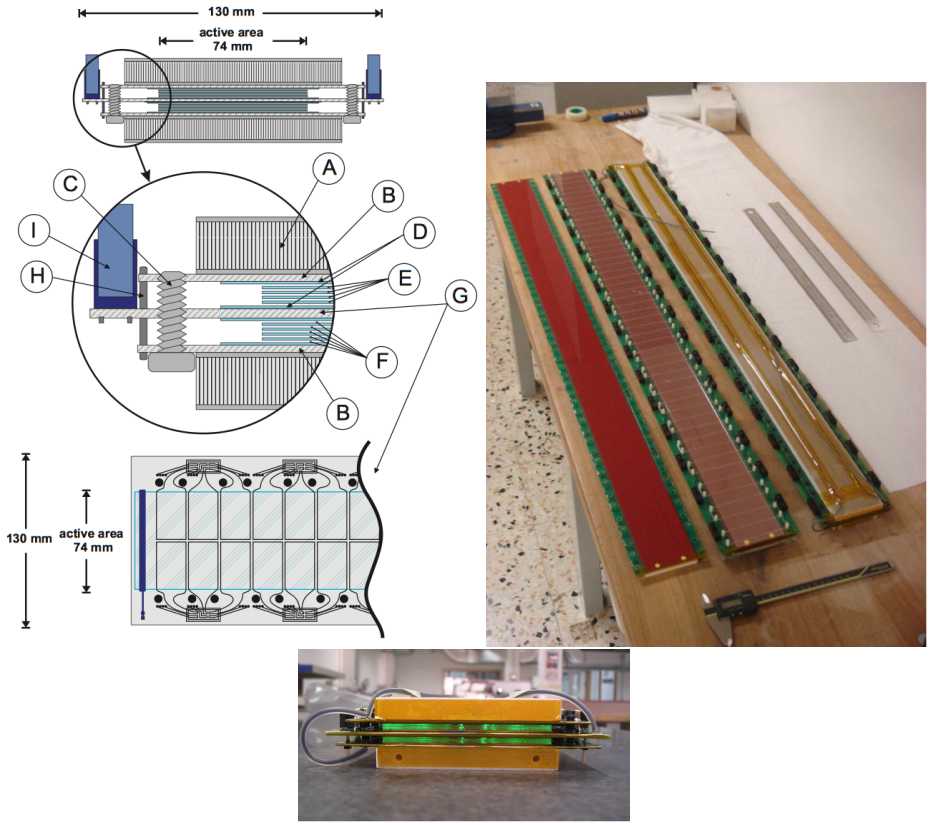

Figure 3.3 Pictures and a schematic diagram of a double-stack MRPC: (*A*) honeycomb panel to guarantee good mechanical rigidity; (*B*) Printed Circuit Board (PCB) with the cathode pick-up pads; (*C*) nylon pin to stretch the fishing line; (*D*) 550 μm glasses with resistive coating used to apply the voltage; (*E*) 400 μm glasses; (*F*) 250 μm gaps; (*G*) central PCB with the anode pick-up pads; (*H*) metallic pin soldered to cathode and anode PCB; (*I*) 16 pin connector. On the bottom, layout of the readout pads.

was tested with test beam at CERN with the final readout chain for a sample of mass-production strips [91]. The measured efficiency and intrinsic time resolution are reported as function of the HV applied to the electrodes in Fig. 3.4. With a HV of 13.0 kV, the TOF MRPCs have an intrinsic time resolution lower than 50 ps, (including the contribution of the readout electronics, estimated to be nearly 30 ps) and efficiency close to 100%. The operating voltage has been chosen to be this value, that is 13 kV. With the applied configuration, the growth of the avalanches in the gas volume is dominated by spacecharge effects and the MRPC can operate in saturated avalanche mode. The average charge produced by a through-going particle is small, at the level of 2-3 pC. As a consequence, the MRPCs are well suited to work at high rate. The high electric field, and the derived high drift velocity, allows to reach very good time resolution.

Nonetheless Fig. 3.4 shows a very good uniformity of the strips behaviour, common to several test samples. Finally the response of the detector to high rate and high radiation dose was tested at the Gamma Irradiation Facility (GIF) at CERN. Measurements have shown no degradation of the results up to about 1 kHz/cm^2 and for a radiation dose greater than 3.5 times the dose foreseen in the first 10 years of the LHC operation.

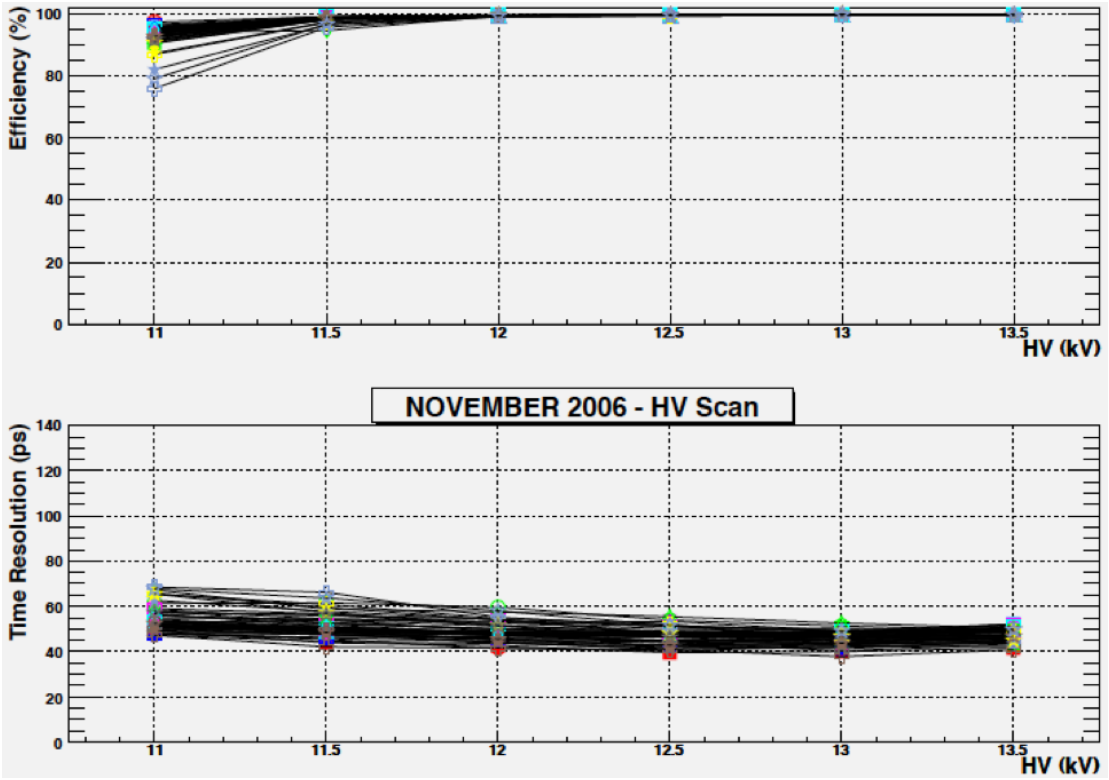

Figure 3.4 Efficiency and time resolution as a function of high voltage for a sample of mass-production MRPC strips. These data, referring to test beam, have been collected by using a standard gas mixture (see the text). With this mixture a HV of 12.5kV could be chosen as nominal value. However, the curves shift of about 500 V on the right if an isobuthan-free mixture is used. The choice of removing the flammable isobuthan component from the mixture when in ALICE, lead to the setting of the nominal value to 13.0 kV.

3.2.2 Overall layout of the TOF detector

The detector covers a cylindrical surface of polar acceptance $|\theta - 90^\circ| < 45^\circ$. It has a modular structure corresponding to 18 sectors in ϕ and to 5 segments in the z direction (that is the direction of the beam axis). The whole device is inscribed in a cylindrical shell with an internal radius of 370 cm and an external one of 399 cm. The whole device thickness corresponds to 30% of a radiation length. The strips are placed inside gas-tight modules (which also act as Faraday cages) and positioned transversely to the beam direction. Five modules of three different types extend along the full cylinder height, in the z direction. They all have the same structure and width (128 cm) but differ lengths. The actual dimensions and overall design are defined in such a way that the joining areas of the modules are aligned with the dead areas of the other detectors projected from the interaction point, thus creating a configuration of minimal disturbance for the external detectors. The length of the central module is 117 cm, the intermediate ones 137 cm, and the external ones 177 cm. The overall TOF barrel length is 741 cm (active region).

In order to minimise the transversal path of the incident particles through the chamber strips, a special tilted positioning of the strips was devised. This reduces the number of very oblique transversal paths that can create a sharing effect of the signal among adjacent pads, thereby increasing the occupancy and the time jitter of the detected signals. The angle of the strips with respect to the axis of the cylinder is progressively increasing from 0° in the central part ($\theta = 90^\circ$) of the detector to 45° in the extreme part of the external module ($\theta = 45^\circ$). This arrangement

makes the median zone of a strip perpendicular to a radius coming from the interaction point, thus minimising the angle of the incoming particles with respect to the normal direction. In order to avoid dead areas, adjacent strips were overlapped inside the modules so that the edge of the active area of one pad is aligned with the edge of the next one. This gives the possibility of creating a full active area with no geometrical dead zones. The modules were designed in such a way to avoid any loss of the sensitive area, along the z-axis. The only dead area is due to the unavoidable presence of the supporting spaceframe structure. Every module of the TOF detector consists of a group of MRPC strips (15 in the central, 19 in the intermediate and in the external modules) closed inside a box that defines and seals the gas volume and supports the external front-end electronics and services. An aluminium-honeycomb plate is the backbone of the module and gives the necessary mechanical stiffness to the system. The honeycomb plate is 1.5 cm thick including two aluminium skins, each 0.1 cm thick. A cover connected to the backbone by means of screws and standard sealing O-Ring closes the total gas volume; it has to withstand the overpressure required for gas circulation inside the chamber (less than 3 mbar). The cover is made of fibreglass 0.3 cm thick, reinforced with moulded ribs, protruded by 1.8 cm; there are 6 ribs in the central module, 9 in the intermediate and 8 in the external ones. A 0.04 cm fibreglass web, covered by a 20 μm aluminium layer, is glued to the inside surface of the cover in order to create an electromagnetic shielding. Inside the gas volume, fixed perpendicularly to the honeycomb plate, there are two macrolon plates, 0.5 cm thick, to which the MRPC strips are attached. The system turns out to be very simple and allows for a fast insertion of the strips at whatever angle is needed. Holes that accommodate feed-through for the signal cables coming from the readout pads, the HV connectors and the gas inlet and outlet, are machined into the honeycomb plate. The signal feed-through is made of a PCB having on one side connectors receiving the cables coming from the strips inside the gas volume and, on the other side, connectors that accommodate the front-end electronic cards, see Fig. 3.5. The PCB is glued to the honeycomb plate via special fibreglass gaskets which are inserted into the holes. The volume containing the electronic cards, input and output cables, gas pipes, water cooling pipes and radiators is closed by a 0.15 cm aluminium cover. This allows access to the electronics with no disturbance to the active part of a module. The complete TOF system consists of 90 modules. Three central modules in front of PHOS have not been installed in order to reduce the amount of material for this high resolution electromagnetic calorimeter in three of its five modules. The five modules in a row are located inside a supermodule framework of longitudinal and transverse aluminium beams for each of the 18 sectors. Pairs of horizontal and vertical rollers are attached to the supermodule body permitting the insertion of the supermodule into the space-frame sector where two rails are fixed. Each supermodule has an overall length of ~ 930 cm and a weight of ~ 1.4 t. A schematic layout of one supermodule inside the ALICE spaceframe and a photo of an assembled supermodule are shown in Fig. 3.6. An overview of the TOF detector parameters is shown in Fig. 3.7

3.2.3 Front end electronics and readout

A schema of the front-end and readout electronics of the TOF is reported in Fig. 3.8. The Front End Analogue (FEA) cards placed inside the modules (see Fig. 3.6) are in charge of reading the differential signal coming from the MRPCs. The FEA contains three NINO ASIC chips (see Fig. 3.9 and Ref. [92]), that are 8-channel amplifier/discriminator devices with an output width correlated to the charge of the input signal, the already mentioned Time over Threshold (ToT). The minimum value of the ToT is 6 ns. The charge information is important to apply the

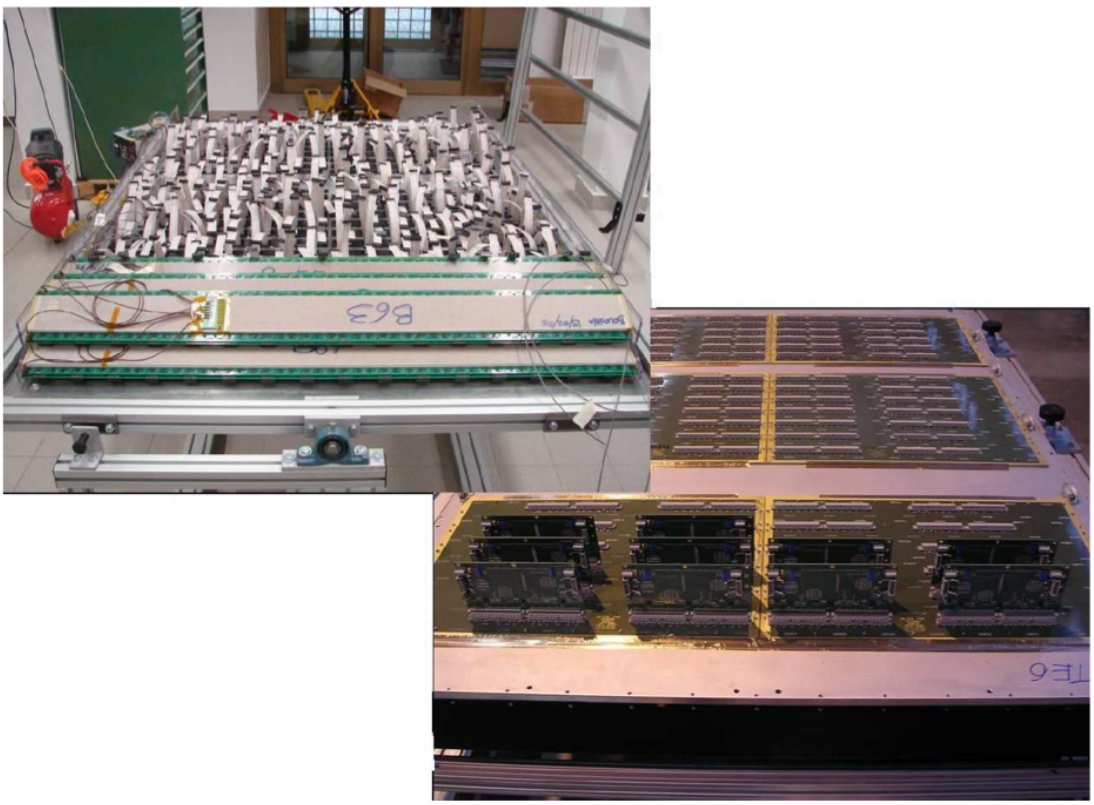

Figure 3.5 Photographs of a TOF module during assembly. The strips are installed inside the gas volume (*upper*) and the FEA cards are plugged onto the PCB connectors (*lower*).

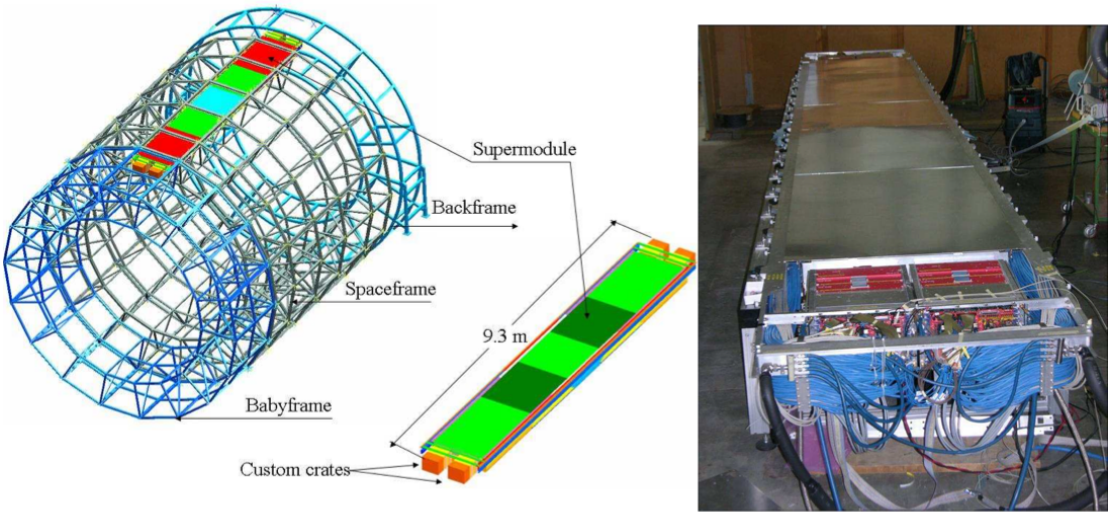

Figure 3.6 Schematic drawing of one TOF supermodule, consisting of 5 modules, in the ALICE spaceframe (*left*). A supermodule after assembly; in the foreground, the two custom crates with readout electronics (*right*).

Pseudo-rapidity coverage	$-0.9 < \eta < 0.9$
Azimuthal coverage	360°
Radial position	$370 < r < 399$ cm
Length (active region)	741 cm
Segmentation in φ	18-fold
Segmentation in z	5-fold
Total number of modules	90
Central module (A)	117×128 cm^2
Intermediate module (B)	137×128 cm^2
External module (C)	177×128 cm^2
Detector active area (total area)	141 m^2 (171 m^2)
Detector radial thickness	$X/X_0 = 29.5\%$
Number of MRPC strips per module	15 (A), 19 (B), 19 (C)
Number of readout pads per MRPC strip	96
Module segmentation in φ	48 pads
Module segmentation in z	30 (A), 38 (B), 38 (C) pads
Readout pad geometry	3.5×2.5 cm^2
Total number of MRPC strips	1638
Total number of readout pads	157 248
Detector gas	$C_2H_2F_4$(90%),i-C_4H_{10}(5%),SF_6(5%)
Gas volume	17.5 m^3
Total flow rate	1 m^3/h
Working overpressure	< 3 mbar
Fresh gas flow rate	0.02 m^3/h
Number of readout channels	157 248
Number of front-end analogue chips (8-ch)	19 656
Number of front-end boards	6 552
Number of HPTDC chips (8-ch, 24.4 ps bin width)	20 520
Number of HPTDC readout boards (TRM)	684
Number of readout boards (DRM) and crates	72
Occupancy for $dN_{ch}/d\eta = 8000$	14% ($B = 0.5$ T)
Occupancy for pp	10^{-4} ($B = 0.5$ T)
π, K identification range (with contamination < 20%)	0.5–3.0 GeV/c
p identification range (with contamination < 15%)	0.5–6.0 GeV/c
e identification range in pp (with contamination < 10%)	0.3–0.5 GeV/c
Event size for $dN_{ch}/d\eta = 8000$	110 kB
Event size for pp	24 kB

Figure 3.7 Overview of TOF parameters.

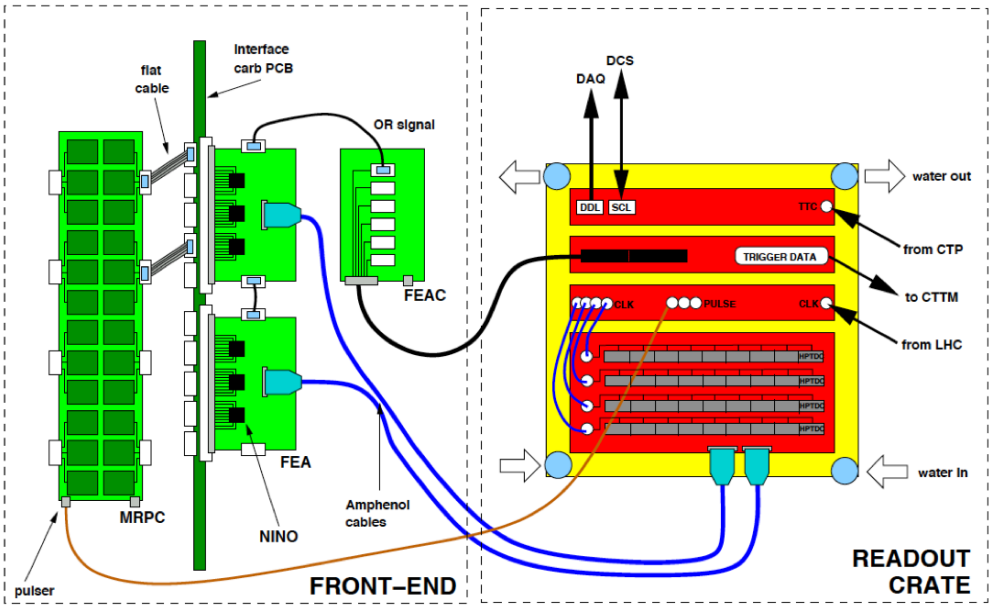

Figure 3.8 Scheme of the TOF front end and readout electronics.

correction for time slewing[2]. Each FEA reads 24 pads displaced in two rows, corresponding to 8 channels $\times$ 3 NINO chips, so that one strip is read by four FEAs. The discriminated signal is sent to the readout component of the system, the TDC Readout Module (TRM) for the time measurement.

Moreover, the OR of two neighbouring FEAs is sent to the FEAC board (still placed inside the SMs). The FEAC supplies a group of 10 or 12 FEAs with the low voltage (2.5 V) power, monitors their temperature through a set of sensors, sets the threshold voltages on the discriminator and collects the OR signals thanks to a Fully Programmable Gate Array (FPGA). The FEAC output is sent to the Local Trigger Module (LTM). According to this configuration, a "trigger hit" is defined if at least one hit has been recorded by any of the 96 pads of 2 half-strips. The group of half-strips connected to a FEAC is also referred to as "maxi-pad". The purpose of these signals is twofold: they can be used to send a fast pre-trigger to the Transition Radiation Detector and to contribute with a Level 0 (L0) trigger to the physics event selection thanks to its 1690 channels, each covering 888 cm^2. The TOF trigger has been widely used both to trigger on cosmic muons both for central detectors calibration and for cosmic-ray physics [87] and to contribute to the selection of minimum bias events in $p-p$ collisions. During *PbPb* data taking in 2010 and 2011, and the $p-Pb$ runs of 2013, the TOF topological trigger has also played a fundamental role in the trigger for Ultra Peripheral Collisions (UPC), as it will be deeply discussed in the next chapter. A large electronics board, the CTTM (Cosmic and Topology Trigger Module), located under the muon spectrometer platform, receives the LTM signals, asserts the L0 and L1 triggers and sends them, within 800 ns after the collision, to the Central Trigger Processor (CTP), which provides the L0 trigger for the whole experiment.

The discriminated signals are transferred from the front-end electronics to a custom VME crate where they are digitized. Each side of a supermodule hosts two crates, as shown in Fig. 3.6, that contain four types of VME64 modules: the TDC Readout Module (TRM), the Local

[2]When two analogue signals that have different amplitudes but arrive at the same time are digitalised, the output values are different, because their leading edge reaches the TDC threshold at different times. The time-of-flight measurement is affected by this as it is obtained on the leading edge of the TDC signal.

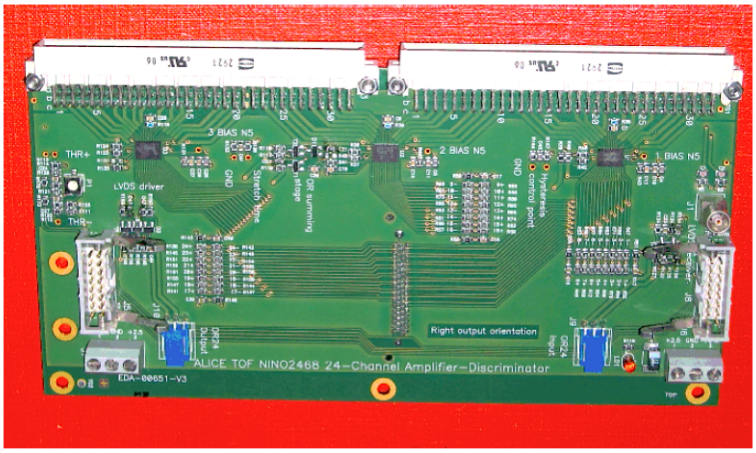

Figure 3.9 One of the TOF Front End Analogue (FEA) cards. The three NINO ASIC chips [92] are visible on the top of the picture. The board dimensions are (19.0×10.5) cm^2.

Trigger Module (LTM), the Clock and Pulser Distribution Module (CPDM) and the the Data Readout Module (DRM).

The TRM

The TRM manages the TDC readout operations. The left[3] crates house 10 TRMs (slots numbered from 3 to 12), the right crates only 9 (slots from 4 to 12). Each TRM hosts 10 mezzanine cards (piggybacks) with 3 High Performance Time To Digital Converter (HPTDC) chips that can read 8 channels, summing up to 30 HPTDCs that read 240 channels per board. The HPTDC determines the difference between the signal from the FEA and the trigger input, by relating it to a synchronous counter latched to the LHC clock. Only the hits that fall in a valid matching window (MW), starting $t_{latency}$ before the trigger arrival are transferred in the L1 FIFO of the HPTDC. Both $t_{latency}$ and the matching window are programmable. During the first three years of the LHC operations, these parameters have been set to MW = 600 ns and $t_{latency} = 9\mu$s, to be compared to the ALICE L1 trigger latency of 6.7 μs. In addition, the TRM deals with:

- HPTDC conguration;
- HPTDC hits reading;
- transfer of the data in temporary buffers embedded in an external RAM memory bank;
- data forwarding to the VME master module in a properly formatted form;
- nonlinearity correction: the TRM board also features an Integral NonLinearity look-up table, that is a correction code needed in the very high resolution mode of the HPTDCs.

The LTM

The Local Trigger Module is the first level of the TOF trigger, in charge of receiving the FEAC output and transferring it to the CTTM. It is also in charge of setting and monitoring low voltages and temperatures in the FEE section of the SM. Finally, each LTM sets the thresholds for the NINO discriminator on the FEAs and defines a delay to the trigger signals that compensates

[3]Left and right are determined by facing the SM from the ALICE A side.

for the different cable length whenever needed. Only one LTM module per crate is present and housed in the VME crate slot 2.

The CPDM

The Clock and Pulser Distribution Module receives the LHC clock via an optical fiber and sends the clock as a standard LVDS input to each VME module in a crate pair. The clock received by the CPDM is a dedicated clock parallel to the TTC system in order to reduce the jitter associated with it. In absence of an external clock, the CPDM delivers a clock locked to an internal oscillator. The CPDM also provides 17 LEMO outputs that are connected to the pulse lines of the MRPC strips, for monitoring the readout chain and calibration purposes. For each crate pair, the CPDM occupies the slot 3 in the right crate.

The DRM

The Data Readout Module installed in the Master VME slot of each crate is the interface between the TOF readout system and the ALICE DAQ and the main responsible for the crate readout. It has several important functions:

- it interfaces to the central ALICE DAQ system via the Detector Data Link (DDL). The TOF is equipped in total with 18 supermodules, read by 4 crates each, for a total of 72 crates, one per DDL. At present, six DDLs are linked to one LDC so that the output rate is not bigger than 5.7 KHz;
- it receives and decodes trigger signals and messages from the TTC system, it propagates to all the VME modules the bunch counter reset, L1 and L2 trigger signals. Part of the trigger information is stored in the data to be sent over the Detector Data Link (DDL) for consistency checks;
- it reads out the data in the LTM and TRMs of the crate and when a Level 2 (L2) trigger is issued it encodes the data stored in its buffer according to the common ALICE format;
- it hosts a single board computer from where it is possible to the reprogram the firmware for each of the FPGAs present on the crate;
- it monitors the condition of the readout and sets a busy 4 signal to the Auxiliary Control Module (ACM);
- it receives from the ACM an external pulse signal, for the detector calibration.

Finally, the DRM card is equipped with an additional optical link to a commercial PC which provides extra Slow Control functionalities. The 72 TOF crates are connected to 18 commercial PCs, grouped in such a way that one PC controls one entire SM.

3.3 TOF performance and Particles IDentification (PID)

In this section details about calibrations, PID capabilities, matching efficiency and evaluation of the time-zero of the event are given in terms of TOF performance. During the 2009-2013 data taking the TOF system had very stable operations with a time resolution of $\sigma_{TOF} = 80ps$, reaching the design value.

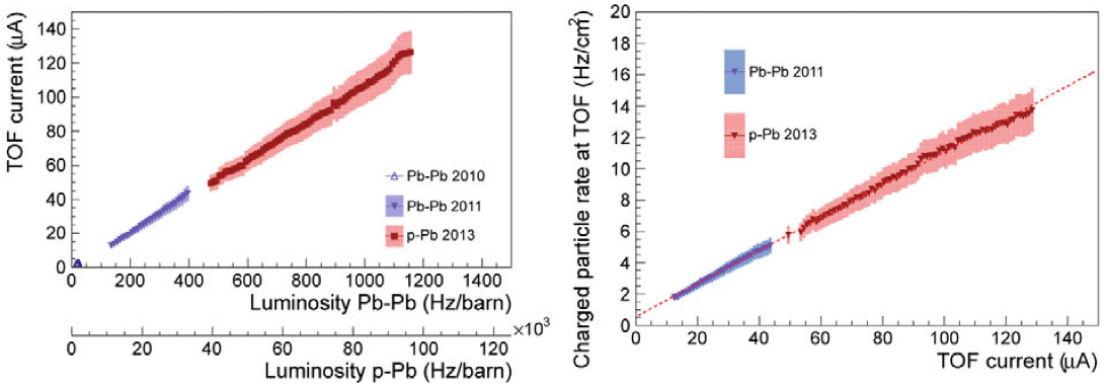

Figure 3.10 Left: the TOF current versus luminosity in $Pb-Pb$ and $p-Pb$. Right: the TOF estimated rate versus HV current. In both figures the points and the bands indicate the average and the spread of the measurements, respectively. The dashed line is the linear fit to the 2013 data [89].

3.3.1 MRPCs behaviour

The performance of the MRPCs was very stable along the first three years of the LHC operation. The TOF current[4] per MRPC during periods without circulating beams was measured to be on average of few nA. During the periods with beams the current of the MRPCs increased linearly with the LHC luminosity (Fig. 3.10-left), with no sign of deviations related to the occurrence of abnormal noise current. The two horizontal axis are aligned to the same detector load considering the average track multiplicity and the ALICE interaction rate [89]. Considering the interaction rate at ALICE and the TOF hit multiplicity per event it is possible to estimate the average rate of particles in the detector as a function of the TOF current. The calculation is shown in Fig. 3.10-right and it indicates a maximum average TOF rate of ≈ 14 Hz/cm^2. Considering the two plots in Fig. 3.10 it is possible to extrapolate the TOF rate to the luminosity foreseen in the ALICE upgrade beyond 2018 (5000 Hz/barn [93]). The expected rates will be 60 Hz/cm^2: when compared to test beam results, this value indicates that also in the high-luminosity LHC period the MRPCs are expected to operate without loss in performance. From 3.10-right it is possible to compute an average induced charge of ≈ 6 pC per track. This value is slightly higher than what obtained in test-beam [94], but still compatible considering that in ALICE the particles are of different species and cross the MRPC at different angles and with different momentum spectra. This low charge ensures a good rate capability and a slower ageing of the detector.

3.3.2 TOF Trigger

Taking advantage of its large coverage, fine granularity and fast signals, the TOF system has been extensively used as a trigger detector during different periods of the ALICE commissioning and data taking. The fine granularity of the TOF and the relatively low noise of the MRPCs (≈ 0.5 Hz/pad without beam) allowed triggering in several configurations, like back-to-back patterns in cosmic events or decays from resonances produced in ultra-peripheral collisions.

The trigger used to select cosmic events is based on a simple event topology: a trigger is delivered when there is a back-to-back coincidence between two sectors in the azimuthal plane. In order to increase the acceptance for low-momentum muons, this condition is relaxed allowing

[4] In the MRPCs the HV is applied with symmetric positive and negative values ($\pm$6500 V): the TOF current is defined as the sum over all MRPCs of the average of the two currents (positive and negative) and represents the total current flowing across the MRPCs.

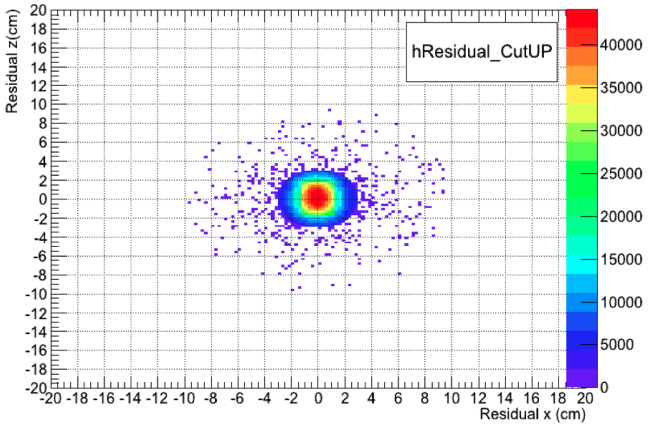

Figure 3.11 TOF residuals along both the x and z direction in 2010 $Pb-Pb$ collision at $\sqrt{s_{NN}}$ = 2.76 TeV. Even if for heavy-ion collisions the geometrical matching windows (MW) is set to 3 cm, the plot shows few entries for greater values since it is widened to the $p-p$ case ($MW = 10$ cm) to increase the TOF matching efficiency in the (very low multiplicity) ultra-peripheral collisions analysed in this work.

the trigger to fire also if one out of the three sectors on each side of the lower one has fired. The purity of the trigger was estimated measuring the in-gate and out-of-gate rates and was found to be 45%. This result is fully consistent with the offline data analysis where a cosmic muon track is found in $\approx 30\%$ of events. The rate has been very stable in time, about 95 Hz, allowing to collect hundreds of millions of muons to be used for TOF and other detectors calibration and for cosmic rays physics.

As already mentioned, the TOF trigger was also used to select resonance decays in UPC during the $Pb-Pb$ data taking in 2010 and 2011 and for $p-Pb$ collisions in 2013. These events are characterized by the presence of just few tracks coming from resonance decays and almost no other tracks in ALICE. The main task of the TOF trigger was the selection of such topologies requesting that only few tracks reached the detector. Thanks to the available segmentation it was possible to require a small number of fired TOF pads (between 2 and 10) with an additional azimuthal topological cut (at least two opposite hits with $150^\circ < \Delta\phi < 180^\circ$. See the next chapter for more information on this topic.

3.3.3 TOF and MRPC efficiency

The ALICE tracking algorithm has been described in Sec. 2.4. After the propagation through TPC and TRD, the tracks are extrapolated to the TOF sensitive layer. A geometrical matching window (MW) of 3 cm (for $Pb-Pb$ collisions) or 10 cm (for $p-p$ collisions) is opened around the intercept of the extrapolated track with the TOF sensitive layer. The algorithm looks for TOF clusters within this matching window and if any is found, the closest hit to the crossing point is associated to the track. The "matched" track is then propagated to the TOF layer. In $Pb-Pb$ the geometrical matching window is also widened to the $p-p$ value to increase the TOF matching efficiency in (very low multiplicity) ultra-peripheral collisions, as it appears from the distribution of the residuals[5] in $Pb-Pb$ events, see Fig. 3.11.

The TOF matching efficiency is defined as the ratio of the tracks matched by the TOF to those reconstructed using the ALICE tracking detectors, *i.e.* ITS, TPC and TRD. This quantity

[5]The quality of the tracking at the TOF-level is monitored by looking at the distance (or *residual*) in the pad reference frame between the extrapolated trackpoint at the TOF layer and the center of the pad containing the matched hit.

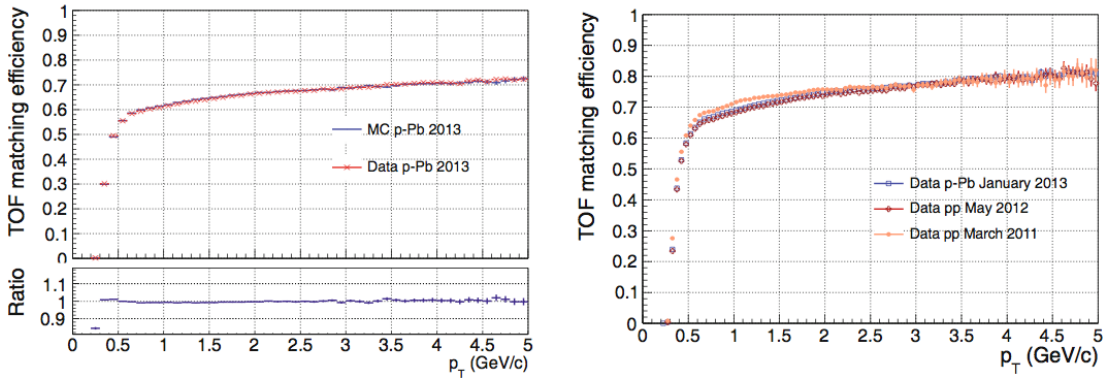

Figure 3.12 Left: comparison between the TOF matching efficiency measured in 2013 $p-Pb$ data and the one extracted from the corresponding simulation (*top*) and their ratio (*bottom*). Right: comparison between the TOF matching efficiency measured with 2011, 2012 $p-p$ data and with 2013 $p-Pb$ data, as in [89].

is obviously affected by the MRPC detection efficiency but also by the TOF geometrical acceptance, hardware data taking conditions, uncertainties in the track extrapolation, the materials located in front of the TOF and by the track-TOF matching algorithm efficiency. Mismatched tracks are those matched with a wrong TOF hit and clearly the interest is to have the TOF track matching efficiency as high as possible, while keeping the number of mismatched tracks as small as possible. Moreover tracks with $p_{\mathrm{T}} < 0.3$ GeV$/c$ do not reach the TOF detector due to the curvature of the trajectory in the magnetic field. For $p_{\mathrm{T}} > 0.3$ GeV$/c$ the matching efficiency rapidly increases until it saturates for $p_{\mathrm{T}} > 1$ GeV$/c$.

A typical behaviour of the TOF matching efficiency is shown in Fig. 3.12, where the matching efficiency measured in the 2013 $p-Pb$ data is also compared with the one simulated in the corresponding Monte Carlo production [89]. The Monte Carlo simulation takes into account the variations in the ALICE and TOF run conditions during the data taking. The tracking and the matching algorithms are common to both data and simulated events. The response of the MRPC detector as a function of the track impact point on the pad has been carefully simulated in the Monte Carlo according to a parametrization extracted from test beam results.The MRPC efficiency in the centre of a pad is taken to be $\sim 99.5\%$. Due to the readout structure of the MRPC, a particle crossing the MRPC close to a pad boundary induces a charge on the pad and a smaller charge also on the neighbouring pad(s). The border between two pads is defined as a 13 mm wide region where the pad efficiency decreases going towards the neighbour pad (from 99.5% to zero), while the efficiency of the nearby pad correspondingly increases (from zero up to 99.5%). This effect concerns three sides of each pad. Along the fourth side (which has no neighbouring pad) there is only a 4 mm wide region where the efficiency slightly decreases, dropping to 88.3% at the pad edge. In the Monte Carlo program, these effects are included by means of a two-dimensional parametrized efficiency function obtained combining beam-test scans across and along the MRPC. With this procedure, the overall simulated MRPC detection efficiency is sligthly reduced to $\sim 98.5\%$. In Fig. 3.12-left the agreement between data and Monte Carlo simulation is within 1%, confirming that the current simulation of the overall MRPC detection efficiency is realistic. The matching efficiency for tracks with $p_{\mathrm{T}} > 2.0$ GeV$/c$ has been stable throughout the years, as shown in Fig. 3.12-right. Under 2 GeV$/c$ the matching efficiency slightly varies due to a different number of TRD sectors installed at different times in front of the TOF: their contribution to the material budget and the presence or not of their position information affect the global tracking in ALICE and also the TOF matching efficiency.

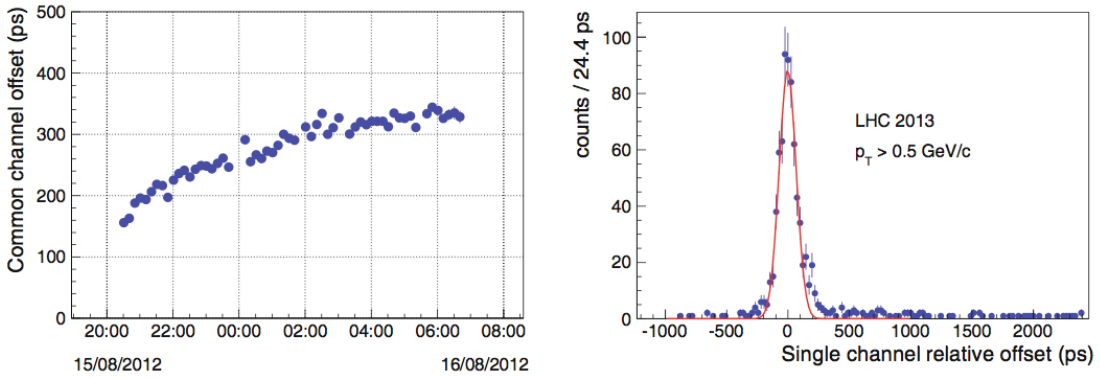

Figure 3.13 Left: common global offset as a function of time as measured in one LHC fill in 2012. Right: an example of a calibration fit used to extract the single-channel offset [89].

3.3.4 Timing calibration

The TOF time calibration is based on the determination of three components:

(i) a global offset, which is common to all the channels,

(ii) a channel-by-channel offset, which depends on the channel,

(iii) a time-slewing correction at the channel level.

All the three calibrations require full track reconstruction in the ALICE detector and, as a consequence, rely on the calibration of the main tracking device, the TPC, which also provides the momentum information.

Global offeset. The need to sample in time the global offset comes from the observation of a time shift in the LHC clock phase, which results in a non constant offset in the measured time of flight. This shift is due to the temperature dependence of the fibre refractive index, which affects the LHC clock time distributed to the experiments. The global offset is derived from a time sampling of the TOF data, using only particles with a reconstructed momentum $p > 0.5$ GeV$/c$ to assure a good tracking performance almost independent of the momentum. The measured arrival times of flight are compared to the expected times obtained from the measured track length and momentum in the pion mass hypothesis, the most abundant species produced in the collisions. The difference between the measured times of flight and the expected times is sampled in time (10 minute samples) for all tracks and the corresponding distribution is fitted with a Gaussian function whose mean corresponds to the global channel offset for the time interval under study (Fig. 3.13-left).

Channel offset. The channel-by-channel offset calibration accounts for the delays introduced in the measured times of flight by the cable lengths and by the electronics. Such calibration is carried out as for the global offset, but in this case the distribution of the differences between the measured and expected times is evaluated for every channel. Again, a Gaussian fit is performed for each distribution and its mean value gives the channel-by-channel offset. It is clear that a much larger statistics is needed to perform such a calibration, due to the fact that a minimum number of tracks per channel is required to assure a reliable fit. An example is shown in the right panel of Fig. 3.13. The calibration is repeated at regular time intervals in order to properly consider possible modifications of the TOF hardware configuration.

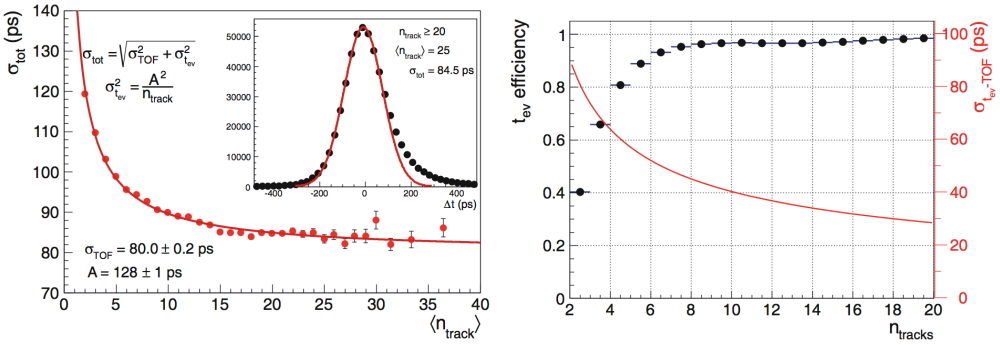

Figure 3.14 Left: total time resolution as reported in [89] for pion tracks on TOF with $0.95 < p < 1.05$ GeV$/c$ as a function of the number of tracks used to define the TOF event time. Data refer to 2013 $p-Pb$ collisions. The inset shows the original distribution for a track multiplicity on TOF > 20 which corresponds to an average of 25. Right: efficiency and time resolution for the TOF-based event time algorithm as a function of the number of tracks matched to TOF and available for the computation.

Time slewing corrections. The correction makes use of the correlation between the measured time and the signal width corresponding to the time interval during which the signal released by TOF remains over the threshold of the signal discriminator (ToT, see Sec. 3.2.3). The time slewing calibration is a channel-by-channel calibration. To reach the very high statistics necessary for this two-dimensional calibration, data are collected over very long periods (several months) or at every hardware intervention on the TOF: also in this case tests have shown no significant changes with time, as expected from the stable operations of the MRPCs and of the readout electronics. More informations about this correction can be found in [89].

After the above three calibrations, it is finally possible to evaluate the TOF performance in terms of time resolution. For tracks with a momentum in the range $0.95 < p < 1.05$ GeV$/c$ the difference between the measured time of flight and the pion time expectation is computed. The distribution is fitted with a Gaussian function, whose width σ_{tot} is the convolution of the intrinsic TOF time resolution σ_{TOF} and the event time (that is the collision time) resolution $\sigma_{t_{ev}}$, as in Eq. 3.9; in this case, the contribution from tracking is negligible for the momentum range considered (this point will be clearer in Par. 3.3.6). For the event time the one measured by the TOF itself is used, as described in Par. 3.3.5. Since the TOF t_{ev} resolution is expected to scale with the square root of the number of tracks used ($\sigma_{t_{ev}} = A/\sqrt{n_{tracks}}$), the measured σ_{tot} can be plotted *versus* n_{tracks} and fitted according to this expression. Fig. 3.14-left, obtained for $p-Pb$ collisions, reports the result of such fit indicating for $n_{tracks} \to \infty$ a value corresponding to a TOF time resolution of 80 ps. The inset shows an example of a Gaussian fit for a track multiplicity on TOF in excess of 20: the distribution has a tail on the right, which was not observed during test beams, and might be related to residual mis-calibrations which are currently under investigation.

3.3.5 Determination of the event time used by TOF

The TOF PID strategy is based on a time difference between the arrival time measured by the TOF and the event time, which is estimated event by event. The ALICE T0 detector was already mentioned to be the dedicated system assigned to this measurement. However, due to the detector acceptance, especially in $p-p$ collisions, no signals are observed by the T0 for a fraction of the events and, as a consequence, an estimate of the event time is not available from the detector. For these events the uncertainty in establishing the event time depends on the finite

size of the bunches and it varies between 80 and 200 ps with respect to the nominal time signal from the LHC: this uncertainty contributes in a significant way to the observed overall time of flight resolution σ_{tot}, affecting the TOF PID performance.

In order to reduce this contribution an alternative method was developed where the TOF information itself is used to determine the event time when at least three tracks have an associated TOF signal. This is done by means of a combinatorial algorithm which compares the measured TOF times to the expected times of the tracks, assuming a common event time t_{ev}. This latter quantity is obtained from a χ^2-minimization procedure [89]. In detail, for a given track j, the event time is determined using all the other tracks in the event and evaluating the following χ^2-expression for all possible combinations of masses (m_i, $i = \pi, K, p$):

$$\chi^2 = \sum_{n_{tracks}} = \frac{((t_{TOF} - t_{ev}) - t_{exp}(m_i))^2}{\sigma^2_{TOF} + \sigma^2_{t_{exp}}} \tag{3.11}$$

where the sum is over all tracks matched at TOF other than j, t_{TOF} is the track measured time and t_{exp} is the expected time with the mass hypothesis i. σ_{TOF} and $\sigma_{t_{exp}}$ are the corresponding errors. The combination that minimises the χ^2 is used to derive t_{ev} which is then subtracted from the TOF time associated to track j. This procedure, which is repeated for each track in the event, ensures that the measured event time is always independent of the TOF measured time of the track, thus avoiding possible biases in the determination of t_{ev}. A check on the χ^2 value of each used track and of the final t_{ev} is also performed in order to reject tracks not consistent with the sample for any mass hypothesis (mismatched tracks) and eventually to reject also the event time: this implies a reduction in the efficiency of the algorithm, depicted in Fig. 3.14. Here the contribution to the total time resolution due to the t_{ev} as calculated with the TOF is reported, indicating that it becomes negligible when the number of tracks is high (≈ 25 ps at $n_{tracks} = 30$.

In the physics analysis the event time is determined combining the t_{ev} estimated by the T0 detector and by the TOF tracks, weighted by the respective resolutions. For the small fraction of events where none of the two measurements is available the event time is taken as the average obtained during the run, of course with a much worse resolution on t_{ev}.

3.3.6 PID

The TOF performance obtained through the calibration and data analysis described in previous sections are first summarized in terms of the measured β-momentum correlation for tracks matching the TOF, as shown in Fig. 3.15-top. In this figure pions, kaons and protons are clearly separated in the intermediate p_{T} range. Points corresponding to non physical values in the $\beta - p$ plane are due to mismatched tracks at TOF, *e.g.*, hit registered at TOF but not associated to the true track. The amount of this background depends on the type of the collisions and it can be reduced at low momentum using the TPC dE/dx information.

Analysing data with the TOF detector, the simplest PID estimator $\hat{I}_{TOF,i}$ for a given mass hypothesis m_i ($i = e, \mu, \pi, K, p, d, t, {}^3He, {}^4He$) is constructed as an $n\sigma$ quantity, assuming a Gaussian description of the response function of the detector, in the following way:

$$\hat{I}_{TOF,i} = \frac{t_{TOF} - t_{ev} - t_{exp}(m_i, p, L)}{\sigma_{tot}(p, m_i, t_{ev})}, \tag{3.12}$$

with the common notation where t_{TOF} is the hit time measured by the TOF detector, t_{ev} is the event time of the collision and t_{exp} the expected time for a particle of mass m_i, momentum p and track length L reaching the TOF. The PID variable is then used to implement simple 2 or 3 σ cuts, depending on the requirements of the specific analysis. The good understanding of the

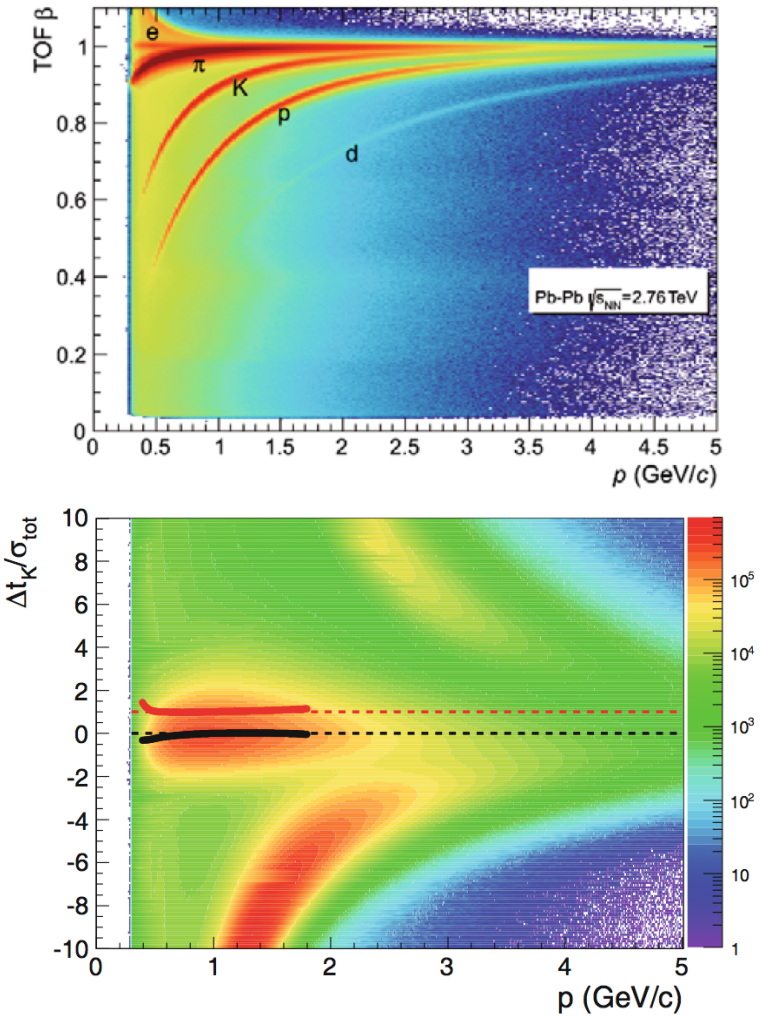

Figure 3.15 Correlation $\beta = v/c$ *versus* momentum as observed by TOF in $Pb-Pb$ collisions after the calibration procedures (*top*). Deviation, in terms of $n\sigma$, *versus* the track momentum considering the kaons expected time (*bottom*). The accumulations corresponding to pions and protons are clearly visible. Points indicate average (*black*) and width (*red*) of the distribution for each momentum bin[89]

detector response and parametrization of its resolution is confirmed by monitoring the average values (expected around zero) and pulls of the distribution of this variable (expected around 1). As an example, the distribution of this variable as a function of momentum for the kaon hypothesis is shown in Fig. 3.15-bottom. Pions and protons are also visible as well as the region where pions start worsening the purity of a selected kaon sample. Each momentum slice has been fitted with a gaussian fit bound to $[-2,2]$ values and the resulting mean and width of the distribution are plotted as black and red points. By construction the fitted width corresponds to the pull of the distribution of the PID variable. In the range where there is no contamination from pions the values are in nice agreement with the expected values for mean and pull of the variable (0 and 1, respectively, represented by the dashed lines) validating the description of the resolution function[6].

It is worth noting that the resolution function $\sigma_{tot}(p, m_i, t_{ev})$ entering the Eq. 3.12 is the same

[6]Note that in $Pb-Pb$ at low p_{T} (below 400 MeV$/c$) the presence of mismatched tracks alters the distribution, but this contribution can be removed using the TPC information.

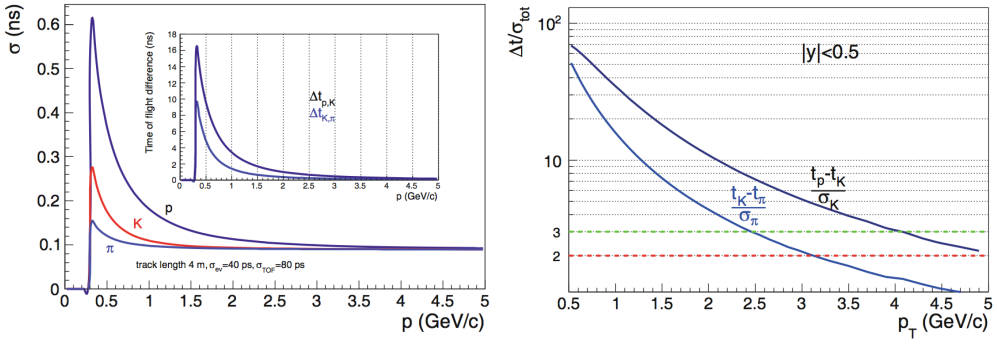

Figure 3.16 Left: resolution function for PID as a function of momentum p for protons, kaons and pions assuming $\sigma_{TOF} = 80$ ps, $\sigma_{t_{ev}} = 40$ ps and a 4 m track length. In the inset the expected time-of-flight difference between protons and kaons and kaons and pions for a 4 m track length is also shown. Right: the present separation power of the TOF for kaon-pion and proton-kaon as a function of p_{T} [89].

expressed by Eq. 3.9. In the general case (therefore, not for calibration purposes as described in Par. 3.3.4) the contribution due to the tracking must been taken into account. It has been parametrized as a function of the momentum on the basis of real data and using Monte Carlo simulations, as shown in Fig. 3.16-left. In absolute terms this contribution becomes dominant at small momenta for heavier particles, but, on the other hand, the expected time difference increases much more, as shown in the insert of the figure.

As a summary of the presented results and in comparison with the analytical computations depicted in Fig. 3.1, the actual separation power of the TOF for kaon-pion and proton-kaon as a function of p_{T} is shown in Fig. 3.16-right. Operatively, the separation is computed as the distance between the peaks divided by the Gaussian width σ_{tot} of the pion or the kaon response, respectively. Usually this is shown as a function of total momentum p, however, since most physics results are reported in transverse momentum bins, here the separation power in p_{T} bins is reported, averaging the momentum-dependent response over the range $|y| < 0.5$.

Chapter 4

Analysis and results on the J/ψ and e^+e^- photoproduction

This last chapter aims to describe the recent experimental studies on the photoproduction of charmonium states (J/ψ and ψ') and e^+e^-pairs at mid-rapidity in ultra-peripheral $Pb-Pb$ collisions at $\sqrt{s_{NN}} = 2.76$ TeV. The results of this analysis have been recently published by the ALICE Collaboration on November 2013 in [1]. The study of the J/ψ production at midrapidity is focused on the coherent and incoherent processes, while those obtained at forward rapidity include only coherent production [95]. The coherent J/ψ production, both at midrapidity and forward rapidity, has been compared with the theoretical predictions available.

The conclusions highlighted in this thesis constrain, at $Q^2 \approx 3$ GeV^2, the nuclear gluon distribution at Bjorken-$x \approx 10^{-2}$ and $\approx 10^{-3}$ for the forward and central rapidity bin, respectively. It is worth noting that this analysis reports the the first LHC results on the topic of photoproduction and moreover, the first significant quantitative conclusions for the J/ψ photoproduction, after those obtained in the past in DIS at higher Q^2.

4.1 Analysis of coherent and incoherent photoproduced J/ψ

This section will concentrate on the results of the photoproduction cross section of coherent and incoherent J/ψ s, while the analysis of the $\gamma\gamma$ interactions will be presented in the Sec. 4.2. However, owing to the same analysis flow for both two processes, the intermediate results (event counting, systematics, ...) will be reported here, leaving for the next section the conclusions.

4.1.1 Event selection

The results discussed below arise from the analysis of the most performing ALICE reconstruction pass of the data collected during the LHC $Pb-Pb$ run of December 2011. The complete list is made up of events belonging to a specific set of 69 runs that passed all the Quality Assurance (QA) tests. From this list, a sub-sample of about 6.5×10^6 events were selected by a dedicated trigger for UPCs, corresponding to an observed integrated luminosity of about 23 μb^{-1}, as it will be explained afterwards.

Trigger and luminosity

In Chapter 1, it was shown how ultra-peripheral events are characterized by a well-defined event topology: the vector mesons are produced with a very low momentum in the transverse plane.

Their decay implies a back-to-back track configuration, with no further tracks due to the absence of hadronic interactions. In practice, ultra-peripheral events are detectable requiring two only good tracks in an otherwise empty detector. This peculiar event topology is valid whether for the research of the J/ψ or the surrounding di-lepton pairs and it has determined the trigger conditions. Indeed, the data sample for the mid-rapidity analysis was collected with a dedicated barrel ultra-peripheral collision trigger (BUPC) in which a topological constrain was applied.

The BUPC trigger was implemented starting from the collection of the L0 inputs of the SPD, TOF and V0s detectors. In particular, the following conditions were demanded:

0SM2 from SPD: minimum bias trigger with at least two fired Fast-OR chips in the outer layer;

0OUP from TOF: a number N^{OR} of fired pad-OR [96] is in the range $2 \leq N^{OR} \leq 6$, with at least two of them with a difference in azimuth, $\Delta\Phi$, in the range $150^\circ \leq \Delta\Phi \leq 180^\circ$. The angular window, in which the two tracks are triggered, was optimized by using a Monte Carlo simulation [3];

Veto from V0s: no hits in the V0 detectors both from A side and C side, to assure a first online rejection of hadronic events.

In summary, the barrel ultra-peripheral collision trigger fired every time the condition among the L0 inputs,

$$BUPC \quad = \quad !V0A \quad \& \quad !V0C \quad \& \quad 0SM2 \quad \& \quad 0OUP, \tag{4.1}$$

was fulfilled, obtaining in this way a sample of 6,507,629 events to analyse offline. To guarantee a proper bandwidth to other triggers, the trigger rate of BUPC needed a downscaling of a factor f_{DS}. This request is automatically fulfilled when taking into account the overall DAQ dead time (see Par. 2.3).

The determination of the effective integrated luminosity observed by BUPC required a correction dependent on the relative dead-time with respect other trigger classes usually employed for the estimation of this quantity[1]. The integrated luminosity, indeed, was measured using a trigger for the most central hadronic $Pb-Pb$ collisions. The cross section for this process was obtained with a van der Meer scan [98], giving a cross section $\sigma = 4.10^{+0.22}_{-0.13}(sys)$ b [99]. This gives an integrated luminosity for the BUPC trigger sample, corrected for trigger live time, of $L_{int} = 23.0^{+0.7}_{-1.2}\mu\text{b}^{-1}$. An alternative method based on using neutrons detected in the two ZDCs was also used. The ZDC trigger condition required a signal in at least one of the two calorimeters, thus selecting single electromagnetic dissociation (EMD) as well as hadronic interactions. The cross section for this trigger was also measured with a van der Meer scan, giving a cross section $\sigma = 371.4 \pm 0.6(sta)^{+24}_{-19}(sys)$ b [100]. The integrated luminosity obtained for the BUPC by this method is consistent with the one quoted above within 3% (see Tab. 4.6).

Offline selection cuts

The triggered and reconstructed events that passed all the quality assurance standard checks were processed in the offline physics analysis. In order to properly define events with two only tracks in an empty detector, a detailed study on the definition of track itself and the detector emptiness was performed with a scanning of a sample of event displays (Fig. 4.1), the study of the average number of track clusters and, finally, the monitoring of the detector noise in

[1] An extensive study concerning how this measure was performed can be found in [97]

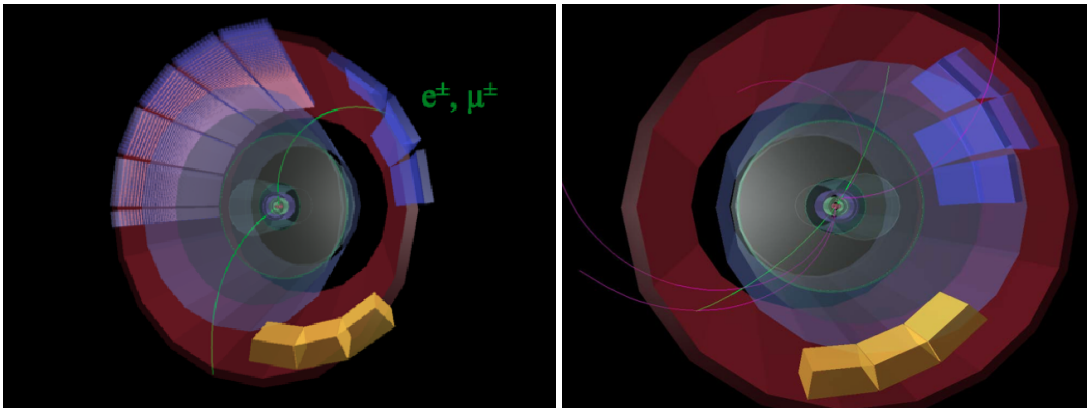

Figure 4.1 Example of two AliRoot event displays of UPC candidates triggered by BUPC. On the left the candidate has been accepted by the offline analysis, while the event on the right has been rejected when applying the analysis cuts.

the fully empty events (triggered by a dedicated system). This step is mandatory since the two tracks originated from the decay of the vector mesons or the $\gamma\gamma$ interactions travel throughout the detector where which cosmic rays, the signal associated to particles of a previous interactions, kink particles - mostly secondary electrons derived from the scattering of the primary particles with the material budget - may influence the search of the genuine signal. The analysis converged into an official set of cuts that optimize the event-tagging:

(i) a number of reconstructed tracks $1 \leq N_{TRK} \leq 10$, where a track is defined with loose criteria: more than 50% of findable clusters in the TPC fiducial volume and at least 20 TPC clusters, matching with those found in the ITS;

(ii) a reconstructed primary vertex using the global track information, otherwise if not possible, by mean of the SPD-tracklet only information ;

(iii) only two good tracks passing tighter quality cuts: at least 70 TPC clusters, at least 1 SPD cluster and rejection of tracks with a kink. The tracks extrapolated to the reconstructed vertex should have a distance of closest approach (DCA) in the longitudinal beam direction $DCA_L \leq 2$ cm, and $DCA_T \leq 0.0182 + 0.0350/p_{\mathrm{T}}^{1.01}$ cm in the plane orthogonal to the beam direction, where p_{T} is in (GeV$/c$);

(iv) at least one of the two good tracks selected in (iii) with $p_{\mathrm{T}} \geq 1\mathrm{GeV}/c$; this cut reduces the background while it does not affect the genuine leptons from J/ψ decay;

(v) The V0 trigger required no signal within a time window of 25 ns around the collision time in any of the scintillator tiles of both A and C sides. The size of the trigger windows are limited by the design of the V0 front-end electronics which is operated at the frequency of the LHC clock, *i.e.* 40 MHz. In the offline analysis the event selection criteria consisted in an absence of a reconstructed signal in any of the V0 scintillator tiles. The time windows in the offline analysis are enlarged to 40 ns and 60 ns around the collision time in V0-A and V0-C, respectively, and were chosen in order to maximize the vetoing efficiency;

(vi) the dE/dx for the two tracks is compatible with that of electrons or muons;

(vii) the two tracks have same or opposite charges, depending on the analysis;

(viii) invariant mass $2.2 < M_{inv} < 6$ GeV$/c^2$.

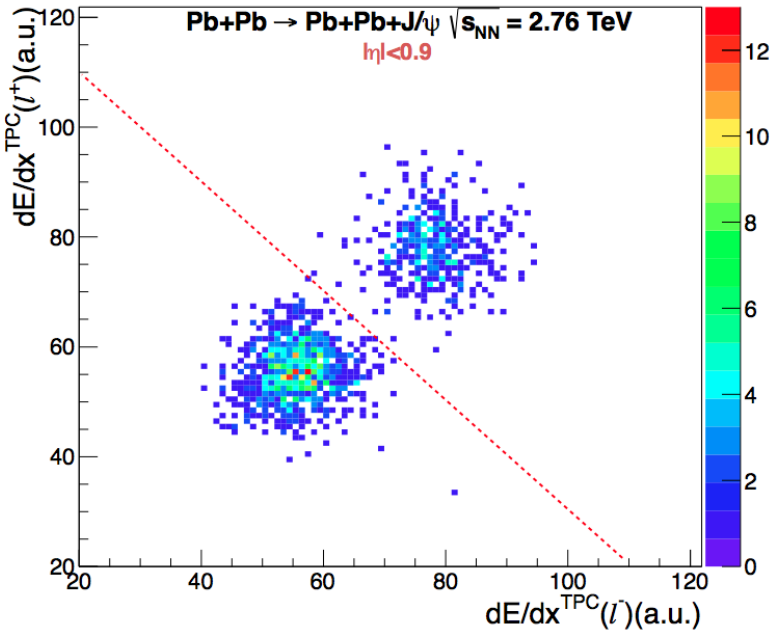

Figure 4.2 Energy loss of the positive lepton versus the negative one, as measured by the TPC for J/ψ candidates from ultra-peripheral $Pb-Pb$ collisions at $\sqrt{s_{NN}} = 2.76$ TeV in the invariant mass range $2.8 < M_{inv} < 3.2$ GeV/c^2 and $-0.9 < \eta < 0.9$. Muon pairs and electron pairs are clearly separated, with the latter showing higher dE/dx values.

Fig. 4.2 shows the TPC dE/dx of the positive lepton candidate as a function of the dE/dx of the negative lepton candidate, for J/ψ candidates in the invariant mass range $2.8 < M_{inv} < 3.2$ GeV/c^2. It is worth noting that the TPC resolution does not allow to distinguish between muons and charged pions, causing an increase of the background. The e/μ separation was obtained by using two methods: *(a)* a sharp cut on Fig. 4.2, where all the particles beyond the dotted line are considered as electrons, and *(b)* using the average of the electron (muon) dE/dx and considering as electrons (muons) the particles within 3 sigma. The difference between the two methods was used as an estimate of the systematic error (see Tab. 4.6). To evaluate the quality of the PID with the TPC, an independent test on the electron and muon separation was applied to those tracks crossing the EMCAL. For each track, the ratio E/p between the energy released in the EMCAL and the reconstructed momentum has been evaluated; electrons lose their total energy in the shower generated in the EMCAL giving a value $E/p \sim 1$, while minimum ionizing particles lose only a small fraction of their energy in the EMCAL; in this case the measured E/p peaks in the region $0.1-0.2$, in good agreement with the expectation (Fig. 4.3).

To extract the coherent and incoherent cross sections, a cut on the transverse momentum of the lepton pairs was added to the previous list, obtaining in this way two separated sub-samples. The p_{T} cut is channel dependent, since muons and electrons interact differently with the detector material budget. The sample enriched with coherent events was selected by applying a cut $p_{\mathrm{T}} < 200$ MeV/c for di-muons ($p_{\mathrm{T}} < 300$ MeV/c for di-electrons). As described in Chapter 1, photoproduction of vector mesons can occur in interactions where additional photons are exchanged, leading to the break up of the nucleus. Since the energies of these photons are low, only a few neutrons are emitted when the nuclei break up. This process is hidden by the more probable breaking up of nuclei in incoherent interactions, where the impinging photon resolves and interacts only with the single nucleon. Up to the present, the exact upper limit on the number of emitted neutrons in coherent processes is not known, but according to Monte Carlo

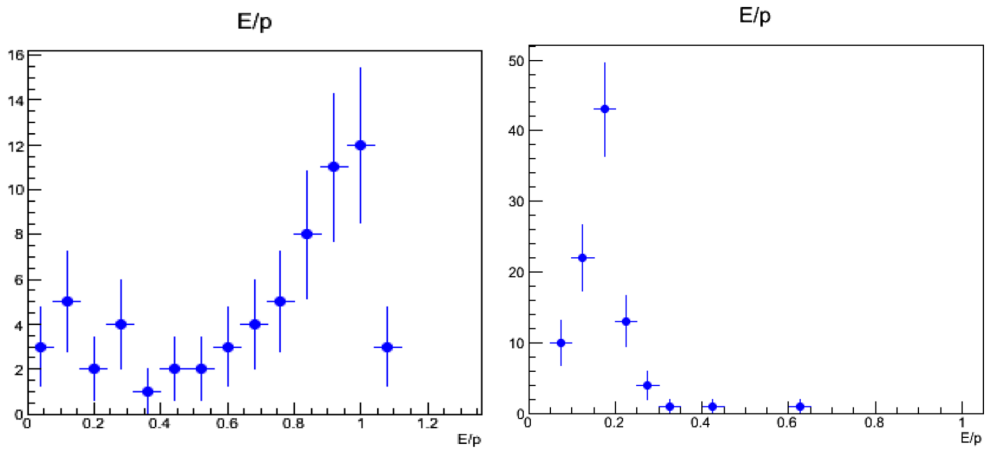

Figure 4.3 For those particles with an associated energy deposit on the EMCAL the ratio E/p, where E is the released energy and p is the track momentum, was evaluated. Electrons lose their total energy in the shower generated giving a value $E/p \sim 1$ *(left)*, while muons lose only a small fraction of their energy in the EMCAL, around $0.1-0.2()$ *(right)*.

Selection	Number of remaining events
Triggered events	6,507,692
$1 \leq N_{TRK} \leq 10$	2,311,056
Primary vertex	1,972,231
Two reconstructed tracks	436,720
$\max(p_{\mathrm{T}}^1, p_{\mathrm{T}}^2) > 1\mathrm{GeV}/c$	46,324
V0 offline	46,183
dE/dx consistent with electron (muon)	45,518
Opposite sign track	31,529
$2.2 < M_{inv} < 6.0\ \mathrm{GeV}/c^2$	4,542
coherent final sample	2047
incoherent final sample	2026

Table 4.1 Summary of the applied data cuts [1].

simulations a cut on the neutron ZDC signal corresponding to less than 6 neutrons on each side was found to be a good solution to avoid a significant loss of signal. It resulted in 20% of the cases in which coherent photoproduction was combined with nuclear fragmentation. The ZDC cut reduces the statistics by 2.5%, which is considered as a source of systematic error $^{+2.5\%}_{-0\%}$ (see Tab. 4.6).

In Tab. 4.1 the effect of these cuts on the statistics is listed. After having applied the whole offline selection, 746 di-electron and 1301 di-muon coherent lepton-pair candidates remain. The second sample, enriched with incoherent events by requiring only the cut $p_{\mathrm{T}} > 200\ \mathrm{MeV}/c$ on di-muons ($p_{\mathrm{T}} > 300\ \mathrm{MeV}/c$ on di-electrons), is composed of 278 electron and 1748 muon event candidates.

Acceptance and efficiency correction

To measure properly the photproduction cross section from the previous filtered data, the obtained yields were corrected to take into account the effects due to the detector acceptance and

efficiency, namely $(Acc \times \varepsilon)$. This correction factor sums up a wide set of contributions like the geometrical area observed by the detector, the sensible effective area devoted to the detection, the detection efficiency, the track-algorithm reconstruction efficiency and the BUPC trigger efficiency. Usually, this correction is parametrized as a function of a kinematic variable like the rapidity, the transverse momentum or the mass of the vector meson. The tiny variations predicted at mid-rapidity for the differential photoproduction ([3]) and the narrow peak of the J/ψ resonance allowed to neglect a rapidity dependence of $(Acc \times \varepsilon)$ around the resonance mass value. The corrections can simply be expressed as a function of the physical process of J/ψ production (coherent and incoherent) or the mass region of the photoproduced di-lepton pairs, namely "low" before the resonance peak, "high" afterwards (see Sec. 4.2).

To calculate $(Acc \times \varepsilon)$, different samples of coherent and incoherent J/ψ events were simulated with StarLight ([54]), whose operating principle was mentioned in Par. 2.4.1. A separate simulation was performed for each run, in order to take into account the slight variations in run conditions during the data taking. The product of the acceptance and efficiency corrections $(Acc \times \varepsilon)_{J/\psi}$ was calculated as

$$(Acc \times \varepsilon)_{J/\psi} = \frac{\text{number of generated events satisfying the cuts}}{\text{number of generated events with the } J/\psi \text{ in } |y| < 0.9}, \tag{4.2}$$

where the cuts are reported in Tab. 4.1. The average values for the combined acceptance and efficiency for $J/\psi \rightarrow e^+e^-(\mu^+\mu^-)$ were found to be $2.71(4.57)\%$ and $1.8(3.19)\%$ for coherent and incoherent interactions, respectively.

As anticipated before, StarLight model predicts a weak rapidity dependence of the J/ψ cross section, of about 10%, over the rapidity interval $y = \pm 0.9$. In order to evaluate the systematic error on the acceptance coming from the generator choice, a flat dependence of $d\sigma_{J/\psi}/dy$ was used in the same rapidity bin, as predicted by other models (see Fig. **??**). The relative differences in $(Acc \times \varepsilon)$ between the methods were $2.5(1.0)\%$ for coherent electrons (muons), and $6.5(3.5)\%$ for incoherent electrons (muons), and are taken into account in the systematic error calculation.

An important element entering the expression of the $(Acc \times \varepsilon)$ factor is the the BUPC trigger efficiency, ε_T^{BUPC}. Its value can be written as the product of the efficiencies of single triggers:

$$\varepsilon_T^{BUPC} = \varepsilon_T^{SPD} \times \varepsilon_T^{V0s} \times \varepsilon_T^{TOF}. \tag{4.3}$$

While the efficiency of the SPD MB trigger was known from other ALICE more standard analysis ($\sim 95\%$, [101]), the other two efficiencies were investigated to better understand their behaviour at this low particle multiplicity.

As described in reference [95], during the 2011 $Pb-Pb$ run the V0 detector was optimized for the selection of hadronic $Pb-Pb$ collisions, with a threshold corresponding to an energy deposit above a single minimum ionizing particle. Since the V0 was used as a veto in the BUPC trigger, this setting could lead to an inefficiency in background rejection. In about 30% of the 2011 BUPC data taking sample, the FMDs were read out too. Since these detectors cover a pseudorapidity interval similar to that of the V0s, their information was used, offline, to check for possible inefficiencies in the V0 data. No hits in the FMD detector for the selected BUPC events were found, confirming that the V0 inefficiency is very small.

At this point, the knowledge of the BUPC efficiency is strictly related to the knowledge of the TOF low-multiplicity topological trigger one. The latter was evaluated in two independent ways, with both Monte Carlo and real data informations. Using the StarLight sample, a check on the L0 input by TOF was performed for each event passing the offline selections. The weakness of this approach stands on the implicit confidence one assumes with respect to the results of the

AliRoot detector simulation. An alternative study was performed in a stand-alone ZDC trigger run, in which data from electromagnetic dissociation were collected. In this case, the event multiplicity at mid-rapidity is similar to the UPC's one; the offline check on the TOF L0 input, for selected events passing the analysis cuts, revealed an agreement with the Monte Carlo results within $^{+3.8\%}_{-9.0\%}$ (see Tab. 4.6).

4.1.2 Coherent and Incoherent J/ψ cross section

Fit of the invariant mass spectra

Sample	Coherent enriched $J/\psi \to \mu^+\mu^-$	Coherent enriched $J/\psi \to e^+e^-$	Incoherent enriched $J/\psi \to \mu^+\mu^-$	Incoherent enriched $J/\psi \to e^+e^-$	$\gamma\gamma \to e^+e^-$ (low)	$\gamma\gamma \to e^+e^-$ (high)
Yield	291 ± 18(sta) ± 4(sys)	265 ± 40(sta) ± 12(sys)	91 ± 15(sta) $^{+7}_{-5}$(sys)	61 ± 14(sta) $^{+16}_{-7}$(sys)	186 ± 13(sta) ± 12(sys)	93 ± 10(sta) ± 6(sys)
Mass (GeV/c^2)	3.096 ± 0.002	3.092 ± 0.036	3.085 ± 0.007	3.080 ± 0.007	-	-
σ (MeV/c^2)	25 ± 1.1	25.0 ± 1.9	33 ± 6	25.0 ± 1.4	-	-
$Acc \times \varepsilon(\%)$	4.57	2.71	3.19	1.8	5.6	4.73
LS pairs	3	0	53	8	0	0
OS pairs	365	514	178	143	186	93
f_D	$0.1^{+0.05}_{-0.06}$	$0.1^{+0.05}_{-0.06}$	0.095 ± 0.055	0.11 ± 0.07	-	-
f_I	0.044 ± 0.014	0.15 ± 0.02	-	-	-	-
f_C	-	-	0.03 ± 0.03	0.47 ± 0.09	-	-
$\lambda_{\gamma\gamma}$(GeV$^{-1}c^2$)	-	-	-	-	-1.55 ± 0.88	-0.73 ± 0.18

Table 4.2 Summary of the main experimental results obtained in the J/ψ and $\gamma\gamma$ analysis and of the most relevant correction parameters applied [1].

Fig. 4.4 shows the invariant mass distribution for $2.2 < M_{inv} < 6.0$ GeV/c^2 for opposite-sign (OS) and like-sign (LS) electron and muon pairs. A J/ψ peak is clearly visible in the four spectra, on top of a continuum coming from $\gamma\gamma \to e^+e^-(\mu^+\mu^-)$ for the coherent enriched sample. The continuum for the incoherent enriched sample for the muon channel (bottom, left) is likely to come from misidentified $\pi^+\pi^-$ pairs, as the energy loss in the TPC is approximatively the same. To extract the J/ψ yield, the number of OS events in the interval $2.2 < M_{inv} < 3.2$ GeV/c^2 for electrons and $3.0 < Minv < 3.2$ GeV/c^2 for muons were considered, due to the different shape of the peak signal. In the mass intervals quoted above, 0 (3) LS electron(muon)-pairs were found for coherent enriched events, while 8 (53) LS pairs were found for incoherent enriched events. The corresponding number of OS pairs was 514 (365) for coherent enriched sample and 143 (178) for incoherent enriched events. Further details that will be explained in the following can be found in Tab. 4.2.

As expected from the behaviour of particles passing throughout the material budget, the J/ψ invariant mass peak reconstructed in the electron channel is broadened towards lower values with respect that one obtained in the muon channel. This has been taken into account in the fit procedure to extract the J/ψ yield. The fit function parametrized the di-lepton invariant mass spectrum with an exponential function, of slope parameter $\lambda_{\gamma\gamma}$, to describe the underlying continuum, and a Crystal Ball function to extract the J/ψ signal. The Crystal Ball function [102] is a probability density function commonly used to model various lossy processes in high-energy physics. It consists of a gaussian core portion and a power-law low-end tail, below a certain threshold. In this analysis, the Crystal Ball function tail parameters (α_{CB} and n) were left free

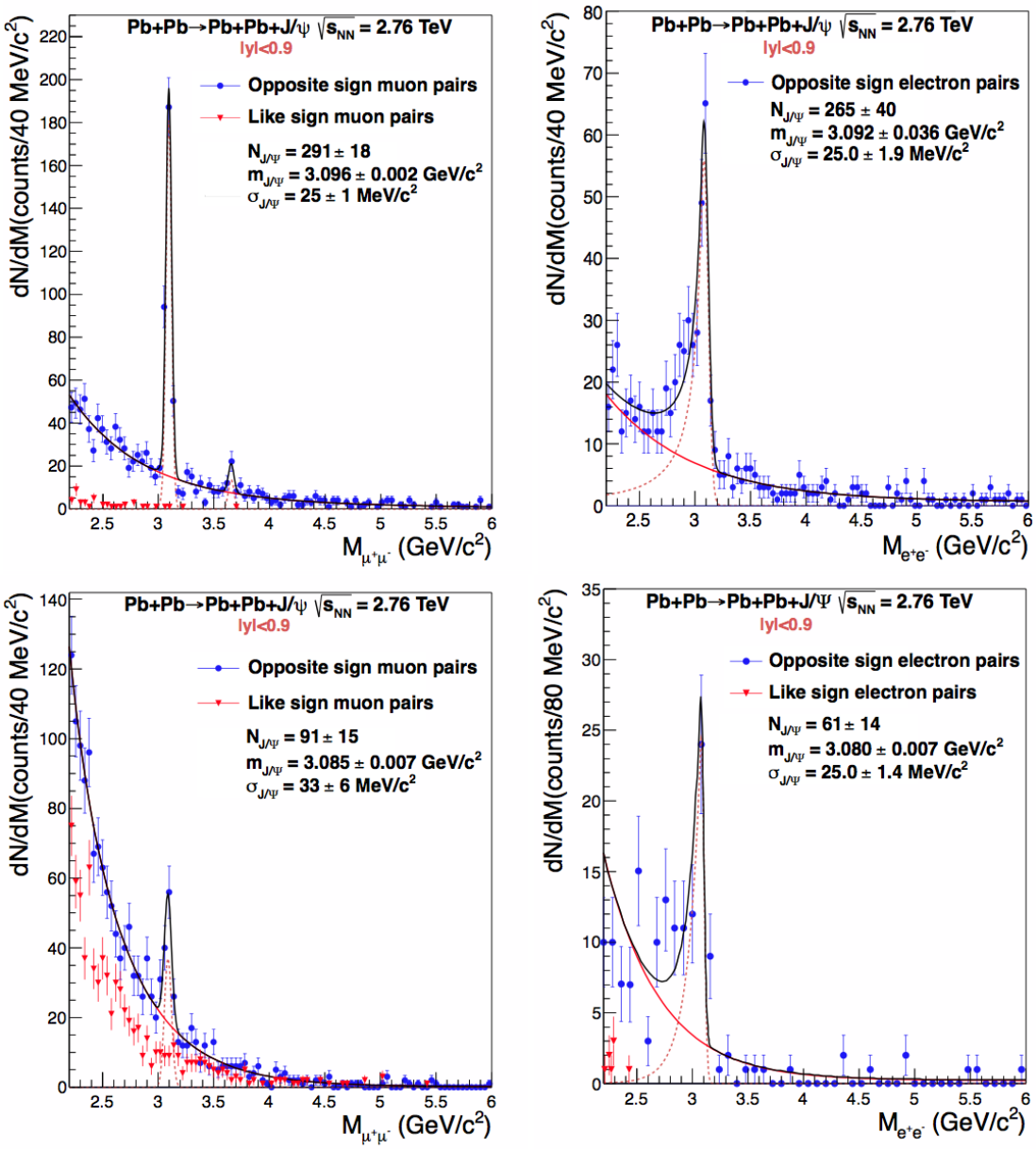

Figure 4.4 Invariant mass distributions for ultra-peripheral $Pb-Pb$ collisions at $\sqrt{s_{NN}} = 2.76$ TeV and and $-0.9 < y < 0.9$ for events satisfying the event selection in Tab. 4.1, in the invariant mass range $2.2 < M_{inv} < 6$ GeV$/c^2$, as reported in [1]. Coherent enriched sample (top) and incoherent enriched sample (bottom) for muons (left) and electrons (right). Blue (red) circles (triangles) are opposite-sign (like-sign) pairs. For like-sign pair the penultimate cut in Tab. 4.1 is replaced by the request of a same-sign pair. No LS events were found for coherent di-electron events.

for the coherent enriched sample, giving a good agreement with those obtained by fitting the simulated data, and were fixed to values obtained from simulations for the incoherent enriched one. When fitting the incoherent di-muons a polynomial was also used to take into account the the combinatorial background, constrained by the LS pair spectrum. In summary, the fit gave the following results.

Fit of the coherent enriched sample. The yield obtained for the coherent enriched sample (Fig. 4.4 top) is $N_{yield} = 265 \pm 40(\text{sta}) \pm 12(\text{sys})$ for the $J/\psi \rightarrow e^+e^-$ channel and $N_{yield} = 291 \pm 18(\text{sta}) \pm 4(\text{sys})$ for the $J/\psi \rightarrow \mu^+\mu^-$ channel. The systematic error on the yield is obtained by varying the bin size and by replacing the exponential with a polynomial to fit the $\gamma\gamma$ process. In addition, the Crystal Ball function parameters are obtained by fitting a simulated sample made of J/ψ and $\gamma\gamma$ event cocktail and then used to fit the coherent enriched data sample too. The difference in the yield obtained with the two Crystal Ball fit procedures is included in the systematic error. As a result a $^{+7\%}_{-6\%}$ and $^{+6\%}_{-5\%}$ systematic error on the signal extraction for coherent electrons and muons was obtained, respectively. For the coherent enriched sample, the central mass (standard deviation) value from the fit is 3.092 ± 0.036 GeV$/c^2$ (25.0 ± 1.9 MeV$/c^2$) for the electron channel and 3.096 ± 0.002 GeV$/c^2$ (25 ± 1.1 MeV$/c^2$) for the muon channel, in good agreement with the known value of the J/ψ mass and compatible with the absolute calibration accuracy of the barrel. The exponential slope parameter, $\lambda_{\gamma\gamma}$, of the continuum for the coherent enriched sample is computed at $2.2 < M_{inv} < 2.6$ GeV$/c^2$ (low) and $3.7 < M_{inv} < 10$ GeV$/c^2$ (high) for electrons with $0.9 < \eta_{1,2} < 0.9$, giving -1.55 ± 0.88 GeV$^{-1}c^2$ and -0.73 ± 0.18 GeV$^{-1}c^2$, in good agreement with the corresponding Monte Carlo expectation, -1.07 ± 0.16 GeV$^{-1}c^2$ and -0.81 ± 0.01 GeV$^{-1}c^2$, respectively. This is an additional indication that there is no important background in the invariant mass and p_{T}range considered.

Fit of the incoherent enriched sample. For the incoherent sample, the central mass (standard deviation) value from the fit is 3.080 ± 0.007 GeV$/c^2$ (25 ± 1.4 MeV$/c^2$) for the electron channel and 3.085 ± 0.007 GeV$/c^2$ (33 ± 6 MeV$/c^2$) for the muon channel. For the incoherent enriched sample the obtained yield is (Fig. 4.4 bottom), $N_{yield} = 61 \pm 14(\text{sta})$ $^{+16}_{-7}(\text{sys})$ for the $J/\psi \rightarrow e^+e^-$ channel and $N_{yield} = 91 \pm 15(\text{stat})$ $^{+7}_{-5}(\text{sys})$ for the $J/\psi \rightarrow \mu^+\mu^-$ channel.

Feed down corrections to coherent and incoherent photoproduction

The top-left plot of Fig. 4.4 depicts a small peak centred at the value of ψ' mass. The photoproduction of this state indeed, must be taken into account in order to evaluate properly the signal cross sections: within the J/ψ signal, a feed-down contribution is hidden from the decay $\psi' \rightarrow J/\psi +$ anything. This contribution is moreover dependent by the polarization P of these feed-down J/ψ s. In ultra-peripheral J/ψ photoproduction, transverse polarization is expected from helicity conservation for a quasi-real photon. In the standard calculations it is therefore assumed that the J/ψ is transversely polarized, as found by previous experiments [103]. On the contrary, the polarization of J/ψ s coming from ψ' decays cannot easily be predicted, since the polarization of the latter can be shared between the J/ψ and the other daughters in different ways. The possible values of the J/ψ polarization, in the helicity frame, ranges among the following extreme values:

(i) full longitudinal L, $\lambda = -1$;

(ii) no polarization NP, $\lambda = 0$;

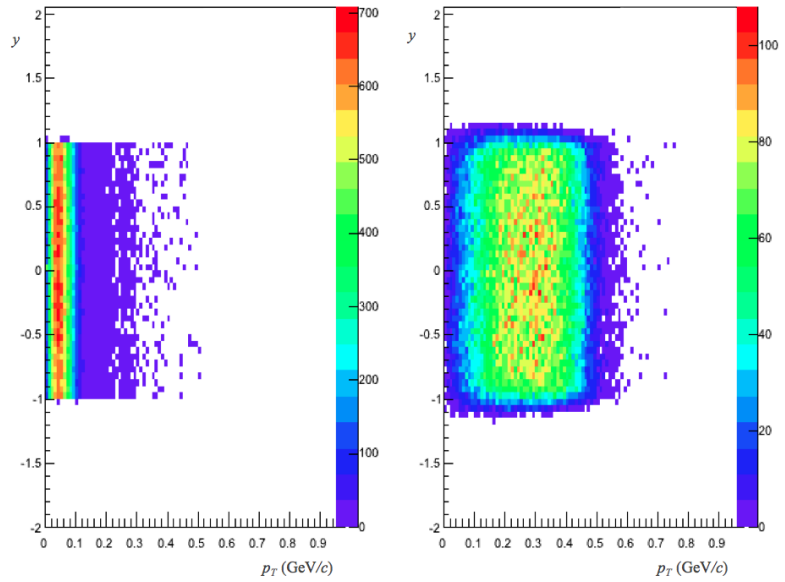

Figure 4.5 Rapidity as a function of transverse momentum for a sample of ψ' generated with StarLight *(left)* and kinematics of the J/ψ coming from the decay $\psi' \to J/\psi +$ anything, obtained with PYTHIA *(right)*. In this example, coherent ψ' were generated.

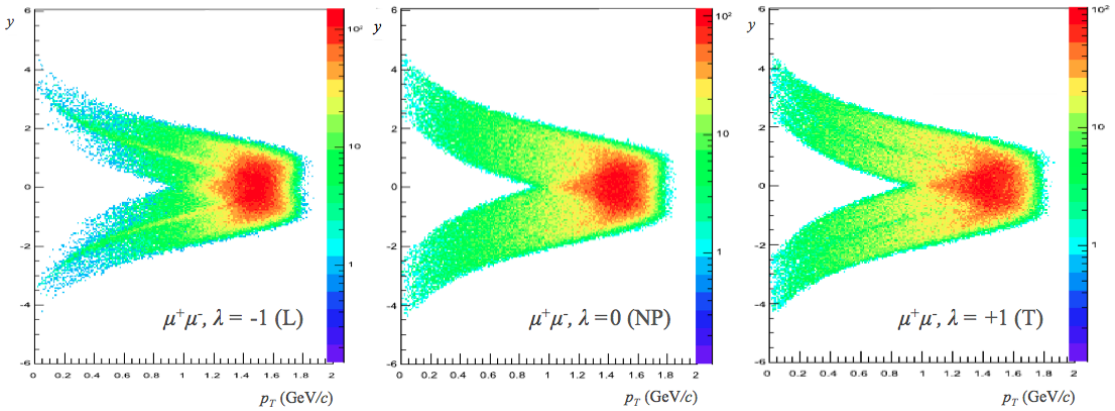

Figure 4.6 Simulation of the only kinematics of the J/ψ di-lepton decay assuming longitudinal (L), transverse (T) or no polarization (NP). In this example, the J/ψ coming from coherent ψ' decay into the muon channel.

(iii) full transverse T, $\lambda = +1$.

The J/ψ fraction coming from ψ' decay for a given polarization, f_D^P, can be written as:

$$f_D^P = \frac{\sigma_{\psi'} \cdot BR(\psi' \to J/\psi \ + \text{anything}) \cdot (Acc \times \varepsilon)^P_{\psi' \to J/\psi}}{\sigma_{J/\psi} \cdot (Acc \times \varepsilon)_{J/\psi}}, \tag{4.4}$$

where all the contributors are evaluated at mid-rapidity. This expression is model dependent: in Starlight, the ratio $\sigma_{\psi'}/\sigma_{J/\psi}$ is predicted to be 1.26 mb / 8.23 mb (0.58 mb / 3.40 mb) for coherent (incoherent) photoproduction. In the case of pQCD inspired models like [104], the ratio is 0.087 for the coherent case while it has been rescaled for the incoherent one since no theoretical predictions are available.

Dedicated Monte Carlo simulations, anchored to the "golden run" 168311, allowed the estimate of the $(Acc \times \varepsilon)$ factor as a function of the J/ψ polarization and channel of reconstruction. The simulations were performed starting from two samples of coherently and incoherently produced ψ's with StarLight, using PYTHIA [80] to simulate their decay into J/ψ + anything (Fig. 4.5); subsequently, the polarized decay of J/ψ s into leptons was obtained with a specific AliRoot class, *AliDecayerPolarized*, implemented in previous analysis to study the effects of the polarization in the J/ψ decays at forward rapidity. The results are depicted in Fig. 4.6 in the case of di-muon channel of J/ψ s from coherently produced ψ's. In this work, more in general, all the cases have been treated. Once the kinematics of the final state (di-lepton from J/ψ + anything) was externally generated, the detector response has been simulated within the AliRoot framework, as explained in Chapter 2. The same offline cuts of the signal analysis were applied to select these resonances in order to evaluate the variations of $(Acc \times \varepsilon)$, and eventually of the feed-down. Tab. 4.3 shows the theoretical predictions for f_D given by Eq.4.4 within the assumptions of StarLight, while in Tab. 4.4 the same predictions are derived with the pQCD model [104]. When coherent ψ's are considered, the theoretical estimation for f_D ranges from 4.4% to 11.8% for electrons and 4.3% to 14.7% for muons, while with incoherent ψ's it spreads from 3.9% to 15.1% for muons and from 3.8% to 18.1% for electrons.

	Coherent ψ'		Incoherent ψ'	
J/ψ polarization	$\mu^+\mu^-$	e^+e^-	$\mu^+\mu^-$	e^+e^-
$\lambda = -1$ (L)	0.147	0.118	0.151	0.181
$\lambda = 0$ (NP)	0.109	0.104	0.112	0.084
$\lambda = +1$ (T)	0.096	0.099	0.087	0.102

Table 4.3 Summary of the StarLight predictions for the feed-down as a function of the J/ψ polarization.

	Coherent ψ'		Incoherent ψ'	
J/ψ polarization	$\mu^+\mu^-$	e^+e^-	$\mu^+\mu^-$	e^+e^-
$\lambda = -1$ (L)	0.065	0.052	0.068	0.081
$\lambda = 0$ (NP)	0.048	0.046	0.050	0.038
$\lambda = +1$ (T)	0.043	0.044	0.039	0.046

Table 4.4 Alternative predictions by pQCD model [104] for the feed-down as a function of the J/ψ polarization.

Alternatively, the ratio of coherent yields for ψ' to J/ψ can be extracted from the real data. Owing to the limited statistics, the electron and muon channels were combined to obtain

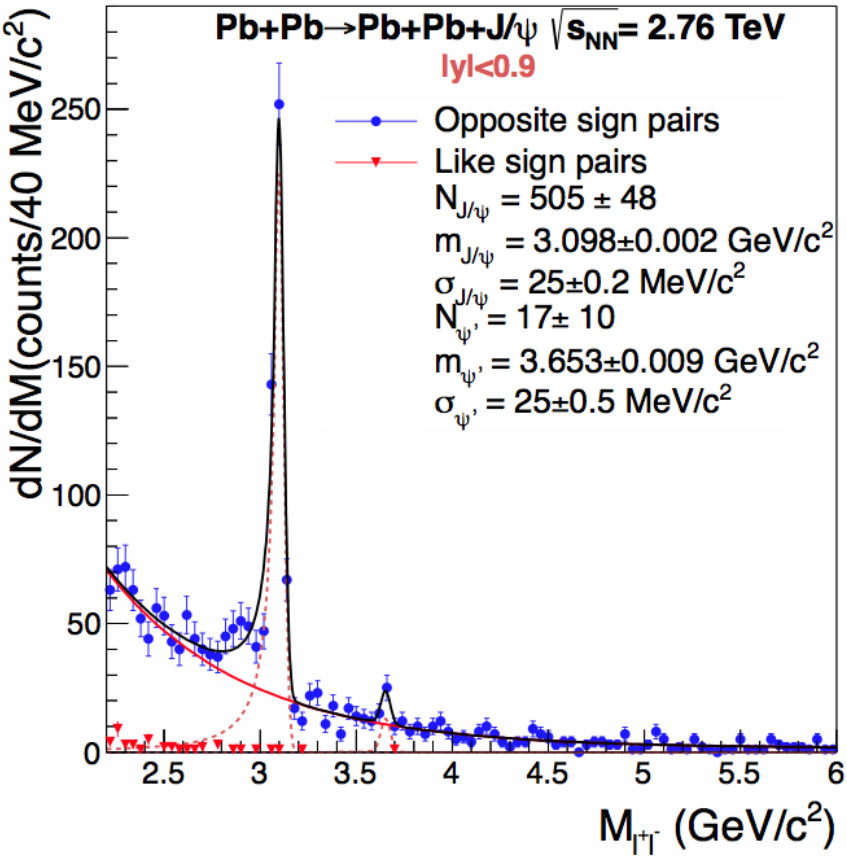

Figure 4.7 Invariant mass distribution for ultra-peripheral $Pb-Pb$ collisions at $\sqrt{s_{NN}} = 2.76$ TeV at $-0.9 < y < 0.9$ for events satisfying the event selection in Tab. 4.1, in the invariant mass interval $2.2 < M_{inv} < 6$ GeV$/c^2$. Coherent di-electron and di-muon candidates are summed together [1].

$N_{\psi'} = 17 \pm 10$ and $N_{J/\psi} = 505 \pm 48$ (see Fig. 4.7). In this case, the fraction f_D, for a given J/ψ polarization P, can be written as:

$$f_D^P = \frac{N_{\psi'} \cdot (Acc \times \varepsilon)^P_{\psi' \to J/\psi} \cdot BR(\psi' \to J/\psi + \text{anything}) \cdot BR(J/\psi \to l^+l^-)}{N_{J/\psi} \cdot (Acc \times \varepsilon)^P_{\psi' \to l^+l^-} \cdot BR(\psi' \to l^+l^-)}. \tag{4.5}$$

The acceptance corrections are again polarization dependent and f_D^P ranges from $15 \pm 9\%$ for longitudinal polarization to $11 \pm 6.5\%$ for transverse polarization.

In conclusion, for the coherent contribution the central value of theoretical and experimental estimates have been used, taking the others as upper and lower limits, *i.e.* $f_D = 0.10^{+0.05}_{-0.06}$; for the incoherent ψ' only the average of the theoretical prediction was assumed, with $f_D = (9.5 \pm 5.5)\%$ for muons and $f_D = (11 \pm 7)\%$ for electrons.

Signal contaminations and transverse momentum spectra

The di-electron (di-muon) p_{T} distribution, integrated over $2.2 < M_{inv} < 3.2$ GeV$/c$, ($3.0 < Minv < 3.2 GeV/c$) is shown in Fig. 4.8 right (left). The clear peak at low p_{T} is mainly due to coherent interactions, while the tail extending out to 1 GeV$/c$ comes from incoherent production. The coherent and incoherent photoproduction p_{T} distributions overlap gradually in a non-negligible way, so that, it is mandatory to define two correction factors, f_C and f_I, that

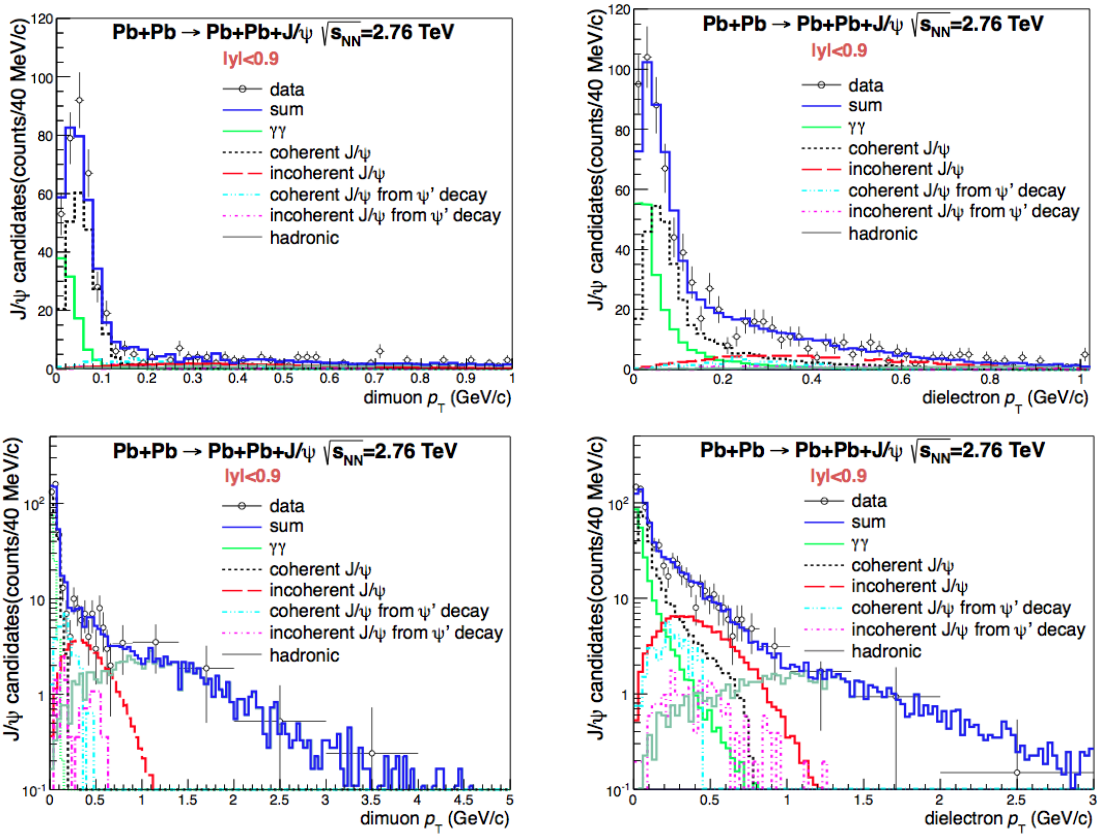

Figure 4.8 Di-muon *(left)* and di-electron *(right)* p_{T} distribution for ultra-peripheral $Pb-Pb$ collisions at $\sqrt{s_{NN}} = 2.76$ TeV and $-0.9 < y < 0.9$ for events satisfying the event selection in the invariant mass interval $3.0 < M_{inv} < 3.2$ GeV$/c^2$ and $2.2 < M_{inv} < 3.2$ GeV$/c^2$ respectively, with the p_{T}-range extended to $p_{\mathrm{T}} < 1$ GeV$/c$ *(top)* and to $p_{\mathrm{T}} < 5$ GeV$/c$ *(bottom)*. The data points are fitted summing six different Monte Carlo templates: coherent J/ψ production *(black)*, incoherent J/ψ production *(red)*, J/ψ from coherent ψ' decay *(light blue)*, J/ψ s from incoherent ψ' decay *(violet)*, $\gamma\gamma$ *(green)*, and J/ψ produced in peripheral hadronic collisions *(grey)*. The solid histogram *(blue)* is the sum [1].

parametrize the contamination of coherent J/ψ s in the incoherent region ($p_{\rm T} > 300$ MeV$/c$ for di-electrons, $p_{\rm T} > 200$ MeV$/c$ for di-muons) and the incoherent contribution in the coherent peak, respectively. These two factors are evaluable by theory considerations, as explained in [1].

An alternative data driven method, to extract an upper limit for f_I and f_C, was the study of the fit to the measured $p_{\rm T}$ distribution. Six different functions were used to describe the $p_{\rm T}$ spectrum:

(i) coherent J/ψ photoproduction;

(ii) incoherent J/ψ photoproduction;

(iii) J/ψ from coherent ψ' decay;

(iv) J/ψ from incoherent ψ' decay;

(v) two-photon production of continuum pairs;

(vi) J/ψ produced in peripheral hadronic collisions.

The shapes for the first five fitting functions (Monte Carlo templates) were provided by Starlight events folded with the detector simulation, while the last contribution was extrapolated by applying the UP-analysis selection criteria of Tab. 4.1 to a $Pb-Pb$ HIJING production at higher centrality enriched with a J/ψ signal from ALICE real data [105]. The relative normalization was left free for coherent and incoherent photoproduction. The contribution from the ψ' was constrained from the estimate above and the two-photon contribution was determined from the fit to the continuum in Fig. 4.4. The hadronic J/ψ s were constrained by the fit to the region $p_{\rm T} > 1.1$ GeV$/c$, where the ultra-peripheral J/ψ contribution is negligible. Tab. 4.2 lists the final adopted values in this analysis for f_C and f_I.

Coherent and incoherent J/ψ cross section

The contributions entering into the calculation of the cross section have been described above. The coherent (incoherent) J/ψ differential cross section is finally given by:

$$\frac{d\sigma_{J/\psi}^{coh(incoh)}}{dy} = \frac{N_{J/\psi}^{coh(incoh)}}{(Acc\times\varepsilon)_{J/\psi}\cdot BR(J/\psi\ \to l^+l^-)\cdot L_{int}\cdot\Delta y}, \tag{4.6}$$

where $\Delta y = 1.8$ is the rapidity interval bin, L_{int} is the integrated luminosity, $BR(J/\psi\ \to l^+l^-)$ is the branching ratio of the J/ψ s into the reconstructed channel and $(Acc\times\varepsilon)_{J/\psi}$ corresponds to the acceptance and efficiency as discussed above. $N_{J/\psi}^{coh(incoh)}$ is the number of coherent (incoherent) J/ψ candidates derived applying the following correction to the yield extracted from the fit to the invariant mass distribution:

$$N_{J/\psi}^{coh(incoh)} = \frac{N_{yield}}{1+f_D+f_{C(I)}}, \tag{4.7}$$

resulting in $N_{J/\psi}^{coh}\ (\mu^+\mu^-) = 255\pm$(sta) $^{+14}_{-13}$(sys), $N_{J/\psi}^{coh}\ (e^+e^-) = 212\pm 32$(sta) $^{+14}_{-13}$(sys), and $N_{J/\psi}^{incoh}(\mu^+\mu^-) = 81\pm 13$(sta) $^{+8}_{-6}$(sys), $N_{J/\psi}^{incoh}(e^+e^-) = 39\pm 9(sta)^{+10}_{-5}$(sys), respectively.

As a result, the differential coherent (incoherent) cross sections obtained in each channel are listed in Tab. 4.5.Since the di-electron and di-muon data are statistically separated samples, they can be combined; their weighted average is listed below.

Coherent differential cross section: $d\sigma^{coh}_{J/\psi}/dy = 2.38^{+0.34}_{-0.24}$(stat+sys) mb.

Incoherent differential cross section: $d\sigma^{incoh}_{J/\psi}/dy = 0.98^{+0.19}_{-0.17}$(stat+sys) mb;

The discussion of these results and the comparison with the available predictions is developed in Sec. 4.3. In addition, the fraction F_n of coherent events with no neutron emission was estimated

Type	$\mu^+\mu^-$	e^+e^-	l^+l^-
$d\sigma^{coh}_{J/\psi}/dy$ (mb)	2.27 ± 0.14(sta) $^{+0.30}_{-0.20}$(sys)	3.19 ± 0.50(sta) $^{+0.45}_{-0.31}$(sys)	$2.38^{+0.34}_{-0.24}$(stat+sys)
$d\sigma^{incoh}_{J/\psi}/dy$ (mb)	1.03 ± 0.17(sta) $^{+0.15}_{-0.12}$(sys)	0.87 ± 0.20(sta) $^{+0.26}_{-0.14}$(sys)	$0.98^{+0.19}_{-0.17}$(stat+sys)

Table 4.5 Differential cross sections for the coherent (incoherent) J/ψ photoproduction in ultra-peripheral $Pb-Pb$ collisions at $\sqrt{s_{NN}} = 2.76$ TeV. The decay channel in which the cross section has been derived is shown, together with the weighted average for the whole di-lepton channel.

by StarLight to be $F_n = 0.68$, while the pQCD inspired model [104] predicts $F_n = 0.76$. Events with neutron emission can be efficiently tagged in ALICE by the ZDC calorimeters, taking advantage of their high efficiency ($> 98\%$). By fitting the di-electron (di-muon) invariant mass spectrum for events with and without neutron emission and with $p_{\rm T} < 300$ MeV$/c$ ($p_{\rm T} < 200$ MeV$/c$), we obtain a fraction 0.70 ± 0.05(sta) in good agreement with the above estimates.

4.1.3 Background and systematics error overall estimate

Tab. 4.6 summarizes the so far presented contributions to the systematic errors took into account in the computation of the cross sections. Moreover, other contributions related to several physical process are hereby explained.

QED pair production

A possible loss of events might come from QED pair production, *i.e.* interactions producing both a J/ψ and a low mass e^+e^- pair (the latter process has a very large cross section), with one of the electrons hitting the V0 detector and thus vetoing the event. This effect was already studied in [95], with a control data sample where no veto at trigger level was applied. As a result, an upper limit on the inefficiency smaller than 2% was found. In the forward rapidity trigger only A-side V0 was used as a veto, and therefore a conservative estimate when the BUPC is taken into account implies a 4% of systematic error for this study.

J/ψ radiative decay

Another possible source of systematic error is the radiative decay $J/\psi \rightarrow e^+e^-\gamma$, neglected by the most commonly used event generators, like those adopted in this analysis. The process, also called internal bremsstrahlung, is computed at the next to leading order and it can occur in the 15% of cases, when considering the J/ψ decay into electrons. In this fraction of events a photon is emitted with an energy $E_\gamma > 100$ MeV [107]. For radiative processes, the reconstructed di-electron invariant mass, $m_{e^+e^-}$, is biased towards smaller values than the nominal J/ψ mass, since the photon contribution is neglected. To estimate the effects of this process for the analysis,

Source	Coherent	Incoherent	$\gamma\gamma$(low)	$\gamma\gamma$(high)
Luminosity	$^{+5\%}_{-3\%}$	$^{+5\%}_{-3\%}$	$^{+5\%}_{-3\%}$	$^{+5\%}_{-3\%}$
Trigger dead time	$\pm(2.5\%)$	$\pm(2.5\%)$	$\pm(2.5\%)$	$\pm(2.5\%)$
Signal extraction	$^{+7\%}_{-6\%}$ $\left(^{+6\%}_{-5\%}\right)$	$^{+26.5\%}_{-12.5\%}$ $\left(^{+9\%}_{-8\%}\right)$	$\pm1\%$	$\pm4\%$
Trigger efficiency	$^{+3.8\%}_{-9.0\%}$	$^{+3.8\%}_{-9.0\%}$	$^{+3.8\%}_{-9.0\%}$	$^{+3.8\%}_{-9.0\%}$
$(Acc \times \varepsilon)$	$\pm2.5\%(\pm1\%)$	$\pm6.5\%(\pm3.5\%)$	$\pm0.3\%$	$\pm0.5\%$
$\gamma\gamma \to e^+e^-$ background	$^{+4\%}_{-0\%}$	$^{+4\%}_{-0\%}$	$^{+4\%}_{-0\%}$	$^{+4\%}_{-0\%}$
e/μ separation	$\pm2\%$	$\pm2\%$	$\pm1.7\%$	$\pm4\%$
Branching ratio	$\pm1\%$	$\pm1\%$	-	-
Neutron number cut	$^{+2.5\%}_{-0\%}$	-	-	-
Hadronic J/ψ	-	$^{+0\%}_{-5\%}$ $\left(^{+0\%}_{-3\%}\right)$		
Total	$^{+14.0\%}_{-9.6\%}$ $\left(^{+13.4\%}_{-8.8\%}\right)$	$^{+29.4\%}_{-16.6\%}$ $\left(^{+14.5\%}_{-11.7\%}\right)$	$^{+10.8\%}_{-7.0\%}$	$^{+12.0\%}_{-8.8\%}$

Table 4.6 Summary of the contributions to the systematic error for the J/ψ and $\gamma\gamma$ cross electrons (muons). The error for the J/ψ signal extraction includes the systematic error in the fit of the invariant mass spectrum and the systematic errors on f_D and f_I (f_C), as described in the text [1].

in particular on the fit and $(Acc \times \varepsilon)$ results, a dedicated simulation was performed, in which the decay of the J/ψ is handled by the EvtGen package [108], and where the final state radiation is described using PHOTOS [109]. In Fig. 4.9 the results of this simulation is depicted: a cocktail with 85% of J/ψ s with a standard di-lepton decay and 15% of them with a radiative one, folded with the detector simulation has been fitted by the Crystal Ball function. Both the resulting CB-parameters as the $(Acc \times \varepsilon)$ correction were found to be not significantly different from the standard values, so no correction were required in this analysis.

Hadronic contaminations

A first contamination due to hadronic interactions comes form J/ψ s originated in very peripheral collisions, $b \approx 2R_{Pb}$, as previously introduced to justify the long tails in the p_{T} spectra (Fig. 4.8). This contribution turned out to be negligible for $p_{\mathrm{T}} \lesssim 200-300$ MeV$/c$, and therefore it is not important for coherent production. For incoherent events this background was evaluated from the p_{T} fit described above and gives a contribution (0.043 ± 0.015) for di-electrons and (0.024 ± 0.017) for di-muons, in the same respective mass intervals taken into account. This has been considered an upper limit since this M_{inv} interval contains J/ψ s and other contributions. These fractions have been included in the systematic errors, as listed in Tab 4.6.

Another hadronic background is originated by mis-identified pions tagged as muons by the TPC: for these two species the energy loss is the same. The combinatorial background can estimated by the LS events and it results to be negligible for coherent J/ψ s and incoherent ones in the electron channel. For incoherent di-muons this background was taken into account by using a polynomial function as described when the fit functions were introduced.

Photoproduced J/ψ in very peripheral collisions

An ultra-peripheral event is defined as an interaction where the impact parameter b is greater than the sum of the radii of the two colliding ions. More in general, photoproduction processes can occur even when $b \lesssim 2R_{Pb}$. It is important to evaluate how many events of this typology

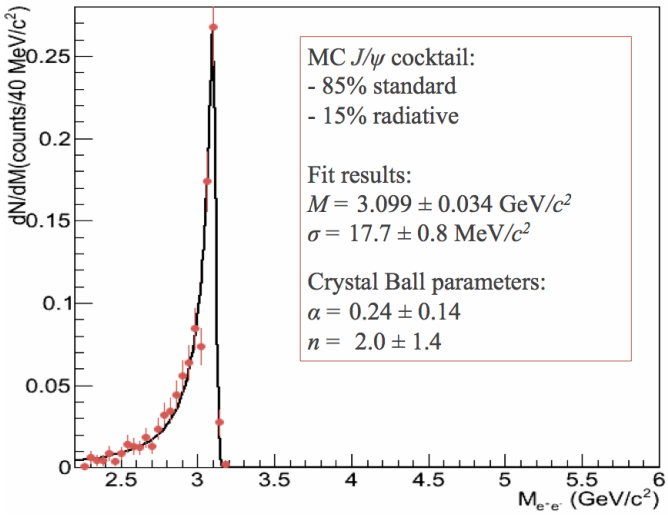

Figure 4.9 Fit to a signal composed by a cocktail enriched with 85% of J/ψ with a standard di-lepton decay and 15% of them with a radiative decay. The simulations have been carried by a specific package as described in the text.

may contaminate the collected data. Since from an analytical point of view the selection cuts are not able to distinguish the two classes of J/ψ photoproduction, an useful estimate of the contamination is given by the analysis of pure minimum bias Monte Carlo $Pb-Pb$ interactions (at very low centrality) passing however both the trigger and the offline selections. The Monte Carlo $Pb-Pb$ sample was generated by HIJING [81];in this analysis 1.67×10^6 events were considered, in the centrality bin $(80-90)\%$ and $(90-100)\%$, where the predicted Starlight cross section is 1.1 mb and 0.7 mb, respectively.

Fig. 4.10 depicts the the impact parameter distribution resulting after imposing the offline analysis cuts (ii, iv, vi, Section 4.1.1) to identify the OS candidates; no BUPC trigger signal was required, obtaining a sample of 12565 events. The survival probability is dramatically reduced when the trigger condition is implemented, as it appears evident in Fig. 4.11, where the mass distribution of OS triggered candidates is plotted assuming the mass of a lepton (muon, in this case). From these results, the fraction of events passing the applied cuts is 0.06% and 0.3% in the two centrality bins. This process therefore gives a negligible contribution to the ultraperipheral cross section.

4.2 Two-photons scattering

The approach illustrated above for the analysis of the di-leptons coming from the J/ψ decay can be easily extended to the analysis of those originated in $\gamma\gamma$ scattering since the final state, for what concerns both the physical signal and the detector answer, is basically the same. This section concentrates on the cross section measurement performed in the $\gamma\gamma\to e^+e^-$ scattering, neglecting the muon channel because of its pion contamination, suggested by the presence of LS events, that could introduce a bias on the results.

The cross section can be written in a similar way to Eq. 4.6:

$$\sigma_{\gamma\gamma}=\frac{N_{\gamma\gamma}}{(Acc\times\varepsilon)_{\gamma\gamma}\cdot L_{int}} \tag{4.8}$$

where $N_{\gamma\gamma}$ was obtained by fitting the continuum in the invariant mass intervals $2.2<M_{inv}<2.6$

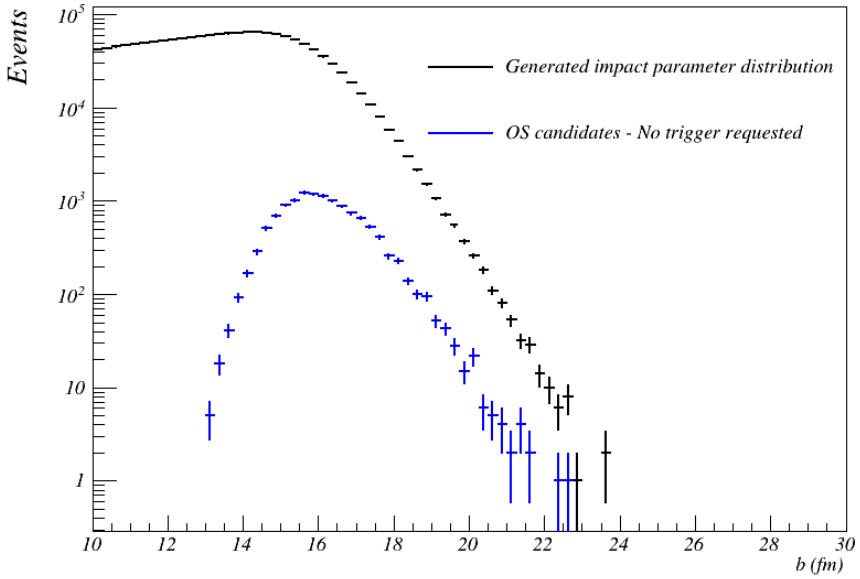

Figure 4.10 Impact parameter distribution (from this work) as generated in the Monte Carlo (black) and after having applied the selections cuts (blue). See the text for further details.

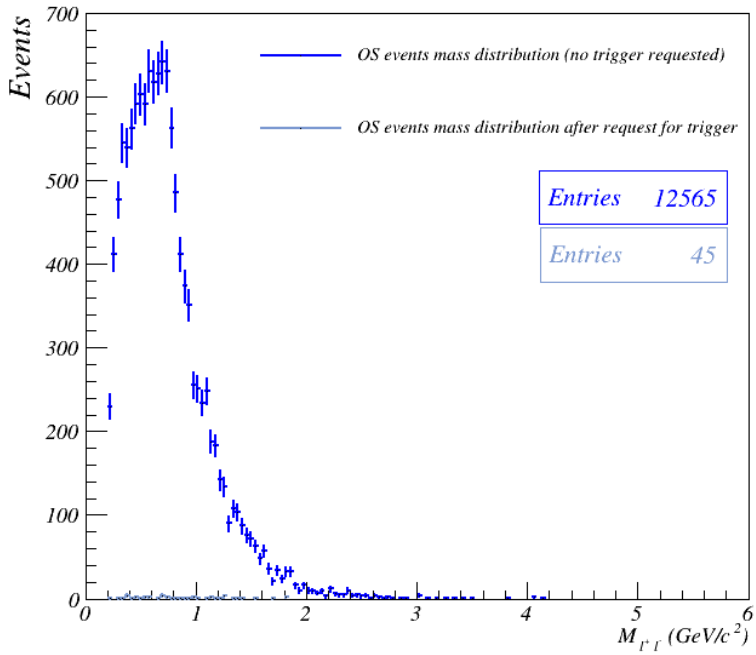

Figure 4.11 The survival probability of events when both the offline cuts and trigger are required is very low. See the text for further details

GeV$/c^2$ ($N_{e^+e^-} = 186 \pm 13$(sta) ± 4(sys)) and $3.7 < M_{inv} < 10$ GeV$/c^2$ ($N_{e^+e^-} = 93 \pm 10$(sta) ± 4(sys)), to avoid contamination from the J/ψ peak. In this analysis the integrated luminosity used was $L_{int} = 21.7^{+0.7}_{1.1}\mu b^{-1}$ and the cut on the track p_T was removed. The acceptance and efficiency correction was similarly computed in dedicated Monte Carlo simulations in which the StarLight generated signal was folded with the detector answer. The two values in relation to the two mass bins are listed in Tab. 4.2.

The cross section in the two mass intervals, computed for di-lepton in the rapidity bin $-0.9 < y < 0.9$ and requiring $-0.9 < \eta_{1,2} < 0.9$ was measured to be:

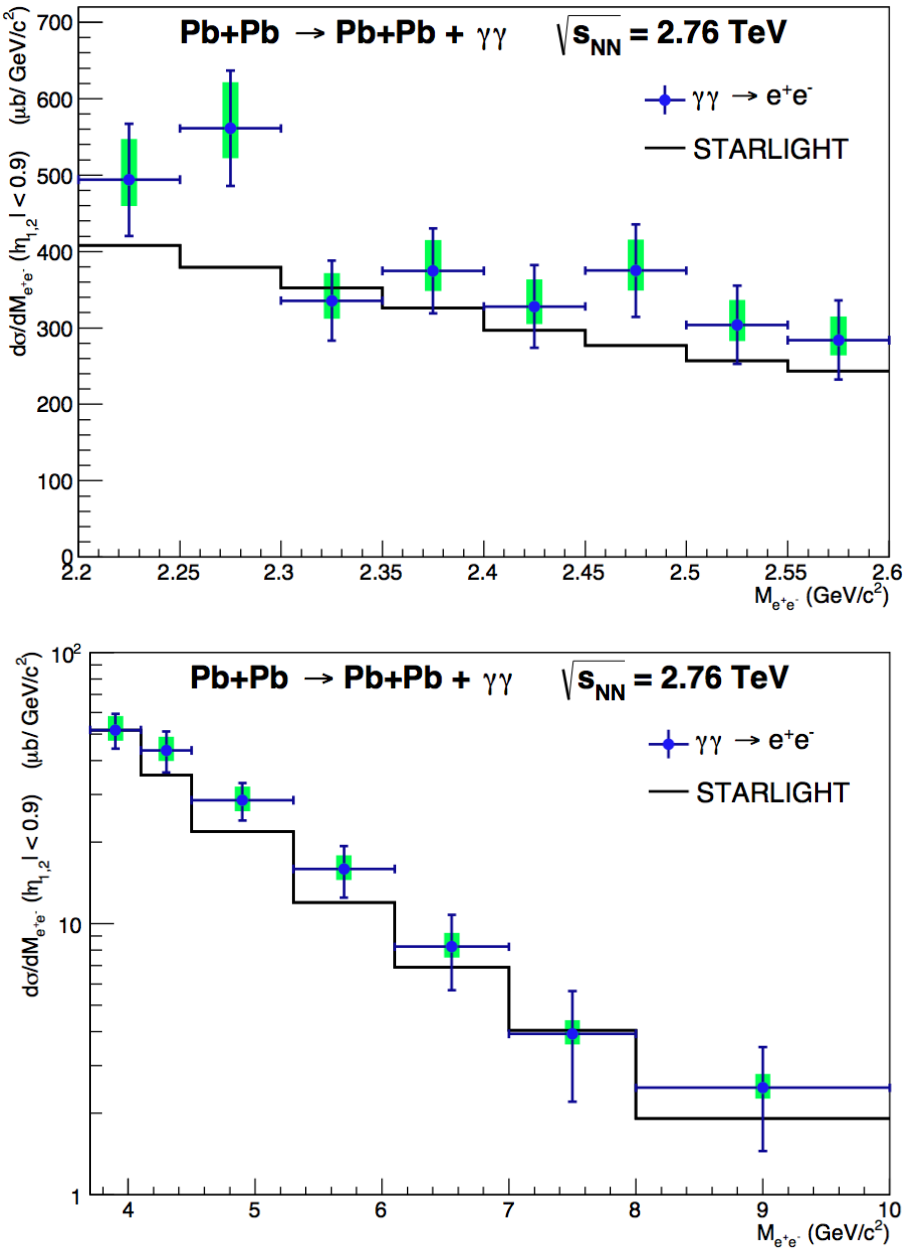

Figure 4.12 $\gamma\gamma \to e^+e^-$ cross section *(blue circles)* for ultra-peripheral $Pb-Pb$ collisions at $\sqrt{s_{NN}} = 2.76$ TeV at $-0.9 < \eta < 0.9$ for events in the invariant mass interval $2.2 < M_{inv} < 2.6$ GeV$/c^2$ *(top)* and $3.7 < M_{inv} < 10$ GeV$/c^2$ interval *(bottom)* compared to StarLight simulation *(black line)*. The blue (green) bars show the statistical (systematic) error, respectively

lower mass interval, $2.2 < M_{inv} < 2.6$ GeV$/c^2$: $\sigma_{\gamma\gamma}^{e^+e^-} = 154 \pm 11(\text{sta})^{+16.6}_{-10.8}(\text{sys})$ μb;

higher mass interval, $3.7 < M_{inv} < 10$ GeV$/c^2$: $\sigma_{\gamma\gamma}^{e^+e^-} = 91 \pm 10(\text{sta})^{+10.9}_{-8.0}(\text{sys})$ μb;

to be compared with $\sigma_{\gamma\gamma} = 128\mu$b and $\sigma_{\gamma\gamma} = 77\mu$b given by STARLIGHT, respectively.

In Fig. 4.12 the cross section as a function of the invariant mass, for the two mass ranges are shown.

4.3 Discussion on the results

In this last section a comparison between the results obtained in this analysis and some theoretical and phenomenological predictions is faced, both for the J/ψ photoproduction (Par. 4.3.1) and the two-photon scattering (Par. 4.3.3). In particular in Par. 4.3.2, the results on the vector meson photoproduction are re-interpreted in terms of the nuclear suppression factor already introduced in Par. 1.4.3, as did by [22].

4.3.1 Coherent and incoherent cross section

The cross section of coherent J/ψ photoproduction is compared with calculations from six different models in Fig. 4.13(a) [104, 24, 4, 113, 114, 115]. The incoherent production cross section is compared in Fig. 4.13(b) with calculations by three different models [104, 24, 115]. These models calculate the photon spectrum in impact parameter space in order to exclude interactions where the nuclei interact hadronically.

In Chapter 1 it was emphasized how the differences between the models come mainly from the way the photonuclear interaction is treated and the fit performed to the experimental data from deep inelastic scattering to parametrize the gluon nPDF. The predictions can be divided into three categories:

(i) those that include no nuclear effects (AB-MSTW08, see below for definition). In this approach, all nucleons contribute to the scattering, and the forward scattering differential cross section, $d\sigma/dt|_{t=0}$ (t is the momentum transfer from the target nucleus squared), scales with the number of nucleons squared, A^2;

(ii) models that use a Glauber approach to calculate the number of nucleons contributing to the scattering (StarLight, GM, CSS and LM). The calculated cross section depends on the total J/ψ -nucleon cross section and on the nuclear geometry;

(iii) partonic models, where the cross section is proportional to the nuclear gluon distribution squared (AB-EPS08, AB-EPS09, AB-HKN07, and RSZ-LTA).

The rapidity region $-0.9 < y < 0.9$ considered here corresponds to photon-proton centre-of-mass energies, $W_{\gamma p}$, between 59 and 145 GeV. A vector meson produced at a given rapidity y is sensitive, at hard scales $Q^2 \approx M_V^2/4$, to the gluon distribution at Bjorken-x:

$$x = \frac{M_V}{\sqrt{s_{NN}}} e^{\pm y}, \tag{4.9}$$

where M_V is the mass of the photoproduced vector meson and $\sqrt{s_{NN}} = 2.76$ TeV. The two-fold ambiguity in x is due to the fact that either nucleus can serve as photon emitter or photon target.

In ALICE the measurement at forward rapidity [95] probed Bjorken-x at $\approx 10^{-2}$ and $\approx 10^{-5}$ for the interval bin , $3.6 < y < 2.6$. As it appears evident from Fig. 4.13(a), the data plotted in

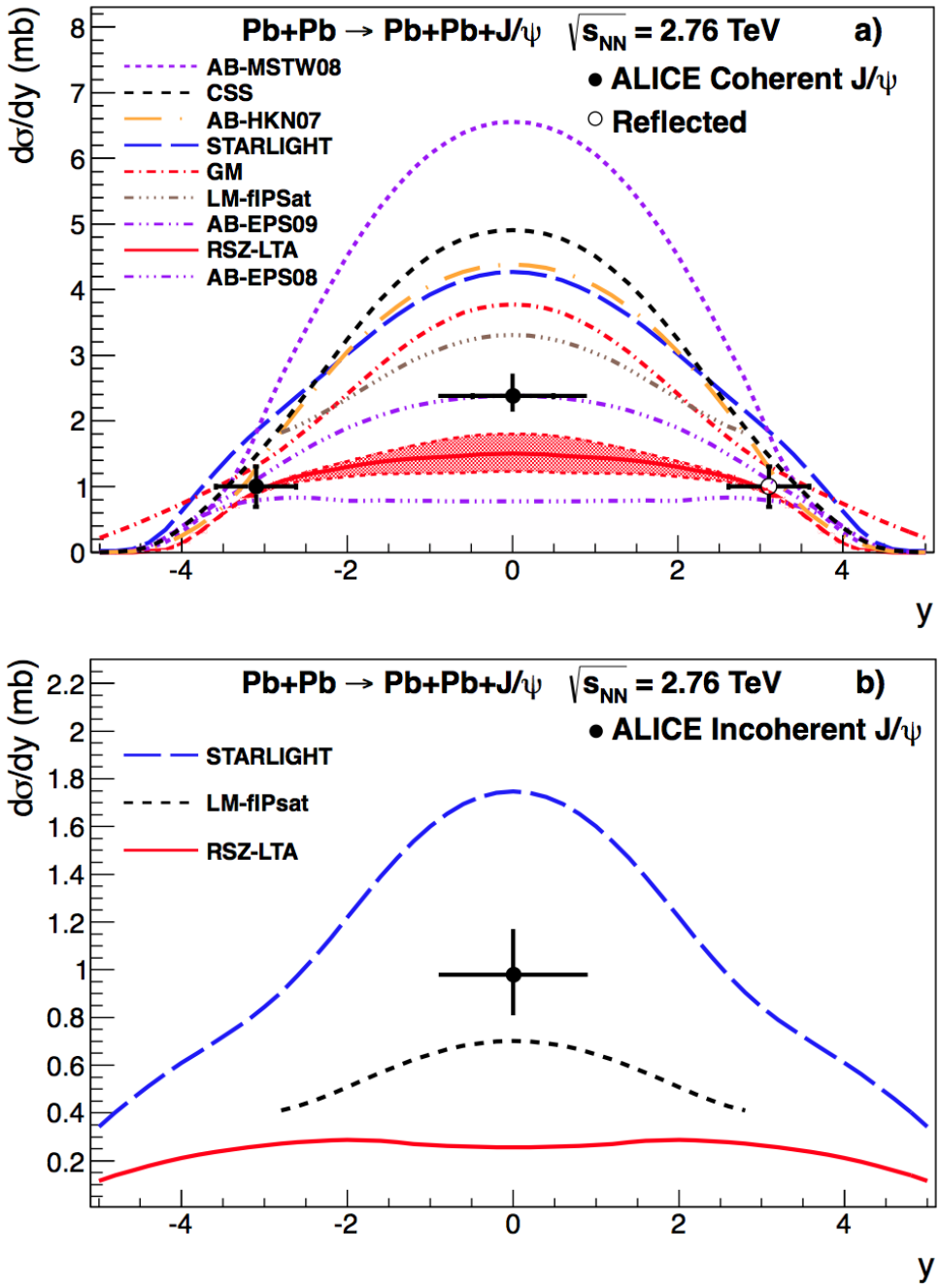

Figure 4.13 Measured differential cross section of J/ψ photoproduction in ultra-peripheral $Pb-Pb$ collisions at $\sqrt{s_{NN}} = 2.76$ TeV at $-0.9 < y < 0.9$ for coherent *a)* and incoherent *b)* events. The error is the quadratic sum of the statistical and systematic errors. The theoretical calculations described later in the text are also shown.

this interval don't allow a clear discrimination of the models since the latter have very similar outcomes. However, it is possible to conjecture a qualitative rejection of the (i)-type models. At the rapidity considered in this work instead, it is possible to improve significantly the model discrimination power. The corresponding range in Bjorken-x for the analysis at midrapidity is between $x = 5 \times 10^{-4}$ and $x = 3 \times 10^{-3}$. In this region, a rather strong shadowing is expected,

and models based on perturbative QCD predict a lower value for the cross section than models using a Glauber approach to account for the nuclear effect. As the effect of the gluon shadowing increases, the cross section become smaller.

The measured coherent cross section, listed in Tab. 4.5, is in very good agreement with the calculation by Adeluyi and Bertulani using the EPS09 nuclear gluon parametrization. The GM model, and the other models using a Glauber approach, predict a cross section a factor 1.5-2 larger than the data, overestimating the measured cross section by more than 3 standard deviations. So does the prediction based on the HKN07 parametrization, which includes less gluon shadowing than EPS09. The model AB-EPS08, significantly underestimates the measured cross section by about a factor of two (about 5 standard deviations), indicating that the gluon shadowing is too strong in the EPS08 parameterization. The leading twist calculation (RSZ-LTA) is also significantly below the data, by about 2-3 sigma.

For the incoherent cross section, shown in Fig. 4.13(b), there are three model predictions available, LM,StarLight, and RSZ-LTA. The measured value deviates by about two standard deviations from the LM prediction, while StarLight predicts an incoherent cross section 60% too high, and RSZ-LTA a factor 4 too low. Taking the ratio between the incoherent and coherent cross section provides further constraints on the treatment of the nuclear modifications implemented in the different models. Another advantage is that the photon spectrum is factorized out, so that the comparison directly probes the ratio of the photonuclear cross sections. The ratio obtained from data is $0.41^{+0.10}_{-0.08}$(sta+sys). This can be compared with 0.21 from LM, 0.41 from Starlight, and 0.17 from RSZ-LTA. Although the latter model is quite close for the coherent cross section at mid-rapidity, it seems to underpredict the incoherent cross section. The LM model also predicts a too low ratio. Starlight, on the other hand, has about the right ratio of incoherent-to-coherent cross section, although it does not reproduce any of the cross sections individually. All three models use the Glauber model to calculate the incoherent cross section, but the implementation and the input cross section for $\gamma + p \to J/\psi + p$ varies. In StarLight the scaling of the inelastic J/ψ + nucleus cross section, ranges from $A^{2/3}$ to A, depending on the J/ψ + nucleon cross section. In the first case, only the nucleons on the surface participate in the scattering, while in the second one all the nucleons contribute. The cross section for incoherent photoproduction is assumed in StarLight to follow the same scaling, while in the other models, the reduction with respect to the A scaling is larger.

In conclusion, models which include no nuclear gluon shadowing are inconsistent with the measured results, as those which use the Glauber model to incorporate nuclear effects. The AB-HKN07 and AB-EPS08 models contain too little or too much shadowing, respectively, to match the data. The analysis results are about 3 sigma higher than the RSZ-LTA model prediction, although a deviation of just 1.5 sigma is found from the model upper limit. Nevertheless the above predictions may have large uncertainties coming not only from the parametrization of the nuclear gluon distribution but also from the selection of the hard scale, the contributions from the higher order terms and the treatment of the photon fluctuation to a quark-antiquark pair. The current measurement will contribute to resolve these uncertainties. None of the three existing models, instead, predicts the incoherent photoproduction cross section correctly, but StarLight predicts a correct incoherent-to-coherent ratio.

4.3.2 Implications on the nuclear suppression factor

It is interesting now to express the results in term of the nuclear suppression factor, discussed in Chapter 1. The measurements of exclusive J/ψ production in ultra-peripheral PbPb collisions at 2.76 TeV indeed, seems to provide the first direct experimental evidence for the nuclear gluon shadowing in lead nuclei at $x \sim 10^{-3}$. The evidence is based on the comparison of the nuclear

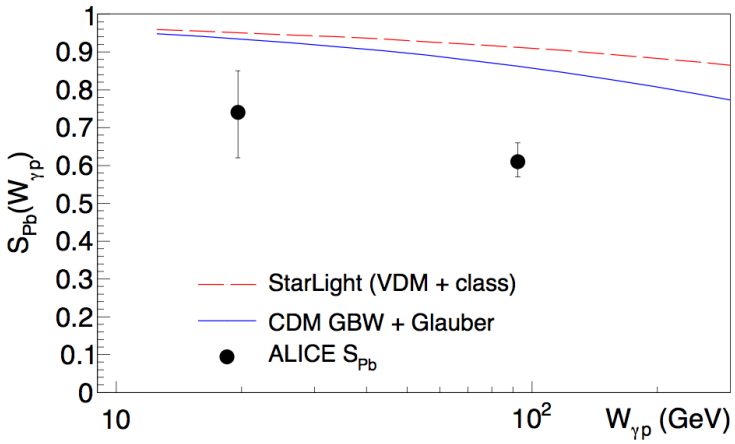

Figure 4.14 Comparison of the ALICE suppression factors with the estimates in the Glauber model with the color dipole cross section and in the Starlight approach [22].

suppression factor experimentally found with with the nuclear gluon shadowing predicted by the global fits of nuclear parton distributions and by the leading twist theory of nuclear shadowing [22].

In Par. 1.4.3 the expressions for both the theoretical and experimental nuclear suppression factor were given at a given γp center of mass energy. In the case of the data collected in this work, $W_{\gamma p}$ ranges between 59 and 145 GeV, but it is convenient to use the value obtained at $y = 0$, namely $W_{\gamma p} = 92.4$ GeV, owing to the two fold ambiguity of the theoretical expression of the differential cross section. Similarly, for the data collected at the forward region, $W_{\gamma p} = 19.6$ GeV at $y = -3.1$. For this values, it turns out from [22] that the two experimental values for the nuclear suppression factor are respectively:

$$S(W_{\gamma p} = 19.6GeV) = 0.74^{+0.11}_{-0.12}, \quad S(W_{\gamma p} = 92.4GeV) = 0.61^{+0.05}_{-0.04}. \tag{4.10}$$

These values, computed starting from the experimental data, can be compared to the relative theoretical estimations discussed. Fig. 4.14 presents the nuclear suppression factor for lead, $S_{Pb}(W_{\gamma p})$, as a function of $W_{\gamma p}$. The result of the calculation using Eqs. 1.351.37 is shown by the blue solid line. One can see from the figure that the predicted nuclear suppression is too small compared to the ALICE results, which are shown as two points with the corresponding error bars.

In the top panel of Fig. 4.15, the values of $S(W_{\gamma p})$ obtained by this analysis of the ALICE data (two black solid circles) at $x = 0.022$ and $x = 0.001$ corresponding to the energies of $W_{\gamma p} =$ 19.6 GeV and $W_{\gamma p} = 92.4$ GeV are compared with the x dependence of the parametrization of the nuclear gluon shadowing factors $R(x)$ used in HIJING 2.0 [116]. In this approach, the nuclear gluon shadowing is characterized by the parameter s_g and, contrary to pQCD, it does not depend on the scale. The nuclear gluon shadowing in this case - which is shown by the red dashed curve - is too strong compared to the ALICE suppression factor at $x \approx 0.001$. The parametrization with $s_g \approx 0.18$ describes the ALICE values very well, see the blue solid curve in the top panel of Fig. 4.15.

In the middle panel of the figure, we compare the nuclear suppression factor found from the analysis of the ALICE data to the x dependence of the nuclear gluon shadowing factors obtained using several nuclear parton distribution functions (PDFs). As developed in Chapter 1, these nuclear PDFs are the results of the global QCD fits based on the data on deep inelastic and Drell-Yan processes on nuclei. In particular, the following leading order approaches where

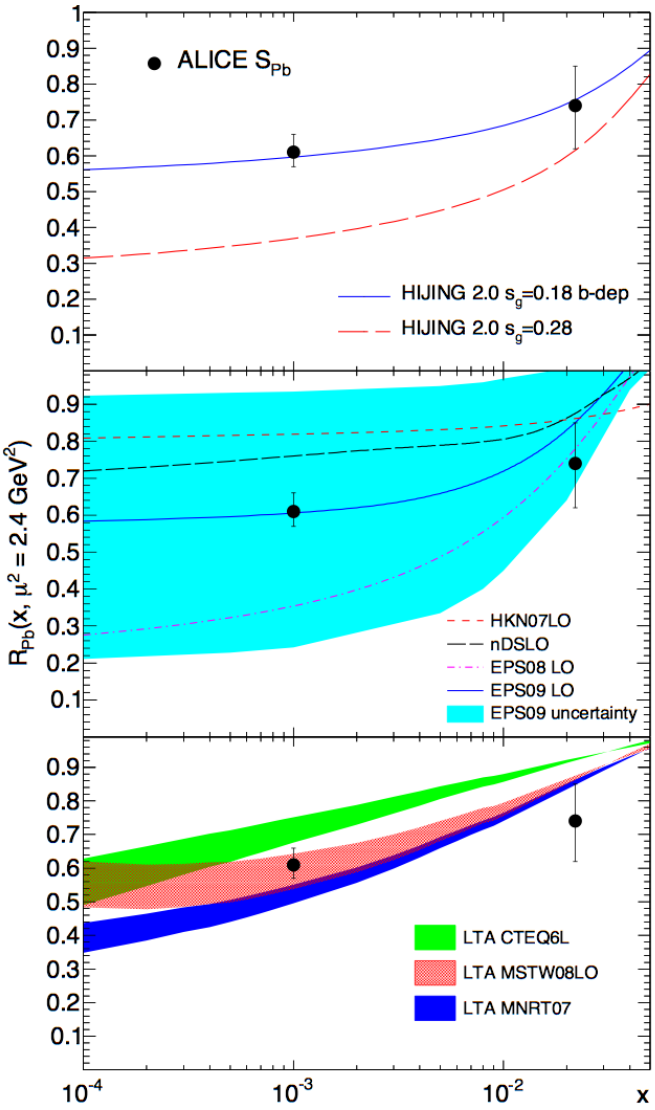

Figure 4.15 Comparison of the ALICE suppression factors with predictions of the nuclear gluon shadowing in HIJING 2.0 *(top)*, global QCD fits *(middle)*, and in the leading twist approximation *(bottom)* as computed by [22].

considered: HKN07 [36], nDS [37], EPS08 [34] and EPS09 [35]. The transfer momentum is always evaluated at the J/ψ mass scale, $Q^2 = M^2_{J/\psi}/4$. From the comparison shown in the middle panel of the figure, HKN07, nDS and EPS08 predictions for $R(x, Q^2 = 2.4)$ GeV^2 are disfavoured by the strong contradiction with the nuclear suppression found by ALICE at $x \approx 0.001$: while HKN07 and nDS predict too weak shadowing, the EPS08 shadowing is too strong. A good agreement is observed for the central set of the EPS09 nuclear gluon shadowing factor (blue solid line). However, one has to admit that the uncertainties of EPS09 (turquoise shaded area) are very large.

One can also compare the nuclear suppression factor found from the analysis of the ALICE data to the nuclear gluon shadowing factors calculated in the leading twist theory of nuclear shadowing [32]. The latter is a dynamical approach based on the QCD factorization theorems, Gribovs theory of inelastic shadowing corrections in multiple scattering, and the HERA diffractive PDFs. The comparison is presented in the bottom panel of Fig.4.15. Three sets of predic-

tions [22] are shown corresponding to three different sets of the gluon PDF in the free proton. The resulting value for $R(x, Q^2 = 2.4)$ GeV^2 predicted by the red band, calculated using the MSTW08 LO [33] nucleon gluon density, is close to the value of nuclear suppression found in the current analysis of the ALICE data.

4.3.3 Two-photons scattering

The data collected for this processes have been compared, as depicted in Fig. 4.12, with the prediction available by the StarLight generator. StarLight computation for the channel $\gamma\gamma \rightarrow e^+e^-$ is performed at the leading order, neglecting NLO effects.

The measured values for the $\gamma\gamma$ cross sections are 20% above but fully compatible within 1.0 and 1.5 sigma with the StarLight prediction for the high and low invariant mass intervals, respectively, if the statistical and systematic errors are added in quadrature. The STAR Collaboration measured the two-photon cross section with a precision of 22.5% when adding the statistical and systematic errors in quadrature [110]. This result was slightly larger than the one predicted by StarLight, but within $\sim 2\sigma$. The PHENIX Collaboration has also measured the cross section of two-photon production of di-electron pairs [111]. This measurement, which has an uncertainty of about 30%, when the statistical and the systematic errors are added in quadrature, was found in good agreement with StarLight.

This result provides important constraints on calculations that include terms of higher orders in α_{em}. A reduction in the two-photon cross section of up to 30% compared with leading-order calculations has been predicted [95]. The result for the two-photon cross section to di-lepton pairs, measured by ALICE with a precision of 12% and 16% for the low and high invariant mass range respectively, is thus fully consistent with StarLight, and sets limits on the contribution from higher order terms [112]. This result reinforces the ALICE J/ψ photoproduction measurement in the forward rapidity region [95], where the cross section was based on $\sigma_{\gamma\gamma}$.

In conclusion, the measured two-photon cross section for di-electron production is consistent with the STARLIGHT model. This implies the models predicting a strong contribution of higher-order terms (not included in StarLight) to the cross section are not favored.

Conclusions

The study of the J/ψ photoproduction at mid-rapidity in ultra-peripheral $Pb-Pb$ collision at $\sqrt{s_{NN}} = 2.76$ TeV has been presented in this work, underlying the relevance of this first measurement at the LHC for the definition of constraints in the nuclear gluon distribution at low Bjorken$-x$. The measurement of the J/ψ photoproduction cross-section indeed, evaluated in the rapidity interval $-0.9 < y < 0.9$, provides a powerful information to constrain the nuclear gluon shadowing in the region $x \approx 10^{-3}$.

The photonuclear origin of the J/ψ is ensured by requiring a minimal hadronic activity, ideally an empty detector but one positive and one negative lepton candidate only. The appearance of these events stands in sharp contrast to central heavy-ion collisions, where thousands of particles are produced. Moreover the J/ψ s are characterized by a very low transverse momentum, entailing a well defined event topology with a back-to-back tracks configuration. The topological constrain was implemented already at the trigger level, thanks to the particular contribution given by the Time-Of-Flight (TOF) system.

The analysis is based on an event sample collected by ALICE in the 2011, corresponding to an integrated luminosity of about 23 μb^{-1}. A detailed discussion on the steps faced for the evaluation of the production cross section has been therefore developed, stressing the contribution to the final result given by this thesis. Such contributions can be summarized in the following list: *(i)* optimization of the analysis selection cuts applied offline to the raw data sample; *(ii)* Monte Carlo extrapolation of the acceptance and efficiency corrections to the signal; *(iii)* simulation of the feed-down contributions from J/ψ s originated in the decay of photoproduced ψ' as a function of three possible polarizations; *(iv)* the simulation of the effects of the J/ψ radiative decay on the signal fit and the applied corrections; *(v)* creation of a Monte Carlo template used in the transverse momentum distribution fit to quantify the possible biases induced by hadronically produced J/ψ in peripheral events; *(vi)* study of the contamination of the signal by photoproduced J/ψ s in peripheral events.

The cross section for coherent and incoherent J/ψ production in the rapidity interval $-0.9 < y < 0.9$, are $d\sigma^{coh}_{J/\psi}/dy = 2.38^{+0.34}_{-0.24}$(sta + sys) mb and $d\sigma^{incoh}_{J/\psi}/dy = 0.98^{+0.19}_{-0.17}$(sta + sys) mb, respectively. These results have been compared to theoretical models and only the coherent cross section is found to be in good agreement with those models which include nuclear gluon shadowing consistent with EPS09 parametrization. On the contrary, none of the three existing models predicts the incoherent photoproduction cross section correctly, although StarLight predicts incoherent-to-coherent ratio consistent with the measurement.

In addition, the cross section for the process $\gamma\gamma \to e^+e^-$ has been measured and found to be in agreement with the StarLight Monte Carlo predictions. This implies that the models predicting a strong contribution of higher-order terms (not included in StarLight) to the cross section are not favoured.

The analysis presented in this work has been recently published by the ALICE Collaboration in the European Physical Journal C [1], with the plot of Fig. 4.12 depicted on the cover-front of the November 2013 issue.

Bibliography

[1] E. Abbas *et al.* (ALICE Collaboration), Eur. Phys. J. C 73, 2617 (2013).

[2] C.A. Betulani, S.R.. Klein, J. Nystrand, Annu .Rev. Nucl. Part. Sci. 55, 271-310 (2005).

[3] A.J. Baltz *et al.*, Phys. Rep 458, 1-171 (2008).

[4] A. Adeluyi and C.A. Bertulani, Phys. Rev. C 85, 044904 (2012).

[5] A. Adeluyi and C.A. Bertulani, Phys. Rev. C 86, 047901 (2012).

[6] A. Adeluyi and C.A. Bertulani, Phys. Rev. C 84, 024916 (2011).

[7] E. Fermi, Z. Physik 29, 315 (1924).

[8] C. F. Weizsäcker, Z. Physik 88, 612 (1934); E. J. Williams, Phys. Rev. 45, 729 (1934).

[9] V.P. Goncalves, C.A. Bertulani,Phys. Rev. C 65, 054905 (2002).

[10] K. G. Wilson, Phys. Rev. D **10**, (1974) 2445.

[11] G. Baur *et al.*, Phys. Lett. B368, 251 (1996).

[12] G. Blanford*et al.*, Phys. Rev. Lett. 80, 3040 (1998)

[13] C. A. Bertulani and G. Baur, Phys. Rep. 163, 299 (1988); G. Baur and L.G. Ferreira Filho, Nucl. Phys. A 518, 786 (1990).

[14] M. Drees and D. Zeppenfeld, Phys. Rev. D 39, 2536 (1989).

[15] C.A. Salgado *et al.*, J.Phys. G: Nucl. Part. Phys. 39, 015010 (2012).

[16] J.C. Collins,D.E. Soper and G. Sterman, Adv. Ser. Direct. High Energy Phys. 5 (1988).

[17] T. Gousset , H.J. Pirner, Phys Lett. B 375 (1996); K.J. Eskola, V.J. Kolhinen, P.V. Ruuskanen, Nucl. Phys. B 535, 351 (1998); L. Frankfurt, M. Strikman, Eur. Phys. J. A 5, 293 (1999).

[18] C. Adler *et al.* (STAR Collaboration), Phys. Rev. Lett. 89, 272302 (2002)

[19] M. Gluck and E. Reya, Phys. Lett. B 79, 453 (1978); L. M. Jones and H. W. Wyld, Phys. Rev. D 17, 759 (1978); H. Fritzsch and K. H. Streng, Phys. Lett. B 72, 385 (1978).

[20] M. Gluck, J. F. Owens, and E. Reya, Phys. Rev. D 17, 2324 (1978); B. L. Combridge, Nucl. Phys. B 151, 429 (1979);R. Brock et al. (CTEQ Collaboration), Rev. Mod. Phys. 67, 157 (1995).

[21] A. Aktas *et al.* [H1 Collaboration], Eur. Phys. J. C 46, 585-603 (2006); S. Chekanov *et al.* [ZEUS Collaboration], Eur. Phys. J. C 24, 345-360 (2002); J. J. Aubert *et al.* [EMC Collaboration], Phys. Lett. B 89, 267 (1980); M. Binkley *et al.*, Phys. Rev. Lett. 48, 73 (1982); U. Camerini *et al.*, Phys. Rev. Lett. 35, 483 (1975).

[22] V. Guzeya, E. Kryshena, M. Strikman, M. Zhalova, arXiv:1305.1724v2 [hep-ph], 9 Oct 2013.

[23] C. W. De Jager, H. De Vries, and C. De Vries, At. Data Nucl. Data Tables 14, 479 (1974).

[24] S. R. Klein and J. Nystrand, Phys. Rev. C 60, 014903 (1999); V.P. Goncalves and C. A. Bertulani, Phys. Rev. C 65, 054905 (2002); V.P. Goncalves and M.V.T. Machado, Phys. Rev. D 77, 014037 (2008).

[25] M. G. Ryskin, Z. Phys. C 57, 89 (1993);

[26] M. G. Ryskin, R. G. Roberts, A. D. Martin, and E. M. Levin, Z. Phys. C 76, 231 (1997); L. Frankfurt, W. Koepf, and M. Strikman, Phys. Rev. D 57, 512 (1998).

[27] S. R. Klein and J. Nystrand, Phys. Rev. Lett. 92, 142003 (2004).

[28] J.J. Aubert *et al.* (European Muon Collaboration), Phys. Lett. B 123, 275 (1983).

[29] K. J. Eskola, V. J. Kolhinen, and C. A. Salgado, Eur. Phys. J. C 9, 61 (1999); M. Hirai, S. Kumano, and T. H. Nagai, Phys. Rev. C 76, 065207 (2007).

[30] K. J. Eskola, H. Paukkunen, and C. A. Salgado, J. High Energy Phys. 04 (2009) 065.

[31] K. Kovarik, I. Schienbein, F. I. Olness, J. Y. Yu, C. Keppel, J. G. Morfin, J. F. Owens, and T. Stavreva, Phys. Rev. Lett. 106, 122301 (2011).

[32] L. Frankfurt, V. Guzey, and M. Strikman, Phys. Rept. 512, 255 (2012).

[33] A. D. Martin, W. J. Stirling, R. S. Thorne, and G. Watt, Eur. Phys. J. C 63, 189 (2009).

[34] K. J. Eskola, H. Paukkunen, and C. A. Salgado, J. High Energy Phys. 07 (2008) 102.

[35] K. J. Eskola, H. Paukkunen, and C. A. Salgado, J. High Energy Phys. 04 (2009) 065.

[36] M. Hirai, S. Kumano, and T. H. Nagai, Phys. Rev. C 76, 065207 (2007).

[37] D. de Florian and R. Sassot, Phys. Rev. D 69 074028 (2004).

[38] V. Guzey and M. Strikman, Phys. Lett. B 687, 16773 (2010).

[39] M. Gluck, E. Reya, and A. Vogt, Phys. Rev. D 46, 1973 (1992).

[40] G. A. Schuler and T. Sjostrand, Z. Phys. C 68, 607 (1995).

[41] F. Cornet, P. Jankowski, and M. Krawczyk, Acta Phys. Pol. B 35, 2215 (2004).

[42] L. Frankfurt, M. Strikman, C. Weiss, Ann. Rev. Nucl. Part. Sci. 55, 403 (2005).

[43] L. Frankfurt, A. Radyushkin, M. Strikman, Phys. Rev. D 55 (1997).

[44] S. J. Brodsky, L. Frankfurt, J. F. Gunion, A. H. Mueller, and M. Strikman, Phys. Rev. D 50, 3134 (1994); J. C. Collins, L. Frankfurt, M. Strikman, Phys. Rev. D 56 (1997).

[45] F. Gelis, E. Iancu, J. Jalilian-Marian and R. Venugopalan, Ann. Rev. Nucl. Part. Sci. 60, 463 (2010).

[46] L.V. Gribov,E.M. Levin and M.G. Ryskin, Phys.Rep.100, 1 (1983).

[47] F. Gelis,E. Iancu, J. Jalilian-Marian and R. Venugopalan, Ann.Rev.Nucl.Part.Sci.60, 463 (2010).

[48] I.I. Balitsky and L.N. Lipatov, Sov. J. Nucl. Phys. 28, 822 (1978); I.I. Balitsky and L.N. Lipatov, Yad. Fiz. 28, 1597 (1978).

[49] M. B. Gay Ducati, M. T. Griep and M. V. T. Machado, arXiv:1305.2407v2 [hep-ph] 25 Jul 2013.

[50] F. E. Low, Phys. Rev. D 12, 163 (1975).

[51] R. Spital and D. R. Yennie, Phys. Rev. D 9, 138-155 (1974).

[52] T. H. Bauer, R. D. Spital, D. R. Yennie and F. M. Pipkin, Rev. Mod. Phys. 51, 407 (1979).

[53] K. J.Golec-Biernat and M. Wusthoff, Phys. Rev. D59, 014017 (1998).

[54] http://sourceforge.net/projects/upcstarlight; S. Klein, J. Nystrand, Phys. Rev. C60, 014903 (1999).

[55] L.D. Landau, E.M. Lifshitz., Phys. Zs. Sowjet 6, 244 (1934); G. Racah, Nuovo Cimento 14, 93 (1937).

[56] D. Antreasyan *et al.*, preprint CERN-EP/8082 (1990).

[57] J. Nystrand and S. Klein, arXiv:nucl-ex/9811007v2 18 Nov 1998.

[58] K. Hencken, D. Trautmann, G. Baur, Phys. Rev. C 59, 841 (1999).

[59] A. J. Baltz, Phys. Rev. Lett. 100, 062302 (2008); A. J. Baltz, Phys. Rev. C 80, 034901 (2009).

[60] R.N. Lee, A.I. Milstein, V.G. Serbo, Phys. Rev. A 65, 022102 (2002).

[61] D.Yu. Ivanov, A. Schiller, and V.G. Serbo, hepph/9809281.

[62] M.L. Miller, K. Reygers, S.J. Sanders and P. Steinberg, Ann. Rev. Nucl. Part. Sci., 57, 205 (2007).

[63] T.Matsui, H.Satz, Phys. Lett. B 178, 416 (1986).

[64] R. Rapp, D. Blaschke, P. Crochet, Prog. Part. Nucl. Phys. 65, 209 (2010).

[65] B. Abelev *et al.* (ALICE Collaboration), Phys. Rev. Lett. 109, 072301 (2012).

[66] B. Abelev *et al.* (ALICE Collaboration), JHEP 09, 112 (2012).

[67] L. Evans (ed.), P. Bryant (ed.), JINST 3, S08001 (2008); O. S. Broning et al., *LHC Design Report*, (2004).

[68] CERN, *Report on the 19th September incident at the LHC*, (2008).

[69] F. Bellini, PhD thesis, Scuola di Dottorato dell'Universitá di Bologna (2013).

[70] J. M. Jowett *et al.*, *First run of the LHC as a heavy ion collider*, CERN, (2011).

[71] K. Aamodt *et al.* (ALICE Collaboration), JINST 3, S08002 (2008).

[72] K. Aamodt *et al.* (ALICE Collaboration), Phys. Rev. Lett. 106, 032301 (2011).

[73] J. Thäder, J. W. Goethe Universität, Frankfurt, PhD thesis, CERN-THESIS-2012-319 (2012).

[74] ALICE Collaboration, ALICE Technical Design Report of the Trigger, Data Acquisition, High-Level Trigger, and Control System, ALICE TDR 10 (2004).

[75] ALICE Off-line framework, AliRoot, http://aliceinfo.cern.ch/Offline

[76] ROOT, http://root.cern.ch; R. Brun, F. Rademakers, Nucl. Instrum. Meth. A 389, 81-86 (1997).

[77] AliEn - ALICE Environment, http://alien2.cern.ch.

[78] P. Saiz *et al.*, Nucl. Inst. Meth. A 502, 437-440 (2003).

[79] L. Milano, PhD thesis, Scuola di Dottorato dell'Universitá di Torino, CERN-THESIS-2012-251 (2012).

[80] PYTHIA online manual, http://home.thep.lu.se/ torbjorn/pythia81html/ Welcome.html; T. Sjöstrand, Comput. Phys. Commun. 82, 74 (1994).

[81] HIJING Documentation, http://www-nsdth.lbl.gov/ xnwang/hijing/.

[82] GEANT - Detector Description and Simulation Tool, http://wwwasd.web.cern.ch/wwwasd/geant.

[83] FLUKA project homepage, http://www.fluka.org/fluka.php.

[84] G. Alessandro *et al.* (ALICE Collaboration), J. Phys. G 32, 1295- 2040 (2006).

[85] B. Batyunya, Yu. Belikov, K. Safarik, ALICE Internal Note, ALICE-INT-97-24 (1997).

[86] D. Caffarri, Ph.D. thesis, Scuola di Dottorato di Ricerca in Fisica dell'Università di Padova, (2011).

[87] CERN/LHCC 2000-012, ALICE TDR 8, 16 February 2000, ALICE TOF Technical Design Report; CERN/LHCC 2002-016, Addendum to ALICE TDR 8, 24 April 2002;ALICE Collaboration, ALICE: Physics Performance Report Vol. 1, J. Phys. G: Nucl. Part. Phys. 30, 15171763 (2004).

[88] A. Akindinov *et al.*, Nucl. Instrum. Meth. A 456, 16 (2000).

[89] A. Akindinov *et al.*, Eur. Phys. J. Plus 128, 44 (2013).

[90] E. Cerron Zeballos *et al.*, Nucl. Instr. and Meth A 374 (1), 132-135 (1996).

[91] A. Akindinov,A. Alici,P. Antonioli, S. Arcelli, Y. Baek,*et al.*, Nucl.Instr. Meth. A 602, 658-664(2009); A. Akindinov *et al.*, Nucl. Instrum. Meth. A 602, 709-712 (2009).

[92] F. Anghinolfi *et al.*, Nucl. Instrum. Meth. A 533, 183 (2004).

[93] ALICE Collaboration, CERN-LHCC-2012-012 / LHCC-I-022 September 7, 2012.

[94] A. Akindinov *et al.*, Eur. Phys. J. C 34, 325 (2004).

[95] B. Abelev *et al.* (ALICE Collaboration), Phys. Lett. B 718, 1273 (2013).

[96] A. Akindinov *et al.*, Nucl. Instrum. Meth. A 602, 372 (2009).

[97] C. Mayer and E. Kryshen, ALICE-INT-2012, 20 October 2012.

[98] S. van der Meer, ISR-PO/68-31, KEK68-64.

[99] K. Oyama and M. Gagliardi, proceeding of the LHC Lumi days 2012, CERN, February 29 - March 1, 2012,

[100] B. Abelev *et al.* (ALICE Collaboration), Phys. Rev. Lett. 109, 252302 (2012).

[101] https://indico.cern.ch/getFile.py/access?contribId=3&resId=0&materialId=slides&confId=106351 .

[102] J. E. Gaiser, Ph.D. thesis, SLAC-R-255 (1982).

[103] S. Chekanov *et al.* (ZEUS Collaboration), Eur. Phys. J. C 24, 345 (2002); A. Aktas *et al.* (H1 Collaboration), Eur. Phys. J. C 46, 585 (2006).

[104] V. Rebyakova, M. Strikman and M. Zhalov, Phys. Lett. B 710, 647 (2012).

[105] K. Aamodt *et al.* (ALICE Collaboration), Phys. Rev. Lett. 106, 032301 (2011).

[106] K. Aamodt *et al.* (ALICE Collaboration), Phys. Lett. B 718, 692 (2012).

[107] J. Beringer *et al.* (Particle Data Group), Phys. Rev. D86, 010001 (2012)

[108] D. J. Lange, Nucl. Instrum. Meth. A 462, 152 (2001).

[109] E. Barberio, Z. Was, Comput. Phys. Commun. 79, 291 (1994).

[110] J. Adams *et al.* (STAR Collaboration), Phys. Rev. C 70, 031902 (2004).

[111] S. Afanasiev *et al.* (PHENIX Collaboration), Phys. Lett. B 679, 321 (2009).

[112] K. Hencken, E. A. Kuraev and V. Serbo, Phys. Rev. C 75, 034903 (2007).

[113] V. P. Goncalves and M. V. T. Machado, Phys. Rev. C 84 (2011) 011902.

[114] A. Cisek, W. Scha fer and A. Szczurek, Phys. Rev. C 86 (2012) 014905.

[115] T. Lappi and H. Mantysaari, arXiv:1301.4095 [nucl-th].

[116] W. T. Deng, X. N. Wang and R. Xu, Phys. Lett. B 701, 133 (2011).